Photon-sail trajectories to exoplanet Proxima b using heteroclinic connections

Master of Science Thesis

Tim Rotmans

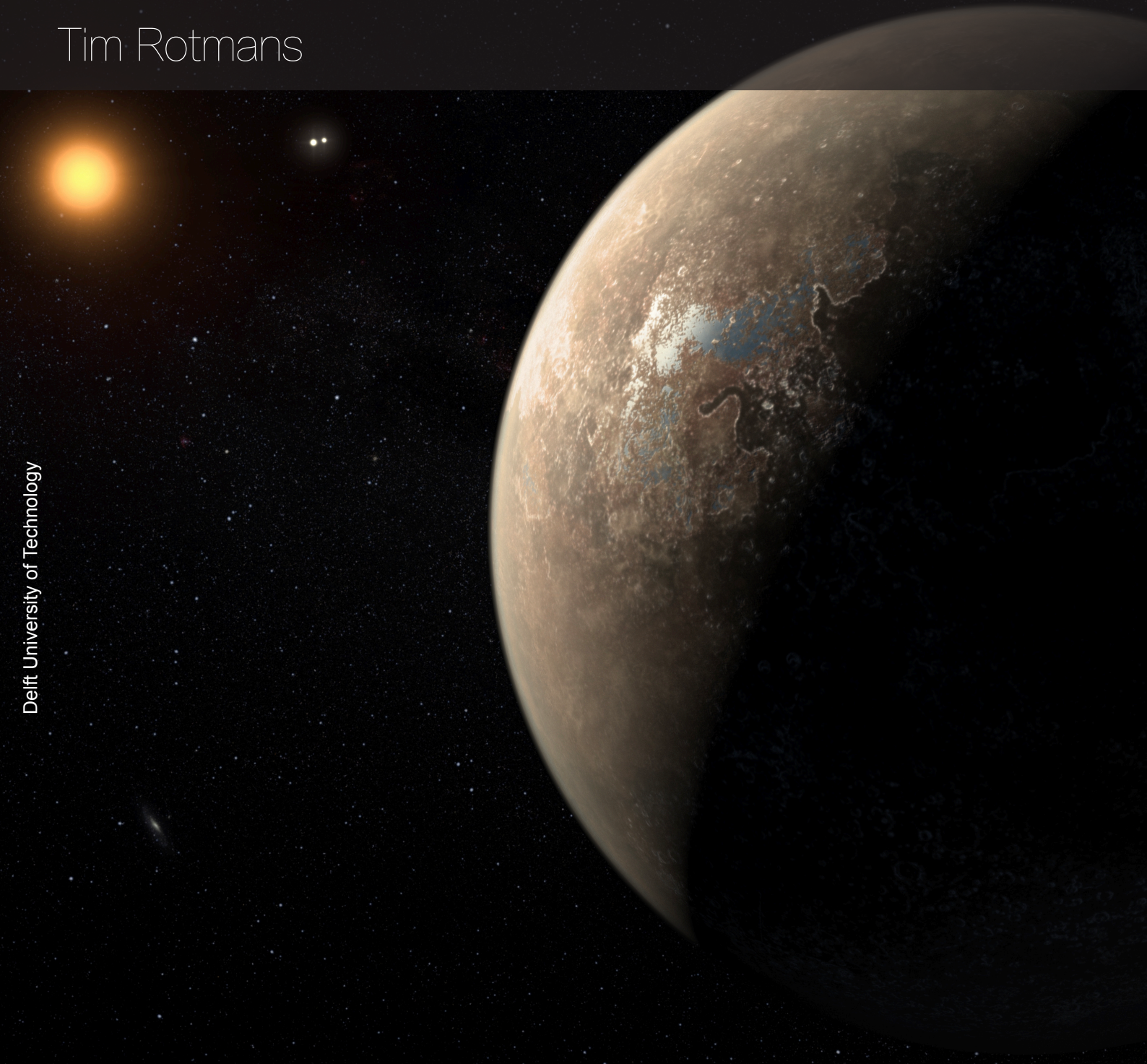

Delft University of Technology

TU Delft

Photon-sail trajectories to exoplanet Proxima b using heteroclinic connections

Master of Science Thesis

by

Tim Rotmans

to obtain the degree of Master of Science
at the Delft University of Technology,
to be defended publicly on Wednesday, March 8, 2023 at 09:30.

Thesis committee: Dr. ir. E. Mooij - Chair
Dr. ir. M.J. Heiligers - Supervisor
Dr. ir. E. van Kampen - External examinator

An electronic version of this thesis is available at http://repository.tudelft.nl/

TU Delft

Preface

The journey this thesis has taken me on feels similar to the interstellar journey that I described in this work: eternally lasting. Especially for this reason, I am thrilled to finally be able to write down my preface, marking the final stage of my thesis. The work provided here investigates heteroclinic connections in the Alpha Centauri systems, specifically meant to find a transfer trajectory headed to Proxima Centauri. It required a ton of creativity and imagination, as I had to imagine a mission scenario that was still pretty futuristic. I'm confident that the final product is engaging, scientifically sound, and original, and I hope it will inspire others in the scientific community to start research on the Alpha Centauri system. In addition, since astrophysics has always fascinated me, I was happy to include an astronomic part in this thesis by using astronomical data needed to describe the orbits of Alpha and Proxima Centauri.

I want to express my gratitude towards my thesis supervisor, Dr. Jeannette Heiligers, for being there throughout the entire journey. Our weekly meetings were truly a delight, and I am still impressed by the amount of knowledge and professionalism she possesses, especially when it comes to solar sailing. Her answers to my questions and our discussions helped me countless times through the difficult moments I experienced during my thesis. It was great to see her taking so much time for her thesis students, and I will remember the Christmas quiz she made for us during the pandemic. I feel lucky and honored with such a great supervisor, and I am glad we could share our passion for solar sailing together.

I also want to thank my friends, family, fellow students, and all the people who helped me throughout my studies and thesis. It might be a cliché, but I could not have done it without them. Furthermore, I want to thank all the professors and teachers in the faculty of spaceflight that educated me. Their courses have inspired me and ignited the passion that I nowadays have for spaceflight. Lastly, I want to thank Pierre Kervella, an astronomer at the Paris Observatory, for his help during my thesis. I reached out to him because I could not understand the astronomical data in one of his publications. He helped me interpret his data and always very elaborately answered my questions.

In closing, this thesis is just the beginning of my journey in solar sailing. I'm excited to keep exploring this fascinating field and contributing to its development in the years to come.

Tim Rotmans
Delft, February 2023

Executive summary

This research investigates photon-sail trajectories towards a rocky, Earth-like exoplanet, Proxima b, located in the habitable zone of Proxima Centauri (AC-C). AC-C is part of the Alpha Centauri system, the stellar system closest to the Solar system. At the center of Alpha Centauri is a binary star system consisting of Alpha Centauri A and B (AC-A and AC-B), revolving around their mutual barycenter in elliptic orbits. AC-C is in a bound orbit around the AC-A/AC-B system at a distance of approximately 13,000 AU. AC-C is a red dwarf star with a small mass; currently, two planets are confirmed to orbit it: Proxima b and Proxima c. Proxima b is a rocky planet and, therefore, the closest Earth-like exoplanet in our galaxy. Visiting Proxima b with an uncrewed probe could provide us with the first view of Earth-like exoplanets and allow us to learn more about the evolution of planets and possibly the formation of life. A solid scientific interest thus endorses a mission towards Proxima b. Breakthrough Starshot was the first to propose a fly-through mission of the Alpha Centauri system, for which photographing Proxima b is the goal. The project aims to send a swarm of miniature spacecraft attached to futuristic ultra-light photon sails and use an Earth-based laser array to propel them to 20% of the speed of light, reaching Alpha Centauri in little over 20 years. While many engineering problems still lie ahead, their proposal initiated other research into photon-sail missions towards or within the Alpha Centauri system. In other literature, the capture of a highly futuristic graphene photon sail to get into a bound orbit about one of the stars in the AC-A/AC-B system is investigated. In that case, a travel time of 75-80 years can be expected. This research is meant as an extension of the work and investigates the next step after reaching the AC-A/AC-B system: going to Proxima b.

To find transfer trajectories from the AC-A/AC-B star system towards Proxima b, a link between the equilibrium points of both systems is searched for through heteroclinic connections. This is done by using the (un)stable photon-sail augmented manifolds of the AC-A/AC-B (departure phase) and AC-C/Proxima b (arrival phase) systems. The manifolds are propagated up to a suitably positioned Poincaré section at which the mismatch between the states of the unstable and stable manifolds is examined. By minimizing the mismatch in position, velocity, and time, a smooth link between trajectories from both systems is searched for. The departure locations investigated for this transfer are the co-linear Lagrange points in the AC-A/AC-B system. The arrival locations are both the co-linear and triangular Lagrange points in the AC-C/Proxima b system. The sail can be maintained at the Lagrange points with an edge-on-sail attitude. To move away from the Lagrange point, the sail attitude is changed to a to-be-optimized attitude, which is kept constant along the augmented photon-sail manifold. Different futuristic sail configurations are assumed based on graphene sail structures with reflective coatings on one or both sides of the sail. A grid search is applied to conduct a first analysis of the problem and explore the design space. The design space exploration focuses on minimizing the linkage errors in position and velocity at the Poincaré section. A genetic algorithm is then applied to also close the gap in linkage time and further minimize the errors in position and velocity. Both methods use the same six parameters to optimize the link: the cone angle (during the departure and arrival phases), the clock angle (again, during the departure and arrival phases), and the departure and arrival dates.

The design space exploration demonstrated that the double-sided reflective sail configuration provides little improvement over a one-sided reflective sail configuration. This is due to the fact that a constant sail attitude is kept along the transfer trajectory so that the features of a double-sided sail are only partially exploited. However, using a double-sided sail does open up the opportunity to depart from the L_1-point in the AC-A/AC-B system. The design space exploration also showed that the mismatch in velocity is the most problematic objective. This can be explained by the different nature of the AC-A/AC-B system compared to the AC-C/Proxima b system. Where the latter only contains one very dim red-dwarf star, the first contains two Sun-like stars. Therefore, the velocity build-up in the departure system is often too large to appropriately decelerate the sail in the arrival system, creating a significant mismatch at linkage. This can be overcome by departing from the L_2-point in the AC-A/AC-B system; from this point, the build-up in velocity is limited and therefore provides the best match at linkage.

Although the arrival location has much less influence on the linkage errors, the design space exploration showed promising results for arrival at the L_1 and L_3-points in AC-C/Proxima b.

Results from the genetic algorithm showed that a transfer from the L_2-point in the AC-A/AC-B system to the L_1-point in the AC-C/Proxima b system can be accomplished with a transfer time of 235 years for a one-sided graphene-based sail with a surface of $315 \times 315m^2$, carrying a payload of 10 grams. The same transfer, with a slightly smaller one-sided graphene-based sail ($75 \times 75m^2$, carrying a payload of 10 grams), results in transfer time of 1025 years. It can therefore be concluded that a very large, futuristic graphene-based photon sail must be used to ensure a reasonable transfer time towards AC-C/Proxima b. For a transfer with either sail configuration, the position error at linkage is kept below 1% of the total travel distance, the velocity error below 1% of the average velocity at linkage, and the time error below 1% of the total transfer time. The results of this research could be used as an initial guess for further optimization efforts to reduce the link errors and possibly decrease the transfer time. To conclude, although the sail configurations utilized in this research may be considered futuristic, the applied methodology has been demonstrated to successfully achieve a transfer to Proxima b.

Contents

List of Figures

List of Tables

1

Introduction

Since humans have been marching the Earth, they have been gazing up at the stars, admiring both their beauty and mystery. Different cultures have had different ideas, explanations, or beliefs about the starry night above their heads and what it could mean. While star constellations were already used to predict seasons by Mayan astronomers [1], the ancient Greeks invented stories and sagas about their Gods to explain the constellations [2]. Later, during the time of the explorers, stars were merely used as a tool to navigate the oceans. It was Giordano Bruno who proposed that the stars could be other ”Suns” and got burned as a heretic in 1600 for his way of thinking. Nowadays, with the help of advanced equipment and much better-developed theories in astronomy, many questions about the vast Universe surrounding us can be answered. It is now known that many of the stars we see are in fact entire galaxies, each one consisting of billions of stars, and the Earth is located in the Milkyway galaxy. However, despite the giant leaps in technological advancement humanity has gone through so far, many questions remain. The depth to which we understand the Universe, based only on theory and observations from the Solar system, is impressive. Nevertheless, one can imagine how our observation-based knowledge could be enriched when in-situ measurements of other systems are possible. What if we could measure (from closeby) gravity, magnetic fields, temperatures, and atmospheric compositions of celestial bodies? What if we could make pictures of exoplanets, exomoons, other stars, or even black holes? How would that change our view of the Universe? In a more general way, human expansion is a phenomenon that can be seen throughout our entire history. The need for cultures to reach out to distinct, unknown places has always been evident. Furthermore, this is all primarily based on one simple question: ”What is out there?”. Translated to modern times, it is humans’ own to start exploring the space surrounding us. In line with this, there is the search for extraterrestrial life. Exploring other worlds and stars might give us more information about how and where life can form, and telescopes can only provide this to a certain extend. In other words, there is an unmistakable scientific base for developing interstellar probes.

1.1. Interstellar travel

In the past decades, scientific efforts have been made to determine the feasibility of interstellar missions. It is obvious that the large travel distances pose the biggest challenge to overcome for interstellar travel. For that reason, a portion of the research on interstellar travel considers currently unavailable or undesired technology, such as nuclear pulse propulsion, antimatter, nuclear fusion, or a ramjet [3, 4]. A less ”science-fiction like” solution would be the use of photon-propelled spacecraft [5–7], also called photon or solar sails. Such a spacecraft uses a surface to reflect photons that consequently transfer a momentum to the sail in the opposite direction, ”pushing” the sail through space. Despite many challenges still ahead, this method is currently seen as one of the feasible ways to succeed in (uncrewed) interstellar travel. In 2016, the Breakthrough Initiatives program proposed a futuristic mission (Breakthrough Starshot) towards Alpha Centauri.[1] Alpha Centauri is an interesting target because it is the closest stellar system [8, 9], at a distance of approximately 4.37 lightyears from the Sun, see

[1] https://breakthroughinitiatives.org/initiative/3, access date:13-12-2022

Table 1.1: Parameters for the three stars within the Alpha Centauri system. The mass, luminosity, and radius are expressed in solar units: $m_\odot$ = $1.989110 * 10^{30}$ kg, $R_\odot$ = $6.9598 * 10^5$ km and $L_\odot$ = $3.854 * 10^{26}$ W [8, 9, 13].

		AC-A	AC-B	AC-C	Sun	Unit
mass	m	1.100	0.9070	0.1230	1	$m_\odot$
Luminosity	L	1.519	0.5002	0.0015	1	$L_\odot$
Radius	R	1.230	0.8570	0.1450	1	$R_\odot$
Avg. Temperature	T	5790	5260	3040	5770	K

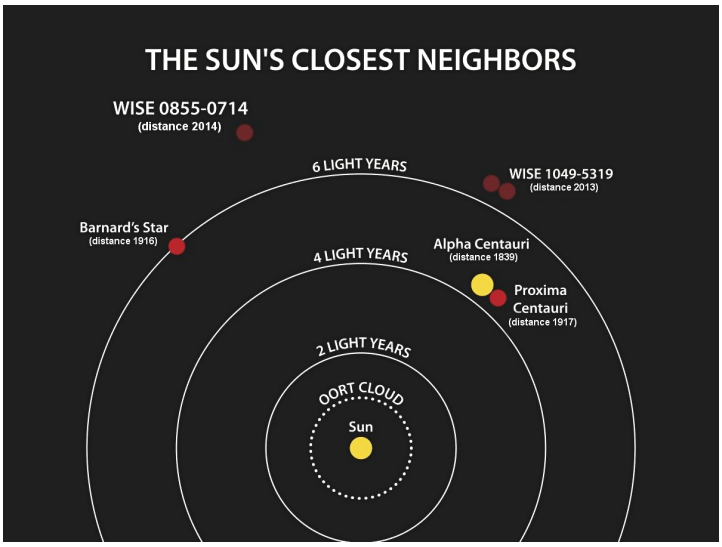

Figure 1.1: Schematic overview of the stars closest to the Solar system.

Fig. 1.1.[2] The system consists of three stars: a binary system consisting of the stars Alpha Centauri A (AC-A) and Alpha Centauri B (AC-B), moving in elliptical orbits about their common barycenter. The third star, a red dwarf called Proxima Centauri (AC-C), orbits the AC-A/AC-B system at a distance of approximately 13,000 AU. In Table 1.1, the mass m, luminosity L, radius R and average surface temperature T of each star is given. As of today, two planets are confirmed to orbit AC-C, Proxima b and Proxima c, from which the first is a rocky planet in the habitable zone of AC-C [10–12]. The eccentric orbit of Proxima b has a semi-major axis of 0.05 AU, whereas Proxima c is further away from AC-C, at a distance of 1.5 AU. As in-situ measurements could add much to our knowledge of exoplanets and the potential formation of life in the Universe, this work aims to search for trajectories to Proxima b. The Breakthrough Starshot project also proposes a mission to Proxima b: it aims to visit the Alpha Centauri system with a swarm of ultra-lightweight laser-propelled photon sails to photograph planet Proxima b. The swarm will be accelerated to 20% of the speed of light by using a 100GW Earth-based laser array, reaching the system in a little over 20 years. It then takes four years to send data back to Earth. The probes in the swarm consist of gram-scale wafers with measurement and communication equipment, attached to a meter-scale photon sail.[3]

1.2. Photon sailing

The concept of using photon sails for propulsion in space was already introduced by rocket scientist Tsiolkovsky at the beginning of the 20th century [14]. A photon sail is a lightweight, highly reflective sail-like structure with a large surface area that is deployed in space [15]. Reflecting photons transfer a momentum to the sail; therefore, light can be used as an infinite source of propellant (as long as one stays in the proximity of a star). The main benefit of this technology is that no fuel is needed (after placement in orbit) to propel a spacecraft through space. Several missions have already proved the feasibility of this concept. JAXA launched the first photon sail in 2010, the IKAROS (Interplanetary Kite-craft Accelerated by Radiation Of the Sun) spacecraft that performed a flyby of Venus [16]. The

[2] https://photojournal.jpl.nasa.gov/catalog/PIA18003, accessed:05-01-2023
[3] https://breakthroughinitiatives.org/concept/3, access date:05-01-2023

principal mission was to measure the acceleration from solar radiation pressure on the sail and demonstrate attitude control of the thin membrane sail. The Planetary Society has launched two photon sails, Lightsail 1 and 2 [17], see Fig. 1.2 for a picture and artist impression of Lightsail 2. The first was merely a deployment demonstration launched in 2015, whereas the latter successfully managed to change its orbital altitude by using solar radiation pressure only. NASA has launched the NanoSail-D2 spacecraft [18] and will launch the ACS3 (Advanced Composite Solar Sail System) mission in 2023 [19]. NanoSail-D2 was NASA's first solar-sail demonstrator mission to test the deployment and deorbit functionality, launched in 2011. The ACS3 mission is merely meant to test a new composite sail boom material.

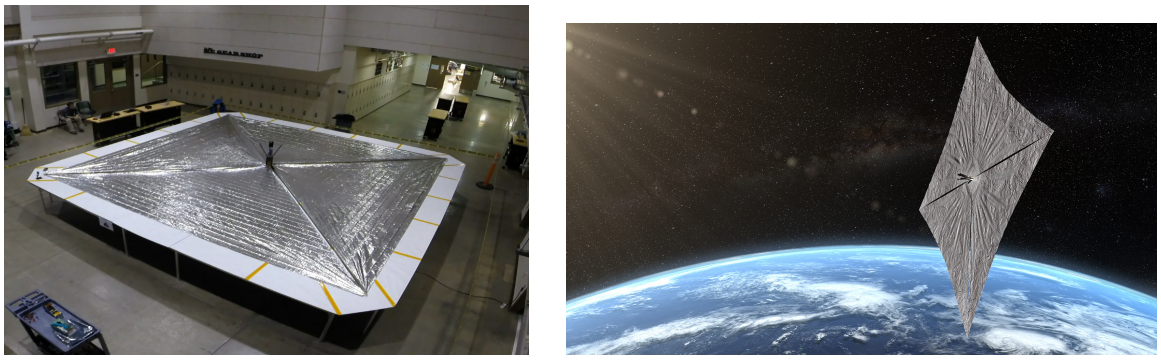

(a) (b)

Figure 1.2: (a) Planetary Society's Lightsail 2 sail, unfolded on the deployment table on Earth. Image Credit: Planetary Society/Justin Foley *"LightSail 2 with solar sails deployed."*, licensed under CC BY 3.0. (b) LightSail 2 deployed in space (artist impression). Image Credit: Planetary Society/Josh Spradling *"LightSail, a Planetary Society solar sail spacecraft."*, licensed under CC BY 3.0

1.3. State-of-the-art literature review

Several publications investigate photon-sail missions towards and in the Alpha Centauri system. In reference [20], the maximum velocity still allowing for capture in the Alpha Centauri system is investigated by making use of photo-gravitational assists; that is, using gravitation and photonic pressure to slow down the sail. Using a futuristic graphene sail of $10^5 \mathrm{m}^2$, they computed a maximum arrival speed of 4.6% of the speed of light, resulting in a 95 years journey from Earth to the AC-A/AC-B system and an additional 46 years to AC-C. The mission scenario described in the paper is displayed in a schematic in Fig. 1.3. The sail has a sufficiently large surface so that a laser array is not needed to accelerate the sail to this velocity. They substantially decreased the travel time to 75 years in successive work by approaching the system differently [21]. Subsequently, they investigated the use of the magnetic fields of the AC-A/AC-B system to decelerate a spacecraft [22], in combination with photo-gravitational maneuvers. They find that magnetism can significantly affect the trajectory if the sail is charged by more than 10 μC/g (Coulomb/gram), sustaining a larger deceleration. However, a charged sail is extremely susceptible to small changes in the trajectory and, therefore, highly unpredictable. In reference [23], different scenarios of a photon-sail exploration mission of the AC-A/AC-B system were investigated. The authors divide their mission into four phases: a capture about AC-A, a polar orbit about AC-A, a transfer to AC-B, and a polar orbit about AC-B. Each phase is optimized, finding a total exploration time of 32.2 years. Their entry velocity was set to 80 km/s, leading to a travel time towards the system of approximately 150 years. Lastly, in two publications the elliptic restricted three-body problem (ERTBP) is applied to the AC-A/AC-B system. The ERTBP is a model that describes the dynamics within a system of two primary bodies in non-circular orbits. The model assumes a third body that is massless. In the ERTBP, it is possible to find points in space where centrifugal and gravitational forces sum to zero, creating equilibrium points. The ERTBP can be augmented with a photon sail. Because this changes the dynamics of the system, these equilibrium points can be altered into artificial equilibrium points (AEPs). In reference [24], the AEPs in the AC-A/AC-B system with the addition of a solar balloon are considered. The authors show that unstable AEPs can be found within the plane of motion of the primaries. By linearization around the points, they prove that these points can be stabilized using control laws. In addition, in reference [25], the AEPs in the AC-A/AC-B system are examined and the authors found small, stable regions close to AC-A. Furthermore, they successfully compute transfer trajectories

between different AEPs.

1.4. Brief overview of the approach of this research

This work aims to find optimized trajectories to Proxima b, after a capture in the AC-A/AC-B system has successfully been accomplished. Therefore, the trajectory departs from the AC-A/AC-B system, with the Proxima b/AC-C system as a target. Hence, the AC-A/AC-B system is defined as the departure system and the AC-C/Proxima b system as the arrival system. Because of the elliptic orbits of the binary stars and Proxima b about AC-C, in this work the ERTBP is applied on both systems. Then, transfer trajectories are searched for by optimizing the links between departure and arrival phase (i.e., trajectories moving away/towards the respective system). Previous work on transfer trajectories between or within such systems was done in the Solar system. In reference [26], heteroclinic connections, that are, connections between equilibrium points, in the Sun/Earth system [26] are investigated. In reference [27], heteroclinic connections between halo orbits in *different* Sun-planet system (Sun/Earth to Sun/Mars, Sun/Earth to Sun/Mercury) were found. In reference [28], time-optimal solar-sail heteroclinic connections between the Earth/Moon and Sun/Mars systems were searched for. In reference [29], transfer trajectories for spacecraft from the Sun/Earth to the Earth/Moon system were computed using a patched ERTBP approximation model, in which both the departure and arrival systems are modelled using the ERTBP. The two systems are then ”patched” together to find a transfer from a Moon orbit to an equilibrium point in the Sun/Earth system. They use a Poincaré section at which the two systems are patched together. Such a surface will from now be referred to as the linkage, or the linkage surface. The publications named above show the potential of using heteroclinic connections to find suitable transfers between equilibrium points in different systems. Therefore, this work uses a similar approach applied to the Alpha Centauri system. To optimize the connections between the different systems, the error in position, velocity, and time between the departure and arrival phases at the link surface is minimized. Different sail configurations, meaning sails with varying lightness numbers and a reflective coating on one side or on both sides, are used. The lightness number of a photon sail is a ratio that indicates its efficiency. To solve this optimization problem, two methods are applied: a grid search and a genetic algorithm. The two methods generally both have advantages and disadvantages. The grid search is computationally heavy but can provide good insight into the problem. It is also a robust method to find a globally optimal solution. The genetic algorithm is often referred to as a ’black box’. It requires (almost) no knowledge of the user of the system and its implementation is straightforward. But, it will not be able to provide much insights into solving the problem. In literature, both the grid search and the genetic algorithm were already used to optimize heteroclinic connections or comparable numerical optimization problems [25, 28, 29]. Both methods proved to be capable of solving these problems. Due to their proven heritage for similar numerical problems, and their opposing working principles, the combination of these two methods is considered an interesting approach to solving the numerical problem of this work.

1.5. Research Objective & Questions

As was introduced in the previous sections, this thesis work investigates transfer trajectories to planet Proxima b. Such a mission is scientifically grounded because in-situ measurements of this system would provide interesting new insights for (exo-)planetary research. The research objective of this work is:

> “To find photon-sail transfer trajectories between the AC-A/AC-B system and Proxima b by exploiting heteroclinic connections between the equilibrium points of the two different systems.”

The research questions that must be answered to consider this research as a valuable contribution to the existing literature on interstellar photon sailing, or photon sailing in Alpha Centauri, are:

1. **Can a transfer be found between equilibrium points of the AC-A/AC-B and AC-C/Proxima b systems using photon-sail augmented heteroclinic connections?**
   (a) What are the minimum errors at linkage in terms of position, velocity, and time between the trajectories from both systems?

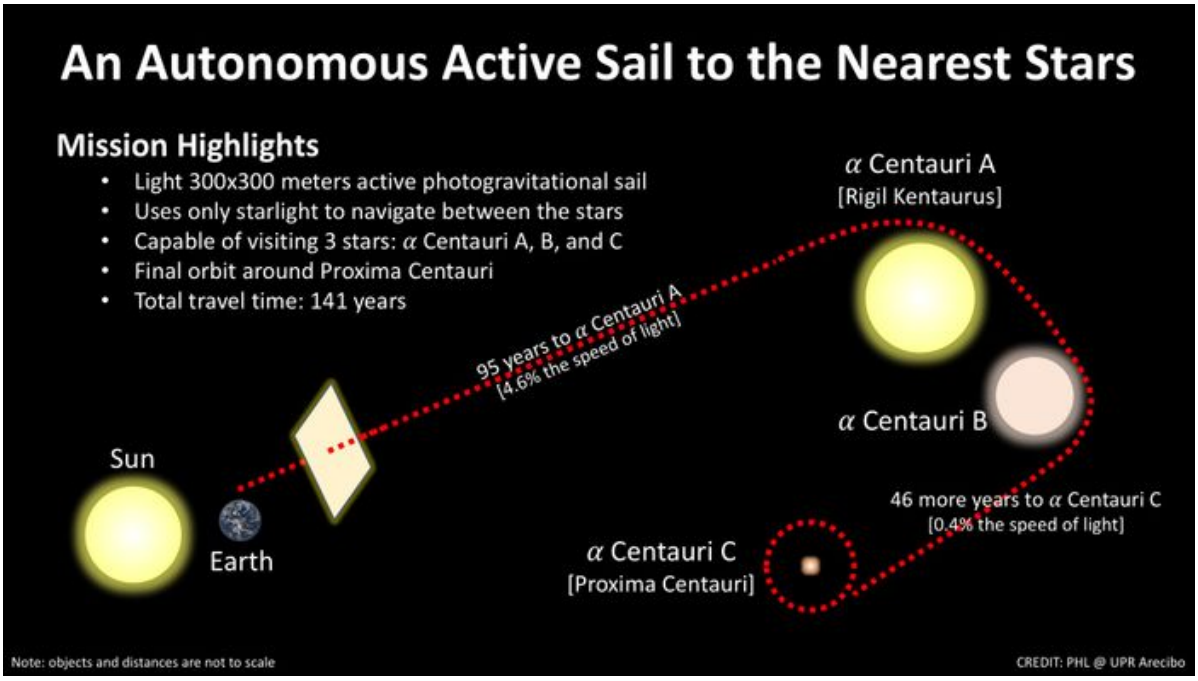

Figure 1.3: Schematic figure of mission proposed by Heller and Hippke (2017) [20].

(b) What is the minimum time of such a transfer?

(c) How do different combinations of departure and arrival locations perform in terms of transfer time and linkage errors?

(d) How do different sail configurations impact the results in terms of transfer time and linkage errors?

2. **Can a grid search be used to reduce the design space for the genetic algorithm?**
3. **Is a genetic algorithm a suited tool to solve the optimization problem in terms of global convergence?**

1.6. Report Outline

The main body of this thesis is written as a journal article, following the format of the Journal of Guidance, Navigation & Control, a journal published by the American Institute of Aeronautics and Astronautics (AIAA). Chapter 2 of this report contains the article, which is named:

"Photon-sail trajectories to exoplanet Proxima b using heteroclinic connections."

The article is structured according to the guidelines issued by the AIAA.[4] The article starts with an abstract, followed by an introduction. Then, information about the Alpha Centauri system is given, followed by a description of the dynamical model, including information about the reference frames used, the accelerations from radiation pressure, the ephemerides data, and the Lagrange points. Then, the optimization problem and methods are described in a methodology section, followed by a design space exploration. The final sections of the article give the results from the genetic algorithm and the conclusions. In the appendix of the article, all the necessary frame transformations are provided. Chapter 3 of this report then gives the additional conclusions and presents the answers to the above state research questions, after which the recommendations for future work are presented. In the first appendix of this report, the verification and validation of the dynamical model and the frame transformations are provided. In Appendix B,the tuning the genetic algorithm settings is explained.

[4] https://www.aiaa.org/home/events-learning/events/Technical-Presenter-Resources, access date: 13-12-2022

2

Article

Photon-sail trajectories to exoplanet Proxima b using heteroclinic connections

Tim J. Rotmans[1]
Delft University of Technology, 2629 HS, Delft, The Netherlands

Now that a rocky planet is confirmed to orbit in the habitable zone of our closest stellar neighbor Proxima Centauri, the interest in visiting that system is growing; especially since Breakthrough Starshot proposed a fly-through mission of the Alpha Centauri system by sending a swarm of laser-driven photon sails. While many engineering problems still need to be solved for such a mission to succeed, research has shown that futuristic, theoretical photon-sail configurations can reach the Alpha Centauri system within 75-80 years while also getting captured in a bound orbit about one of the binary stars. This paper investigates trajectories from the binary star system towards planet Proxima b. A mission to Proxima b is scientifically grounded since measurements or pictures could help us better comprehend the evolution of rocky planets and potential life-formation in our Universe. The classical Lagrange points in the binary system (AC-A/AC-B) and the system Proxima Centauri-Proxima b (AC-C/Proxima b) are used to find possible trajectories towards Proxima b. The transfer is divided into a departure phase from AC-A/AC-B and an arrival phase to AC-C/Proxima b. Heteroclinic connections are then exploited using a patched restricted three-body problem method to connect the two phases. A grid search is applied on the optimization parameters to explore the design space, after which a genetic algorithm is applied to further optimize the link, focusing on minimization of the position, velocity, and time error at linkage. Futuristic sail configurations are used, including double-sided reflective sails and lightness numbers up to β = 1779. The design space exploration shows that a double-sided sail provides little improvement over a one-sided sail, mainly due to the constant sail attitude along the trajectories. Results from the genetic algorithm show that a transfer from the L_2-point in the AC-A/AC-B system to the L_1-point in the AC-C/Proxima b can be accomplished with a transfer time of 235 years for the one-sided graphene-based sail with a surface of 315×315 m^2 carrying a payload of 10 grams. A transfer from the L_2-point in the AC-A/AC-B system to the L_3-point in the AC-C/Proxima b, with a slightly smaller one-sided graphene-based sail (75×75 m^2,

[1]Graduate Student, Department of Astrodynamics and Space Missions, Faculty of Aerospace Engineering, timrotmans@gmail.com.

carrying a payload of 10 grams), results in a transfer time of 1025 years. For both sail configurations, the position error at linkage is kept below 1% of the total travel distance, the velocity error below 1% of the velocity at linkage, and the time error below 1% of the total transfer time.

Nomenclature

Roman symbols

$\mathbf{a}$	acceleration vector	$\hat{\mathbf{n}}$	sail normal vector
b	galactic latitude	$\mathcal{O}(\tilde{\mathbf{X}}, \tilde{\mathbf{Y}}, \tilde{\mathbf{Z}})$	observer frame
c	speed of light	P	period
e	eccentricity	P_0	last epoch of periastron
E	eccentric anomaly	$\mathcal{P}(\mathbf{x}, \mathbf{y}, \mathbf{z})$	rotating pulsating barycentric frame
$\mathcal{E}(\mathbf{j}_1, \mathbf{j}_2, \mathbf{j}_3)$	International Celestial Reference Frame	q_{1-10}	set of target conditions and sail attitude/configuration
G	gravitational constant	Q	Poincaré surface
$\mathcal{G}(\tilde{\mathbf{x}}, \tilde{\mathbf{y}}, \tilde{\mathbf{z}})$	galactic frame	$\mathbf{r}$	position vector
i	inclination	R	radius
$\mathcal{I}(\mathbf{X}, \mathbf{Y}, \mathbf{Z})$	inertial frame	$\mathcal{S}(\hat{\mathbf{r}}, \hat{\boldsymbol{\theta}}, \hat{\boldsymbol{\eta}})$	sail-centered frame
J_1, J_2, J_3	optimization objective functions	s	semi-major axis
l	galactic longitude	t	time
L	luminosity	T	temperature
L_1, L_2, L_3	colinear Lagrange points	u	binary control variable double-sided sail
L_4, L_5	triangular Lagrange points	U	effective potential in ERTBP
m	mass	$\mathbf{v}$	velocity vector
M	mean anomaly	$\mathbf{x}$	state vector
n	mean motion		

Greek symbols

α	cone angle	ρ	distance between primary bodies in the ERTBP
β	lightness number	σ	sail loading
δ	clock angle	Φ	state transition matrix
ϵ	lightness number conversion ratio parameter	Ψ	argument of periapsis
θ	true anomaly	$\boldsymbol{\omega}$	angular velocity vector
μ	mass parameter	Ω	longitude of the ascending node

Abbreviations and acronyms

AC-A	star Alpha Centauri A	DEC	declination (ICRS coordinates)
AC-B	star Alpha Centauri B	DV	decision variables
AC-C	star Alpha Centauri C	ERTBP	elliptic restricted three-body problem
AU	astronomical unit	RA	right ascension (ICRS coordinates)
CRTBP	circular restricted three-body problem	rev	revolutions

Subscripts

a	arrival system	d	departure system
A	Alpha Centauri A	$\oplus$	Earth
B	Alpha Centauri B	$\odot$	Sun
C	Alpha Centauri C	$2s$	double-sided sail

I. Introduction

While tracking a comet with his telescope in 1689, astronomer Jean Richaud came across the Centaurus constellation. For the first time, he noticed that the star known back then as Alpha Centauri was in fact a binary star system [1]. In 1839, 150 years later, astronomer Thomas Henderson determined the parallax of this binary system [2]: 747.1 milliarcseconds, or 4.37 lightyears away from the Solar system, making Alpha Centauri our closest stellar neighbor. Another 80 years later, in 1915, astronomer Robert T. A. Innes discovered Proxima Centauri [3], located at 4.25 lightyears from the Solar system, therefore taking on the title of being our closest neighbor. As of today, there is strong evidence that Proxima Centauri is in bound orbit about the binary system [4]. Moreover, two additional discoveries were made in the past ten years. At least two planets are in orbit about Proxima Centauri: Proxima b and Proxima c [5, 6]. One of these two, Proxima b, is a rocky planet in the habitable zone of Proxima Centauri, potentially bearing life.

Until today, there has been a vivid discussion about the probability of Proxima b containing life. It is important to note that many factors play a role in whether life could have formed on Proxima b or not [7, 8]. Two factors that are not beneficial for life-formation on a planet are addressed here. Firstly, Proxima b orbits a red dwarf, Proxima Centauri, which is much cooler than the Sun, resulting in a habitable zone closer to the star. This exposes Proxima b to high levels of radiation, flares, and mass ejections [9]. For a rocky planet in such an environment, keeping an atmosphere stable is difficult due to a large number of high-energy particles hitting the atmospheric particles. This process is called atmosphere stripping [9] and could be countered by a strong magnetic field. Secondly, there is the possibility that Proxima b is tidally locked with Proxima Centauri, similar to our moon is with the Earth. Such a configuration results in one hot and one cold side of the planet and is not beneficial for life formation. However, an atmosphere and potential winds could regulate surface temperatures to some extent. In-situ measurements of Proxima b's magnetic field and the star's surface activity would provide valuable information in the discussion about life formation on Proxima b. Ultimately, such research would help our understanding of life formation on rocky exoplanets. A mission to this system is thus endorsed by a strong scientific interest.

Breakthrough Initiatives proposed a mission to the Alpha Centauri system using photon sails.[1] The concept of photon sailing, also called solar sailing, was recently brought into practice when JAXA successfully launched the first sail in 2010 [10]. A photon sail consists of a highly reflecting, ultra-thin membrane attached to a payload. It uses the radiation pressure from a star to generate thrust and propel the spacecraft. The thrust force is proportional to the light's intensity and the sail's surface. The light particles, called photons, transfer their momentum to the sail and cause a small but continuous push in a specific direction, allowing the

[1] https://breakthroughinitiatives.org/initiative/3, access date: 18/10/2022

spacecraft to travel through space without the use of traditional fuels. The spacecraft can be controlled by adjusting the angle of the sail with respect to incoming radiation, changing the direction of the thrust. In the past ten years, more launched sailcraft followed, such as NASA's NanoSail-D2 [11], Planetary Society's Lightsail 1 and 2, [2] and the upcoming ACS3 (Advanced Composite Solar Sail System) mission[12]. The Breakthrough Starshot mission has a more futuristic nature than these current photon-sail missions, because it is an interstellar mission. It aims to send a swarm of ultra-lightweight sails with gram-sized payloads to Alpha Centauri to perform a flyby of the binary system. Using a 100 GW Earth-based laser array, the sails are propelled to 20% of the speed of light, reaching the system in a little over twenty years. Although the technology to launch such a mission is not yet within our grasp, the project initiated other research on photon-sail missions to Alpha Centauri. In references [13–15], several different mission scenarios are investigated. Using a futuristic graphene-based sail, they studied the possibility of getting captured in the binary system, and, trajectories towards Proxima Centauri using gravity assists. They computed trajectories that decelerate in the binary system by using the radiation pressure and a flyby of Alpha Centauri A. The trajectory then continues towards Proxima Centauri, and to get in bound orbit about Proxima Centauri, they calculated a maximum arrival speed in the Alpha Centauri A/B system of 5.7% of the speed of light. This results in a 75 years journey from Earth and an additional 46 years towards Proxima Centauri. In reference [16], comparable results are presented for a capture in the Alpha Centauri A/B system using the same sail configuration.

The research presented in this paper focuses on finding photon-sail trajectories starting from the colinear Lagrange points in the binary system to the colinear and triangular Lagrange points in the Proxima Centauri/Proxima b system. The elliptic restricted three-body problem (ERTBP) is applied to the two different systems: the *departure* system consists of the stars Alpha Centauri A (AC-A) and Alpha Centauri B (AC-B), and the *arrival* system consists of the star Proxima Centauri (AC-C) and planet Proxima b. Adequate connections between the two systems are sought for using a patched restricted three-body problem approximation method [17–19]. In this method, the two systems are "patched" together to find a transfer. The surface at which the two systems are patched is a Poincaré section in phase space, also called linkage surface. A transfer between the two systems is established using heteroclinic connections (connections between different Lagrange points). Such connections are constructed by using invariant manifolds; trajectories that asymptotically lead towards/away from the equilibrium points. The aim is to connect the unstable manifolds of the Lagrange points of the departure system, with the (artificial) stable manifolds of the Lagrange points in the arrival system. So the transfer is divided into a departure and an arrival phase. This approach has

[2]https://www.planetary.org/sci-tech/lightsail, access date: 18/10/2022

already proved to be successful in finding such links. In reference [19], it is used to find connections for a photon-sail mission from the Earth-Moon L_2 point to the Sun-Mars L_1 point. In reference [20], connections are established between a Sun-Earth L_2-halo orbit to a Sun-Mars L_1-halo orbit, and between a Sun-Earth L_1-halo orbit and a Sun-Mercury L_2-halo orbit. To find a proper link between the two systems, the error between the departure and arrival phase at the Poincaré section is evaluated. A numerical optimization problem unfolds in which the error in position, velocity and time is minimized. Similar as in reference [19], this work uses two techniques to solve this numerical problem: a grid search and a genetic algorithm. The grid search is used for a design space exploration and gives a first insight into the problem. With the knowledge of the design space exploration, the genetic algorithm is applied to further optimize the link between the systems.

This paper is structured in the following way. The first section gives an overview of the Alpha Centauri system, including all the relevant parameters of AC-A, AC-B, AC-C, Proxima b, and Proxima c. Then, the dynamical model is explained, including the reference frames used, the equations of motion for the photon-sail augmented ERTBP, the acceleration caused by radiation pressure, the used ephemerides, and the Lagrange points in both systems. The next section presents the methodology to solve the numerical problem. This includes an explanation of the patched restricted three-body problem model, the optimization problem, and the optimization methods. Subsequently, the design space exploration results are presented, containing the grid search results and conclusions. The final results of the optimization problem generated by the genetic algorithm are given in the next section, after which the conclusions of this research are presented.

II. Alpha Centauri System

As briefly mentioned in Section I, Alpha Centauri is a triple star system located at 4.37 light-years from the Sun [21]. AC-A and AC-B are both similar to our Sun in size and luminosity. They form a binary star system, mutually rotating around the barycenter, with a period of approximately 80 years [22]. In Table 1, all relevant parameters of the system are given. In Tables 2 and 3, the orbital elements of AC-A, AC-B and AC-C are presented. In reference [23], it is demonstrated with a high degree of confidence that the third star AC-C is in a bound orbit about the binary system. In that reference, an approximation of the orbital elements is given, although improved data was published more recently [24]. This data is provided in Table 3 and given in the departure observer frame O_d. This frame is explained in Section III.A. AC-C orbits the binary system at approximately 13,000 AU. AC-C is a red dwarf star with a smaller luminosity and mass than AC-A and AC-B. Figure 1 gives an overview of the orbits of all bodies of interest. Due to the enlarged orbits of the binary system and Proxima b, the figure provides the opportunity to visualize and comprehend the system.

At present, it has been confirmed that two planets are in orbit about AC-C: Proxima b and Proxima c

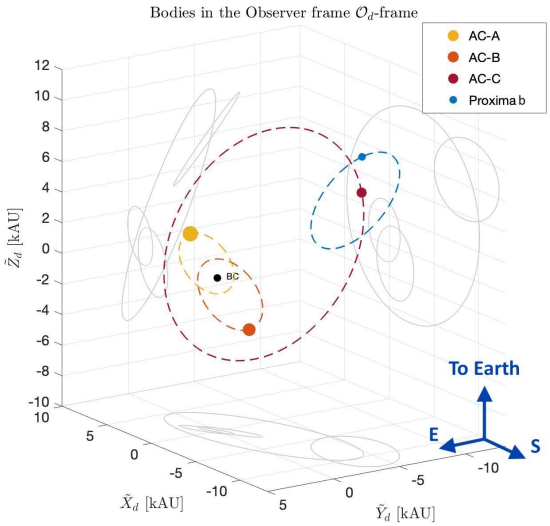

Figure 1. An overview of the positions and orbits of the three stars, including the assumed orbit of Proxima b, at reference epoch J2000. The orbit of AC-C is to scale. The orbits of AC-A and AC-B are enlarged by a factor 200. Proxima b's orbit is enlarged by a factor of 80,000.

Table 1. Parameters for the three stars within the Alpha Centauri system. The mass, luminosity and radius are expressed in solar units: $m_\odot$ = 1.989110 $*$ 10^{30} kg, $R_\odot$ = 6.9598 $*$ 10^5 km and $L_\odot$ = 3.854 $*$ 10^{26} W [21, 25, 26].

		AC-A	AC-B	AC-C	Sun	Unit
Mass	m	1.100	0.9070	0.1230	1	$m_\odot$
Luminosity	L	1.519	0.5002	0.0015	1	$L_\odot$
Radius	R	1.230	0.8570	0.1450	1	$R_\odot$
Avg. Temperature	T	5790	5260	3040	5770	K

Table 2. Orbital parameters for the binary system. The angles are measured relative to the Observer Frame O_d [24].

		AC-A	AC-B	Units
Semi-major axis	s	10.790	12.726	AU
Eccentricity	e	0.5208	0.5208	-
Inclination	i	79.32	79.32	deg
Longitude of ascending node	Ω	205.064	205.064	deg
Argument of periapsis	Ψ	232.006 + 180	232.006	deg
Mean anomaly	M	19.959	199.959	deg
Period	P	79.929	79.929	yr
Last epoch of Periastron	P_0	August 1955	August 1955	

Table 3. Orbital parameters for AC-C's orbit [24]. Epoch of periastron passage is relative to present. The angles are measured relative to the Observer Frame O_d.

		AC-C	Unit
Semi-major axis	s	8.2	kAU
Eccentricity	e	0.497	-
Inclination	i	124.9	deg
Longitude of the ascending node	Ω	165.0	deg
Argument of periastron	Ψ	151.0	deg
Period	P	511,000	yrs
Epoch of periastron	P_0	278,000	yrs

Table 4. Kepler elements, parameters, and size/mass estimations of Proxima b and c [5, 6, 27, 29, 30, 32]. The mass and radius are expressed in Earth's units: $m_\oplus$ = $5.972 * 10^{24}$ kg and $R_\oplus$ = 6371 km. Kepler elements are given in the observer frame O_a.

		Proxima b	Proxima c	Unit
Mass	m	1.3	7	$m_\oplus$
Semi-major axis	s	0.05	1.5	AU
Eccentricity	e	0.105	0.04	-
Inclination	i	Unknown	133	deg
Longitude of the ascending node	Ω	Unknown	331	deg
Argument of periastron	Ψ	310	Unknown	deg
radius	R	1.07	Unknown	$R_\oplus$
Period	P	11.186	1928	days

[27, 28]. The parameters for the two planets are presented in Table 4, given in the arrival observer frame O_a. This reference frame is addressed in Section III.A. Proxima b is an Earth-like, rocky planet located in the habitable zone. Data on the orbit of Proxima b is scarce, but in Table 4 a collection of the available data is presented, obtained from multiple sources [5, 27, 29, 30]. From the data in Table 4 it is clear that there are two unknown orbital elements: the inclination i and right ascension of the ascending node Ω. However, it is known that Proxima b does not transit AC-C [31], therefore an inclination of 90° (or close to 90) with the plane tangential to the line-of-sight is impossible. Thus, in this work an inclination of i = 45° is assumed.

Proxima c is the second confirmed planet, orbiting much further from AC-C [6, 28, 32]. It orbits AC-C at approximately 1.5 AU, far outside the habitable zone. Again, Table 4 provides the planets' specifications. Since Proxima c is outside of the habitable zone and not likely to be a rocky planet, it is of less interest to the scientific community. Additionally, several other planets within the Alpha Centauri system were claimed over the past years, including planets orbiting the binary system, although these have not been confirmed.

III. Dynamical Model

In this section, the dynamical model used in this work for a photon sail in the Alpha Centauri system is given. Section III.A provides a brief overview of all the reference frames used in this work. All frame

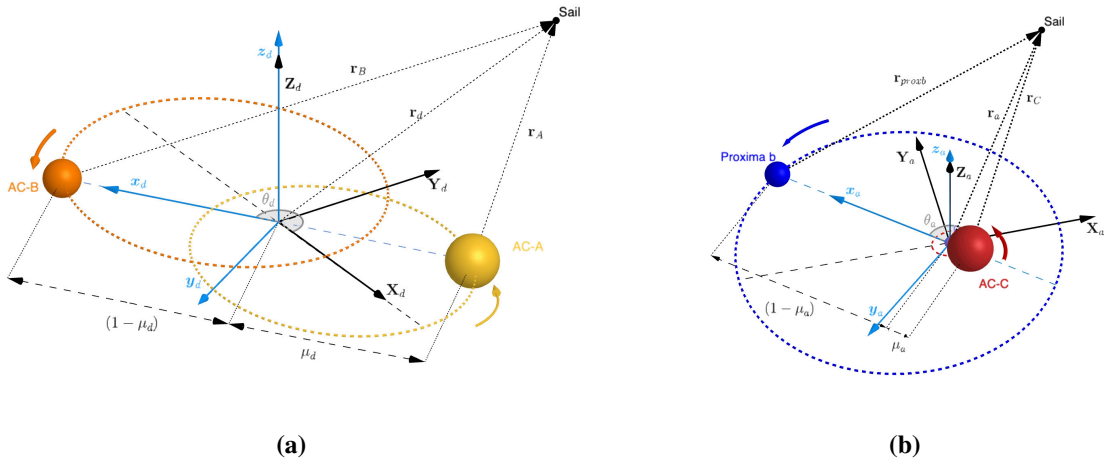

(a) (b)

Figure 2. Schematic representation of (a) the departure system, including the $\mathcal{I}_d(\mathbf{X}_d,\mathbf{Y}_d,\mathbf{Z}_d)$ and $\mathcal{P}_d(\mathbf{x}_d,\mathbf{y}_d,\mathbf{z}_d)$-frame , and (b) the arrival system, including the $\mathcal{I}_a(\mathbf{X}_a,\mathbf{Y}_a,\mathbf{Z}_a)$ and $\mathcal{P}_a(\mathbf{x}_a,\mathbf{y}_a,\mathbf{z}_a)$-frame.

transformations used for this work are given in the Appendices. Section III.B gives the equations of motion for a photon sail in the elliptic restricted three-body problem (ERTBP). The ERTBP is a modified version of the circular restricted three-body problem (CRTBP), used to describe the motion of a massless particles under the effect of two larger bodies that move in non-circular orbits. In Section III.C, the photon-sail acceleration model is defined using an ideal-sail model. To continue, Section III.D discusses the ephemerides data of the bodies in the Alpha Centauri system and how that data was obtained. Finally, Section III.E provides the Lagrange points of the departure and arrival systems.

A. Reference Frames

The first two frames that are introduced are inertial frames. Both inertial frames are non-rotating, fixed frames, with their origin in the barycenter of the two central bodies of the three-body problem considered. Frame $\mathcal{I}_d(\mathbf{X}_d,\mathbf{Y}_d,\mathbf{Z}_d)$ has its origin in the barycenter of stars AC-A and AC-B, see Figure 2a. The X_d-axis is aligned with the major axis of their elliptic orbits and is positive in the direction of AC-B's periastron. The Z_d-axis is aligned with the angular velocity vector $\boldsymbol{\omega}_d$, a vector originating in the barycenter and perpendicular to the orbital plane of AC-A and AC-B. The Y_d-axis completes the right-handed frame. Similarly, frame $\mathcal{I}_a(\mathbf{X}_a,\mathbf{Y}_a,\mathbf{Z}_a)$ has its origin in the barycenter of star AC-C and planet Proxima b, see Figure 2b. The X_a-axis is aligned with the major axis of Proxima's orbit and positive in the direction of the periastron. The Z_a-axis is aligned with the angular velocity vector $\boldsymbol{\omega}_a$, a vector originating in the barycenter and perpendicular to the orbital plane of AC-C and Proxima b. The Y_a-axis completes the right-handed frame.

Additionally, two observer frames are presented that prove to be helpful when describing the orbits

of celestial bodies. The $O_d(\tilde{\mathbf{X}}_d, \tilde{\mathbf{Y}}_d, \tilde{\mathbf{Z}}_d)$ frame, located in the barycenter of AC-A and AC-B, and the $O_a(\tilde{\mathbf{X}}_a, \tilde{\mathbf{Y}}_a, \tilde{\mathbf{Z}}_a)$ frame, located in the barycenter of AC-C and Proxima b. In both frames, the $\tilde{Z}$-axis points towards the observer, and axes $\tilde{X}$ and $\tilde{Y}$ are defined in the plane-of-the-sky (tangential plane), a plane perpendicular to $\tilde{Z}$, see Fig. 3 for a generalized depiction of an observer frame. If the body of interest is found on the Northern celestial sphere, the $\tilde{X}$-axis points towards the intersection between the tangential plane and a line through the Celestial Poles. If located in the Southern celestial sphere, which is the case for the Alpha Centauri system, the $\tilde{X}$-axis points away from this intersection, so that the negative $\tilde{X}$ direction is towards the intersection between the tangential plane and a line through the Celestial Poles. The $\tilde{Y}$-axis completes the right-handed frame. Furthermore, in astronomical data, the right ascension of the ascending node Ω of a celestial body is often measured starting from the $\tilde{X}$-axis towards the line of nodes. The inclination i represents the angle between the orbital and tangential planes. These definitions are also used in this research, see Fig. 3.

Furthermore, when working with the ERTBP (explained in Section III.B), it is convenient to define a rotating pulsating barycentric frame, an extension or variant of the synodic frame used for the CRTBP [33]. As a result of the eccentric orbits of the primary bodies, the distance between them and their angular rotation rate, expressed in an inertial frame, is non-uniform. The rotating pulsating barycentric frame accounts for this non-uniform rotation ω_i of the two central bodies by expanding its axes in accordance with the instantaneous distance ρ_i between the two primaries [33]:

$$\rho_i = \frac{s_i(1 - e_i^2)}{1 + e_i \cos\theta_i}, \qquad i = d, a \tag{1}$$

where the subscript i is used to distinguish between the departure and arrival system parameters. e_i is the eccentricity, s_i the semi-major axis, and θ_i the true anomaly. Due to the expanding and contracting nature of the frame, the distance between the primaries in this frame remains constant, as well as their locations on the x_i-axis. Consequently, it is possible to define the equations of motion of the ERTBP in a similar manner as for the circular problem. The equations of motion for the ERTBP are given in Section III.B. Again, two frames are introduced, with their origins in the barycenters of departure and arrival systems: $\mathcal{P}_d(\mathbf{x}_d,\mathbf{y}_d,\mathbf{z}_d)$ and $\mathcal{P}_a(\mathbf{x}_a,\mathbf{y}_a,\mathbf{z}_a)$. The $\mathcal{P}_d$-frame has its origin in the barycenter of AC-A and AC-B. Its x_d-axis is aligned with the line connecting the two primaries, positive in the direction of AC-B. The z_d-axis is aligned with the angular velocity vector $\boldsymbol{\omega}_d$, perpendicular to the $x_d y_d$-plane. The y_d-axis completes the right-handed reference frame. The $\mathcal{P}_a$-frame has its origin in the barycenter of AC-C and Proxima b. Its x_a-axis is aligned with the line connecting the two primaries, positive in the direction of Proxima b. The z_a-axis is aligned with

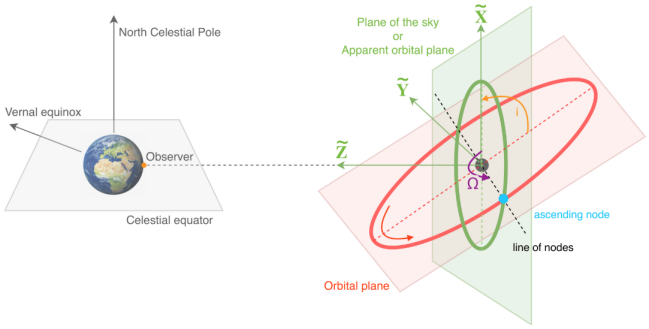

Figure 3. A general definition of the observer frame, where the $\tilde{Z}$-axis points towards Earth [34].

the angular velocity vector ω_a, perpendicular to the $x_a y_a$-plane. The y_a-axis completes the right-handed reference frame.

Two sail-centered frames are defined to describe the orientation of the photon sail. When the sail is located in the departure system, it is defined as $\mathcal{S}_d(\hat{\mathbf{r}}_A,\hat{\boldsymbol{\theta}}_A,\hat{\boldsymbol{\eta}}_A)$. When the sail is in the arrival system, it is defined as $\mathcal{S}_a(\hat{\mathbf{r}}_C,\hat{\boldsymbol{\theta}}_C,\hat{\boldsymbol{\eta}}_C)$. The sail-centered frame has its origin in the center of the sail; see Fig. 4a and Fig. 4b. The definitions of the three axes are given as:

$$\left(\hat{\mathbf{r}}_A = \frac{\mathbf{r}_A}{\|\mathbf{r}_A\|}, \quad \hat{\boldsymbol{\theta}}_A = \frac{\mathbf{Z}_d \times \hat{\mathbf{r}}_A}{\|\mathbf{Z}_d \times \hat{\mathbf{r}}_A\|}, \quad \hat{\boldsymbol{\eta}}_A = \frac{\hat{\mathbf{r}}_A \times \hat{\boldsymbol{\theta}}_A}{\|\hat{\mathbf{r}}_A \times \hat{\boldsymbol{\theta}}_A\|}\right) \tag{2}$$

$$\left(\hat{\mathbf{r}}_C = \frac{\mathbf{r}_C}{\|\mathbf{r}_C\|}, \quad \hat{\boldsymbol{\theta}}_C = \frac{\mathbf{Z}_a \times \hat{\mathbf{r}}_C}{\|\mathbf{Z}_a \times \hat{\mathbf{r}}_C\|}, \quad \hat{\boldsymbol{\eta}}_C = \frac{\hat{\mathbf{r}}_C \times \hat{\boldsymbol{\theta}}_C}{\|\hat{\mathbf{r}}_C \times \hat{\boldsymbol{\theta}}_C\|}\right) \tag{3}$$

where the $\hat{\mathbf{r}}_A$ and $\hat{\mathbf{r}}_C$ axes are the unit vectors of $\mathbf{r}_A$ and $\mathbf{r}_C$. $\mathbf{r}_A$ and $\mathbf{r}_C$ are vectors from stars AC-A and AC-C to the sailcraft, see Fig. 4a and Fig. 4b. The $\hat{\boldsymbol{\theta}}_A$-axis points in the direction perpendicular to a (theoretical) plane through $\mathbf{Z}_a$ and $\hat{\mathbf{r}}_A$. The $\hat{\boldsymbol{\theta}}_C$-axis points in the direction perpendicular to a (theoretical) plane through $\mathbf{Z}_d$ and $\hat{\mathbf{r}}_C$. The $\hat{\boldsymbol{\eta}}_A$-axis is perpendicular to the $\hat{\mathbf{r}}_A,\hat{\boldsymbol{\theta}}_A$-plane, the $\hat{\boldsymbol{\eta}}_C$-axis is perpendicular to the $\hat{\mathbf{r}}_C,\hat{\boldsymbol{\theta}}_C$-plane.

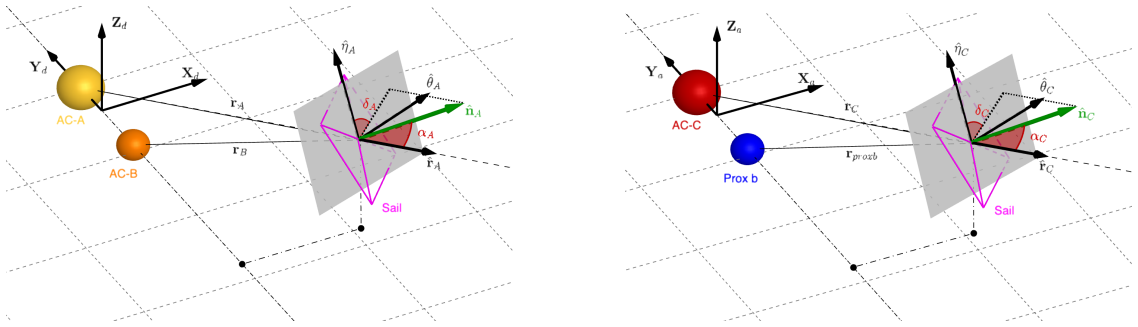

(a) **(b)**

Figure 4. Schematic overview of the relevant sail angles and vectors in the (a) departure system and (b) arrival system.

A galactic frame $\mathcal{G}(\tilde{\mathbf{x}},\tilde{\mathbf{y}},\tilde{\mathbf{z}})$ is defined, located in the Solar system with its origin in the center of the Sun, see Figure 5. The $\tilde{x}$-axis is aligned with a line connecting the Sun with the center of the Milky Way. The $\tilde{z}$-axis points towards the North Galactic Pole, the $\tilde{y}$-axis completes this right-handed frame and points in the direction of rotation of the Sun about the galactic center. From the perspective of an observer within the Solar system, its axes are fixed. Because of its static nature, the galactic frame is suited to describe the motion of stellar bodies in the sky. It can also be used to transform a state vector back and forward between the departure and arrival systems. Note that this transformation also takes the motion of the Solar system itself into account. In this research, two local galactic frames are defined, originating in the barycenter of AC-A/AC-B and in star AC-C, respectively: $\mathcal{G}_d(\tilde{\mathbf{x}}_d,\tilde{\mathbf{y}}_d,\tilde{\mathbf{z}}_d)$ and $\mathcal{G}_a(\tilde{\mathbf{x}}_a,\tilde{\mathbf{y}}_a,\tilde{\mathbf{z}}_a)$. The axes of both frames are aligned with those of the general $\mathcal{G}(\tilde{\mathbf{x}},\tilde{\mathbf{y}},\tilde{\mathbf{z}})$-frame. In addition to its $\tilde{\mathbf{x}}$, $\tilde{\mathbf{y}}$, $\tilde{\mathbf{z}}$-coordinates, the location of a body on the Celestial sphere can be expressed by the galactic longitude l and latitude b, see Fig. 5.

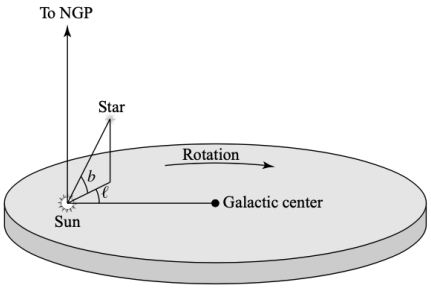

Figure 5. Definition of the galactic frame $\mathcal{G}$, obtained from [35].

Finally, the ICRS (International Celestial Reference System) coordinate system is adopted, with the corresponding frame $\mathcal{E}(\mathbf{j}_1,\mathbf{j}_2,\mathbf{j}_3)$ (this frame is in literature denoted by ICRF [36]). The ICRS is currently the standard reference system of the International Astronomical Union (IAU) [36, 37]. The origin of this frame is at the barycenter of the Solar system, and its axes are defined relative to extragalactic radio sources. These sources (quasars and active galactic nuclei) are so distant that they are assumed to be fixed on the celestial sphere. Therefore, the frame is fixed over time as well, so no associated reference epoch is necessary. Positions in this system are described with the right ascension RA and declination DEC of an object on the celestial sphere. The right ascension and declination are ICRS equivalents of the galactic longitude and latitude. Again, in this research, two local frames are defined that have their origin in the barycenter of AC-A/AC-B and in the center of star AC-C, respectively: $\mathcal{E}_d(\mathbf{j}_{d,1},\mathbf{j}_{d,2},\mathbf{j}_{d,3})$ and $\mathcal{E}_a(\mathbf{j}_{a,1},\mathbf{j}_{a,2},\mathbf{j}_{a,3})$.

B. Photon-Sail Augmented Elliptic Restricted Three-Body Problem

In departure and arrival systems, the primary bodies move in elliptic orbits about the local barycenter. Therefore, the same dynamical model is applied to both systems: the photon-sail augmented elliptic restricted three-body problem. The equations of motion for this model are defined below, again using subscript $i = d, a$ to distinguish between variables and parameters of both systems [33, 34, 38]:

$$\begin{aligned} \ddot{x}_i - 2\dot{y}_i &= \frac{1}{(1 + e_i \cos\theta_i)}\left(\frac{\partial U_i}{\partial x_i} + a_{x,i}\right) \\ \ddot{y}_i + 2\dot{x}_i &= \frac{1}{(1 + e_i \cos\theta_i)}\left(\frac{\partial U_i}{\partial y_i} + a_{y,i}\right) \\ \ddot{z}_i &= \frac{1}{(1 + e_i \cos\theta_i)}\left(\frac{\partial U_i}{\partial z_i} + a_{z,i}\right) \end{aligned} \tag{4}$$

where $a_{x,i}$, $a_{y,i}$, and $a_{z,i}$ are components of the sail acceleration vector $\mathbf{a}_{s,i}$, which is addressed in Section III.C. The independent variable is the true anomaly θ_i. The equations of motion are expressed in the pulsating rotating barycentric frame $\mathcal{P}_i$, that was introduced in Section III.A. The effective potential U_i in both systems can be expressed as [33]:

$$U_d = \frac{1}{2}\left(x_d^2 + y_d^2 + z_d^2\right) + \frac{(1 - \mu_d)}{r_A} + \frac{\mu_d}{r_B} - \frac{1}{2}(1 + e_d \cos(\theta_d))z_d^2 \tag{5}$$

$$U_a = \frac{1}{2}\left(x_a^2 + y_a^2 + z_a^2\right) + \frac{(1 - \mu_a)}{r_C} + \frac{\mu_a}{r_{proxb}} - \frac{1}{2}(1 + e_a \cos(\theta_a))z_a^2 \tag{6}$$

The equations of motion are written in dimensionless form using normalized units: the sum of the two masses as the unit of mass, the distance between the masses as the unit of length, and the inverse of the system's angular velocity $1/\omega_i$ as the unit of time. The mass parameter is introduced, $\mu_i = \frac{m_{2,i}}{(m_{1,i}+m_{2,i})}$, in which $m_{1,i}$ corresponds to the primary with the larger mass. In dimensionless form, the masses become $m_{1,i} = 1 - \mu_i$ and $m_{2,i} = \mu_i$, with corresponding locations on the x_i-axis $(-\mu_i)$ and $(1 - \mu_i)$, respectively. The period of both systems now becomes 2π.

C. Photon-sail acceleration

As was explained in the introduction of this section, an ideal-sail model is used. An ideal sail model uses a perfect, specular reflecting sail surface. This means that no absorption, re-rediation, or wrinkles in the sail are assumed [39]. This assumption results in a radiation pressure force that is perpendicular to the sail surface, in direction of the normal vector $\hat{\mathbf{n}}$. The performance of a photon sail can be expressed using its lightness number β [39]. The lightness number is a performance ratio that describes the radiation pressure

acceleration relative to the gravitational acceleration of the star. Both accelerations change with the inverse square of the distance to the star, so the lightness number is independent of this distance and therefore constant for a given sail configuration (under the assumption that the mass and luminosity of the Sun do not change). Alternatively, the lightness number can be expressed as follows [39]:

$$\beta = \frac{\sigma^*}{\sigma} \tag{7}$$

$$\sigma^* = \frac{L_\odot}{2\pi G m_\odot c} \tag{8}$$

where the sail loading σ describes the properties of the sail configuration (dependent on the sailcraft mass and area of reflectivity), G is the gravitational constant, and c is the speed of light. The relation between the Solar lightness number $\beta_\odot$ and the lightness number relative to another star depends on the mass and luminosity of the respective star [34, 40]. This relation can be expressed as $\beta_k = \epsilon_k \beta_\odot$, with the ratio ϵ_k defined as $\epsilon_k = \frac{L_k m_\odot}{L_\odot m_k}$. The subscript k is used to distinguish between the three stars AC-A, AC-B and AC-C ($k = A, B, C$)

The photon-pressure acceleration acting on a sail in a binary-star system is different than in a single-star system, because in a binary system, the sail will receive photons from two stars. Since the dynamical model used in this research consists of both a binary and a single-star system, it is necessary to define the acceleration in both cases.

First, a normal vector $\hat{\mathbf{n}}_k$ is introduced, defining the orientation of the sail with respect to the incoming sunlight. The normal vector's direction is expressed by using the cone and clock angles α_k and δ_k. The cone angle is the angle between the normal vector $\hat{\mathbf{n}}_k$ and the local $\hat{\mathbf{r}}_k$-axis. The clock angle is the angle between the $\hat{\boldsymbol{\eta}}_k$-axis and the projection of the normal vector on the plane perpendicular to vector $\hat{\mathbf{r}}_k$ (the $\hat{\boldsymbol{\theta}}_k, \hat{\boldsymbol{\eta}}_k$-plane). Defining the normal vector in the local sail-centered $\mathcal{S}_i$-frame results in:

$$\hat{\mathbf{n}}_d|_{\mathcal{S}_d} = \begin{pmatrix} \cos\alpha_A & \sin\alpha_A \sin\delta_A & \sin\alpha_A \cos\delta_A \end{pmatrix}^\top \tag{9}$$

$$\hat{\mathbf{n}}_a|_{\mathcal{S}_a} = \begin{pmatrix} \cos\alpha_C & \sin\alpha_C \sin\delta_C & \sin\alpha_C \cos\delta_C \end{pmatrix}^\top \tag{10}$$

The cone and clock angles of the departure system are measured with respect to star AC-A, so relative to vector $\hat{\mathbf{r}}_A$. In the arrival system, the cone and clock angles are measured with respect to star AC-C, so relative to vector $\hat{\mathbf{r}}_C$. To use the normal vectors in Eqs. 9 and 10, a frame transformation to the pulsating frame $\mathcal{P}_i$ is

necessary:

$$\hat{\mathbf{n}}_k|_{\mathcal{P}_i} = \left[\begin{array}{ccc} \hat{\mathbf{r}}_k & \hat{\boldsymbol{\theta}}_k & \hat{\boldsymbol{\eta}}_k \end{array} \right] \hat{\mathbf{n}}_k \Big|_{\mathcal{S}_i} \tag{11}$$

In the equations provided in the rest of this section, the frame notations $|_{\mathcal{P}_i/\mathcal{S}_i}$ are dropped. The photon-sail acceleration in the *arrival* system can then be expressed as follows [40]:

$$\mathbf{a}_{s,a} = \epsilon_C \frac{\beta_\odot (1-\mu_a)}{\|\mathbf{r}_C\|^2} (\hat{\mathbf{r}}_C \cdot \hat{\mathbf{n}}_a)^2 \hat{\mathbf{n}}_a \tag{12}$$

Since the sail cannot create an acceleration in the direction of the star from which it receives photons, the following constraint is enforced:

$$\hat{\mathbf{r}}_C \cdot \hat{\mathbf{n}}_a \geq 0 \tag{13}$$

In the departure system, the sail acceleration is defined as [34]:

$$\mathbf{a}_{s,d} = \mathbf{a}_A + \mathbf{a}_B \tag{14}$$

$$\mathbf{a}_{s,d} = \beta_\odot \left(\epsilon_\mathrm{A} \frac{1-\mu_d}{\|\mathbf{r}_\mathrm{A}\|^2} (\hat{\mathbf{r}}_\mathrm{A} \cdot \hat{\mathbf{n}}_d)^2 + \epsilon_\mathrm{B} \frac{\mu_d}{\|\mathbf{r}_\mathrm{B}\|^2} (\hat{\mathbf{r}}_\mathrm{B} \cdot \hat{\mathbf{n}}_d)^2 \right) \hat{\mathbf{n}}_d \tag{15}$$

In this case, a constraint is enforced to ensure that the non-reflective side of the sail never faces either one of the stars in the binary system during the transfer:

$$\hat{\mathbf{r}}_A \cdot \hat{\mathbf{n}}_d \geq 0 \quad \text{and} \quad \hat{\mathbf{r}}_B \cdot \hat{\mathbf{n}}_d \geq 0 \tag{16}$$

Furthermore, the expressions in Eq. 16 show that these constraints severely limit the maneuverability of the sail in the binary star system, because it will be difficult to not expose both sides to either one of the stars. Therefore, an additional sail model is investigated, based on other research done on photon sails in binary system [16, 34]: a sail that reflects photons on both sides. Where a regular one-sided sail in real life will reflect photons on one side and emit radiation on the backside (for thermal control), the hypothetical double-sided sail reflects photons from both sides. The ideal-sail model is then applied to both sides of the sail. The feasibility of the double-sided ideal sail model is not further addressed here. In the arrival system, applying a double-sided sail model does not change the sail acceleration definition given in Eq. 12. However, for the departure system, the model results in a slightly altered sail acceleration [34]:

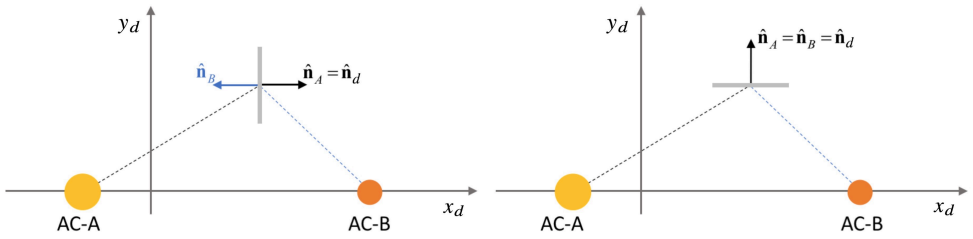

Figure 6. Schematic display of the working principle of the double-sided sail in the departure system [34].

$$\mathbf{a}_{s,d} = \beta_{\odot} \left(\epsilon_{\mathrm{A}} \frac{1-\mu_d}{\|\mathbf{r}_{\mathrm{A}}\|^2} \left(\hat{\mathbf{r}}_{\mathrm{A}} \cdot \hat{\mathbf{n}}_d\right)^2 + u * \epsilon_{\mathrm{B}} \frac{\mu_d}{\|\mathbf{r}_{\mathrm{B}}\|^2} \left(\hat{\mathbf{r}}_{\mathrm{B}} \cdot \hat{\mathbf{n}}_d\right)^2 \right) \hat{\mathbf{n}}_d \tag{17}$$

In eq. 17, a binary control variable u is introduced that can either take the value of -1 or 1. In case of a one-sided sail model, the binary value always takes the value 1, and the equation reduces to Eq. 15. In case of a double-sided sail, the value for u depends on the orientation of the sail with respect to AC-A and AC-B. This is defined by the flowdown in Eq. 18 and Fig. 6 provides further insight in the working principle of the binary control variable. If the sail is illuminated by AC-A on one side, and by AC-B on the other, the sail normal vector $\hat{\mathbf{n}}_B$ is flipped. In Eq. 17, this is done by setting the control variable to -1. In case both stars illuminate the same side, u is set to 1, and both normal vectors ($\hat{\mathbf{n}}_A$ and $\hat{\mathbf{n}}_B$) are aligned. The constraints on the orientation of the sail are again given by the expressions in Eq. 16, but the flexibility of the double-sided sail is improved over the one-sided sail.

$$u = \begin{cases} \text{one-sided} & 1 \\ \text{double-sided} & \begin{cases} 1 & \text{if } \hat{\mathbf{r}}_B \cdot \hat{\mathbf{n}}_d \geq 0 \\ -1 & \text{otherwise} \end{cases} \end{cases} \tag{18}$$

D. Ephemerides

The positions and velocities of the different bodies over time must be known in order to find a transfer trajectory. From the current positions and velocities (or at a specific reference epoch) of all bodies, it is possible to estimate their future positions at any given time. Figures 7a and 7b present the orbit of AC-C about the barycenter of Alpha Centauri. Figure 7a gives the orbit in 3D in the galactic reference frame $\mathcal{G}_d$. Fig. 7b gives the projected orbit of AC-C on the celestial sphere, in ICRS coordinates.

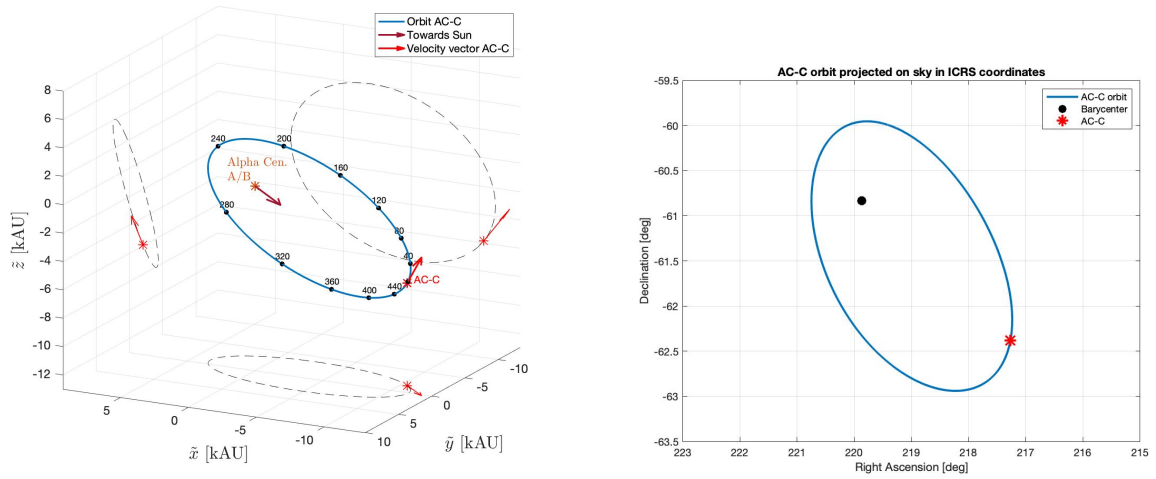

(a) **(b)**

Figure 7. (a) 3D presentation of AC-C's orbit about the barycenter of the system in the galactic $\mathcal{G}_d$ frame. The velocity vector of AC-C is given, as well as a vector pointing towards the Sun. The orbit is labeled with time points that represent millennia. The position and velocity of AC-C are in the year 2021. (b) AC-C orbit projected on the celestial sphere (plane of the sky) in ICRS coordinates.

The reference epoch t_0 is August 2035, when AC-A and AC-B are at periastron. Since the true anomaly of Proxima b is unknown, its periastron is also set to be at reference epoch t_0. Note that the period of Proxima b is short: 11.186 days. Many Proxima b revolutions fit in one departure system period, and transfer times of hundreds of years are considered reasonable. The assumption on the exact periastron of the arrival system is thus of minor influence on the results and therefore considered a safe assumption to make.

The relationship between the independent variable θ_i and dimensional time t_i, is indirectly given by Kepler's equation [35]:

$$M_i = E_i - e_i \sin E_i \tag{19}$$

where, as stated before, subscript i is defined as $i = d, a$. The variable E_i is the eccentric anomaly and M_i is the mean anomaly, calculated from $M_i = n_i(t_i - T_{0,i})$. Time $T_{0,i}$ is the periastron passage, which is different from t_0 since it refers to the last periastron passage, whereas t_0 is set to August 2035. To clarify this, the last periastron passage is defined as: $T_{0,i} = t_0 + rev_i * P_i$, where rev_i is the number of revolutions done by the primaries $rev = 1, 2, 3, .., rev_{i,max}$. Variable n_i is the mean motion of the system: $n_i = 1/P_i$. To calculate the dimensional time t_i from the independent variable θ_i, the first step is to calculate E_i using the relation in Eq. 14.

$$\tan\frac{\theta_i}{2} = \sqrt{\frac{1+e_i}{1-e_i}}\tan\frac{E_i}{2} \tag{20}$$

With Kepler's equation (Eq. 19), the mean anomaly can be calculated and used to compute the time after periastron ($t_i - T_0$).

E. Lagrange points

The Lagrange points in both the departure and arrival system are exploited to search for a transfer trajectory from AC-A/AC-B to the vicinity of Proxima b. The sail position can only be maintained at these points by enforcing the sail to an "edge-on" attitude. Using an edge-on attitude, the generated sail acceleration is zero, creating the possibility of using the Lagrange points for this purpose. An assumption is made that the sail will remain in this position only for a relatively short time so that the photon sail will not drift away from the Lagrange points regardless of the stability of the point. In Table 5, the five Lagrange points in both the departure and arrival system are given. These are calculated by setting the acceleration and velocity terms to zero in Eqs. 4.

Since the departure system consists of two stars, it is not possible to establish an edge-on position at the triangular Lagrange points, as photons from one of the two stars will always create a force on the sail. For this reason, only the colinear points are used for the departure phase. In addition to this, the fact that the L_1-point lies in between the two stars introduces another problem for a one-sided sail. A sail leaving that point will (almost) certainly face one of the stars with its non-reflective side for a period of time. Therefore, the L_1-point only serves as a departure location for trajectories with a double-sided sail and is considered an infeasible departure location for a one-sided sail. In the arrival system, which contains only one star, all five Lagrange points are used as arrival locations for both a one-sided and a double-sided sail.

Table 5. Lagrange points in the departure and arrival system.

	Departure		**Arrival**	
	x_d	y_d	x_a	y_a
L_1	0.058151154632749	0	0.978344822171941	0
L_2	1.212338004180330	0	1.021909480029498	0
L_3	-1.183815561294513	0	-1.000012920599003	0
L_4	0.041168983747797	0.866025403784439	0.499968990562389	0.866025403784439
L_5	0.041168983747797	-0.866025403784439	0.499968990562389	-0.866025403784439

IV. Methodology

This section presents the methodology employed to address the numerical problem of optimizing a transfer between the departure and arrival system. To determine a photon-sail transfer trajectory between the two star systems in Alpha Centauri, a method based on the patched restricted three-body problem approximation [18, 19, 41] is utilized. This technique is discussed in Section IV.A. An extrapolation method that reduces the

computational load of the arrival phase is explained in Section IV.B, referred to as "cut-off". The optimization problem, including its objectives and constraints, is addressed in Section IV.C. Finally, Section IV.D outlines the two optimization methods applied to solve the problem: a grid search and the genetic algorithm.

The sail configurations analyzed in this study are presented in Table **??**. Four sail configurations are evaluated: a single-sided and double-sided sail with two different lightness numbers. The lightness numbers for sail configurations 3 and 4 are based on sail configurations previously studied for photon sailing in Alpha Centauri [13, 16]. The lightness numbers for configurations 1 and 2 represent a lower limit that appeared to ensure sufficient acceleration and deceleration during the departure/arrival phases, while maintaining a reasonable transfer time. Due to the large distances between the systems, a reasonable transfer time is considered to be anywhere from 100-1000 years for this transfer. The lower limit is primarily imposed by the small luminosity of AC-C, which affects the relative lightness number β_C, and, therefore, the deceleration capability upon arrival at AC-C/Proxima b.

Table 6. The four different sail configurations evaluated in this paper, with the sail loading and lightness numbers for the Sun, AC-A, AC-B, and AC-C, using two different lightness numbers and both a one-sided and double-sided sail.

	Reflective sides	$\beta_\odot$	β_A	β_B	β_C	Sail loading $[g/m^2]$
Configuration 1	1	100	137.4	53.4	1.2	0.015
Configuration 2	2	100	137.4	53.4	1.2	0.015
Configuration 3	1	1779	2444.4	949.4	21.7	0.00086
Configuration 4	2	1779	2444.4	949.4	21.7	0.00086

A. Patched restricted three-body problem approximation method

The patched restricted three-body problem approximation is a method used to find transfer trajectories between the two different star systems in Alpha Centauri. The method used in this work is based on previous attempts to find photon-sail transfers between different restricted three-body problems [18–20, 41]. A schematic of the method is provided in Fig. 8. To connect the two systems, so called heteroclinic connections are exploited. Heteroclinic connections are trajectories between different equilibrium points and can therefore also be used to link different three-body problems. These connections are constructed by using manifolds. Manifolds are sets of trajectories that asymptotically lead towards or away from unstable equilibrium points. A manifold can be obtained by perturbing the state at the unstable equilibrium point and then propagating the state over time. The perturbation is applied in the direction of the stable and unstable eigenvectors of the Monodromy matrix. The Monodromy matrix is obtained by evaluation of the state transition matrix Φ after

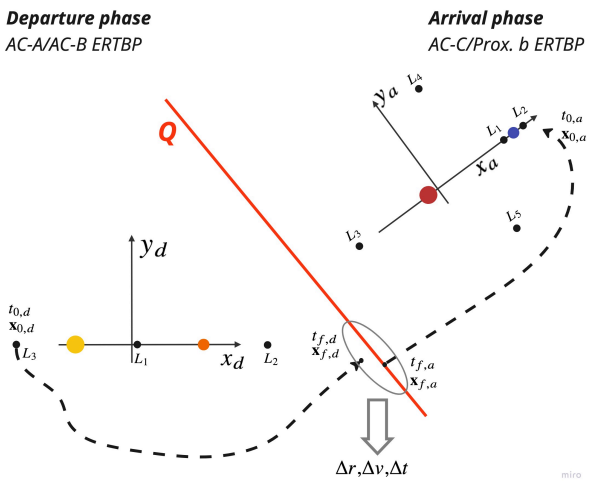

Figure 8. Schematic overview of the patched restricted three-body problem approximation method.

one period, $\Phi(\theta_0 + P)$ [34, 38]. The state transition matrix is constructed by linearizing the equations of motion around the equilibrium point, leading to a set of first-order differential equations. Exciting the state in the direction of the eigenvector associated with unstable motion results in motion away from the equilibrium. This induces the unstable manifold, for which the state is propagated forward in time. Similarly, exciting the state in the direction of the eigenvector associated with stable motion results in motion towards the point, providing the stable manifold. To compute the stable manifold, the state is propagated backward in time.

As was stated in III.E, for the initial conditions in the departure system, the colinear Lagrange points are considered. In the arrival system, all five Lagrange points are investigated as target conditions. The initial and target conditions define the Lagrange point from where the trajectory is propagated and the time at which the propagation is initiated. When at the Lagrange point, the sail is positioned with an edge-on attitude. The unstable manifolds from the colinear Lagrange points in the departure system are used to initiate motion away from the AC-A/AC-B system. In the arrival system, the stable manifolds are exploited to obtain motion towards the Lagrange points. However, the L_4 and L_5-points in the arrival system are stable and do not exhibit manifolds. But, manifolds can be artificially created by omitting the edge-on attitude. The accelerating force resulting from the solar radiation pressure then disrupts the stable motion around the equilibrium.

To add flexibility in the design of the transfers, a range of cone and clock angles is considered in the unstable and (artificial) stable manifolds. A constant sail attitude is assumed along these manifolds to limit the search space. Additionally, the non-autonomous nature of the ERTBP creates another dimension in the search space through the time-dependent true anomaly θ_i, at which a trajectory departs or arrives. The resulting manifolds form tube-like structures called photon-sail dedicated sets [18]. The manifolds must

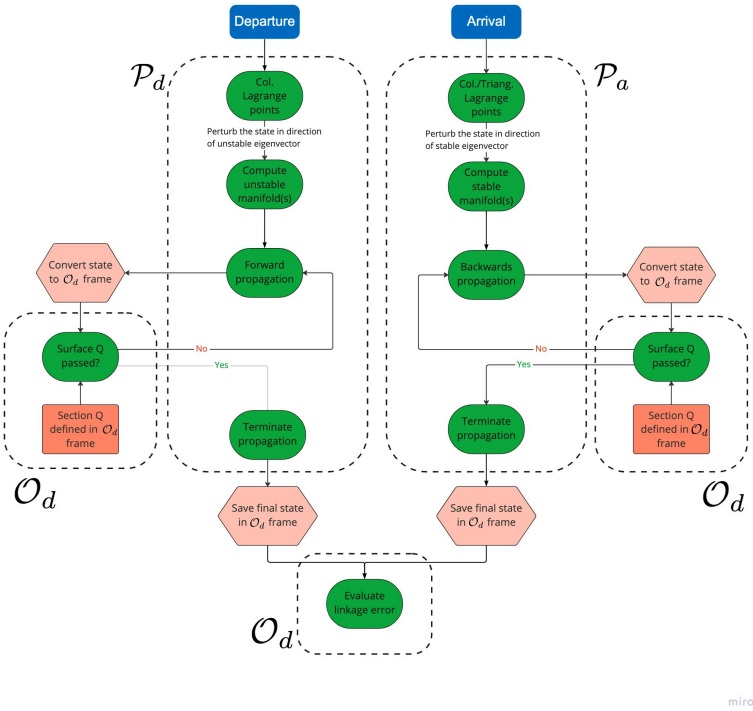

Figure 9. Schematic overview of the construction of the grid search, where for each grid point, photon-sail dedicated sets are used to search search for a heteroclinic connection.

then be connected in phase space and time to find a transfer trajectory. A detailed overview of the steps taken to find such transfers, using combinations of sail attitude and departure/arrival time, is given in Fig. 9. In the schematic, the reference frames associated with each step are also specified. In order to evaluate the connection between the photon-sail dedicated sets in phase space, the state of the sail is propagated to a Poincaré section (surface Q). Surface Q is defined in the departure observer frame $\mathcal{O}_d$. It is a section perpendicular to the line connecting the barycenter of the departure system with the barycenter of the arrival system, located exactly halfway along this line. The surface is chosen as the location in phase space where the state error, in terms of position, velocity, and time, can be evaluated. To reach this surface, the unstable manifolds of the Lagrange points in the departure system are propagated forward in time up to surface Q. In the arrival system, the (artificial) stable manifolds of the Lagrange points are propagated backwards up to surface Q. The error at surface Q is calculated by comparing the state $\mathbf{x}_{f,d}$ and time $t_{f,d}$ at the end of the unstable manifold with the state $\mathbf{x}_{f,a}$ and time $t_{f,a}$ at the end of the (artificial) stable manifolds. The evaluation of the error can be used to determine whether a heteroclinic connection exists between the departure and arrival systems, given the initial/target conditions $\mathbf{x}_{0,i}$ and $t_{0,i}$. The process of evaluating the connection between the photon-sail dedicated sets is crucial in determining the feasibility of a transfer trajectory between

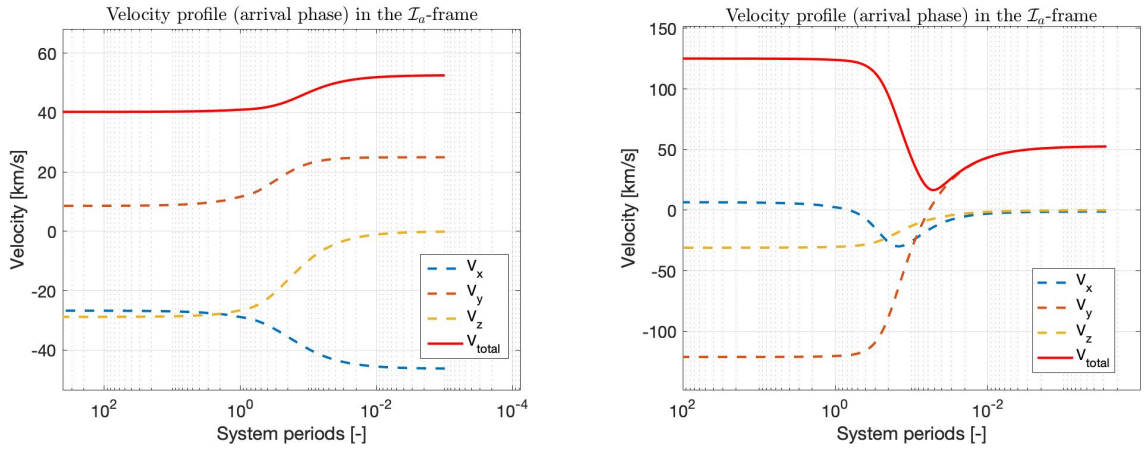

Figure 10. (a) A typical example of the velocity profile over time for a trajectory reaching surface Q, using sail configuration 1. (b) A typical example of the velocity profile over time for a trajectory reaching surface Q, using sail configuration 3. Both trajectories are given in the $\mathcal{I}_a$-frame and propagated backward in time with a tolerance of 10^{-11}.

the two systems. The aim is to find a set of initial/target conditions for the sail that will result in a successful transfer trajectory. By propagating the state of the sail to surface Q, and evaluating the error at that point, it is possible to identify which initial/target conditions will result in a successful transfer. It must be noted that not all initial/target conditions result in a trajectory crossing surface Q. In such a case, the final state of that trajectory will automatically produce a large error, so that the corresponding initial/target conditions are not further considered.

B. Arrival system cut-off

A challenge when searching for transfer trajectories lies in the computation cost associated with the arrival phase. This is due to the short period of the arrival system (11.186 days) relative to the transfer time, which results in the need to propagate the state of the sail over numerous system revolutions, which can be up to thousands. The numerical integration process, using Matlab's inbuilt *ode*45 solver, becomes time-consuming as a result. On the other hand, the departure system, with a period of approximately 80 years, requires less computational effort.

It is common practice when doing numerical simulations to make a trade-off between computation time and accuracy. Using a low-accuracy integration method can save time at the cost of less accurate results. In this work, the challenge of reducing computation time is solved by using an state extrapolation method, instead of using a low-accuracy integration. The developed method is used to approximate the state and time of the

sail at surface Q without having to propagate the entire (artificial) stable manifold. First, the state of the sail in the $\mathcal{P}_a$-frame is defined as $\mathbf{x}_a(t_a) = \begin{bmatrix} x_a & y_a & z_a & \dot{x}_a & \dot{y}_a & \dot{z}_a \end{bmatrix}^T$, while the estimated state is denoted as $\overline{\mathbf{x}}_a(\bar{t}_a)$. The foundation of the method is based on the observation that when backward propagating the state vector, using different target conditions, most trajectories converge to a constant velocity within a short period of propagation time, as seen from the inertial $\mathcal{I}_a$-frame. This can be illustrated by the velocity profiles of two example trajectories of a one-sided sail (sail configurations 1 and 3) in Fig. 10, in which, due to the backwards propagation, the constant velocity phase appears on the left side of the plot. Following the direction of motion (so not the direction of the backward propagation), the sail is approaching the arrival system with an almost constant velocity. When close enough to the primary bodies, the gravitational and solar accelerations start to have more effect on the trajectory and the constant velocity phase is breached. It is important to note that the velocity profile is dependent on factors such as the sail attitude and target conditions, however, the behavior of most trajectories remains consistent; a long, constant velocity phase upon approach, until getting in close enough range of the primary bodies to be affected by the solar radiation pressure and gravity.

A state extrapolation technique is applied in the arrival phase to reduce its computational load. When backwards propagating the (artificial) stable manifold, it is assumed that the velocity v_{cutoff} and its x, y, and z components reach a constant value at time t_{cutoff}. The time t_{cutoff} is determined by setting a threshold on the acceleration resulting from the gravitational pull of AC-C (a_{cutoff}), since the velocity depends on the target velocity and the accelerations acting on the sail. The state is backward propagated until the threshold is met, indicating that the sail is sufficiently far in its transfer trajectory, initiating the constant velocity phase. The propagation is then terminated at this point, referred to as a "cut-off." The state and time at surface Q are then estimated by linear extrapolation of the state at the cut-off point up to surface Q. The sail is thus assumed to move in a straight line between the cut-off point and surface Q. The time at which the extrapolated trajectory reaches surface Q is determined by dividing v_{cutoff} by the distance between the cut-off point and section Q. Therefore, the state and time at which the sail reaches surface Q, can be analytically approximated based on the state and time at the cut-off point.

To prevent that the linear extrapolation method produces erroneous results, the error of the method is assessed. It is important to realize that it is impossible to calculate the true error resulting from a numerical computation when no real-time data or measurements exist. However, the error of a lower accuracy method can be evaluated by comparing it to a benchmark run with a known higher accuracy. Therefore, a high accuracy benchmark is computed with absolute and relative tolerances of 10^{-11}, using the $ode45$ integrator in Matlab. The benchmark is propagated in full, until it reaches surface Q. For redundancy reasons, the benchmark consists of ten different trajectories. Each of these trajectories is propagated using a different set q, consisting

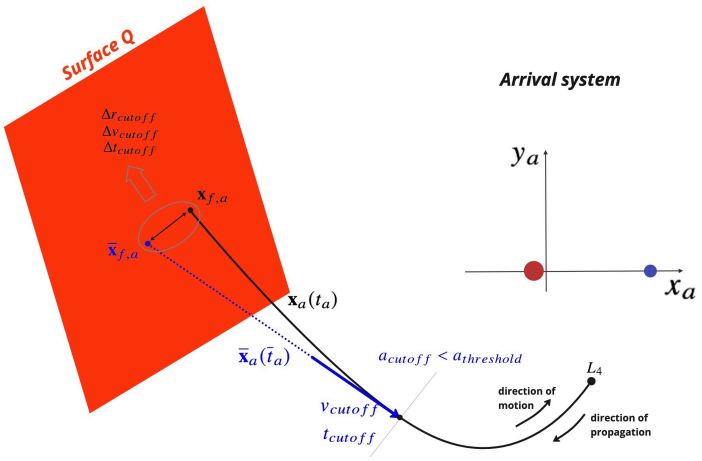

Figure 11. Schematic of the arrival system cut-off method. The blue dotted line represents the estimated state, extrapolated from the cut-off point.

of a specific target condition, sail attitude and sail configuration. Each set is indicated by a subscript from one to ten ($[q_1, q_2, ..., q_{10}]$), corresponding to the ten different combinations of target condition, sail attitude and configuration. This leads to ten different benchmark states at surface Q: $[\mathbf{x}_{f,a1}, \mathbf{x}_{f,a2}, ..., \mathbf{x}_{f,a10}]_{bench.}$. Then, the extrapolation method is tested against these benchmark trajectories. This is done by using the same sets q_{1-10}, but this time a cut-off is performed and the state extrapolated, following the above explained method, so that ten estimated states at surface Q are obtained: $[\bar{\mathbf{x}}_{f,a1}, \bar{\mathbf{x}}_{f,a2}, ..., \bar{\mathbf{x}}_{f,a10}]_{extr.}$. The estimated states are compared to their corresponding benchmark run and the differences are referred to as cut-off errors: Δr_{cutoff}, Δv_{cutoff}, and Δt_{cutoff}. Furthermore, the estimated states are computed using different tolerances for the propagation until cut-off. So, for each tolerance, the same sets q_{1-10} are used and the average over the ten cut-off errors is calculated and plotted in Fig. 12.

To complete the analysis, the extrapolated state method is also compared to a low-accuracy integration method. For the low-accuracy integration method, the state is again propagated in full (until section Q), but higher tolerances are used than for the benchmark. The procedure is identical to the one used for the extrapolation method. The same ten sets q_{1-10} are used for the propagation of ten trajectories, leading to 10 final states at surface Q: $[\mathbf{x}_{f,a1}, \mathbf{x}_{f,a2}, ..., \mathbf{x}_{f,a10}]_{low}$. At surface Q, the differences with the benchmark are again calculated in position, velocity and time. This process is repeated for each tolerance, ranging from 10^{-10} to 10^{-6}. The results are displayed together with the estimated (extrapolated) state results in Fig. 12. It is evident that the extrapolated state $\bar{\mathbf{x}}_{f,a}$ provides solutions that are closer to the benchmark than those obtained through full propagation with looser tolerances. The long propagation time of full propagation results in significant accumulation of numeric (truncation) errors when a looser tolerance is used. Although this is

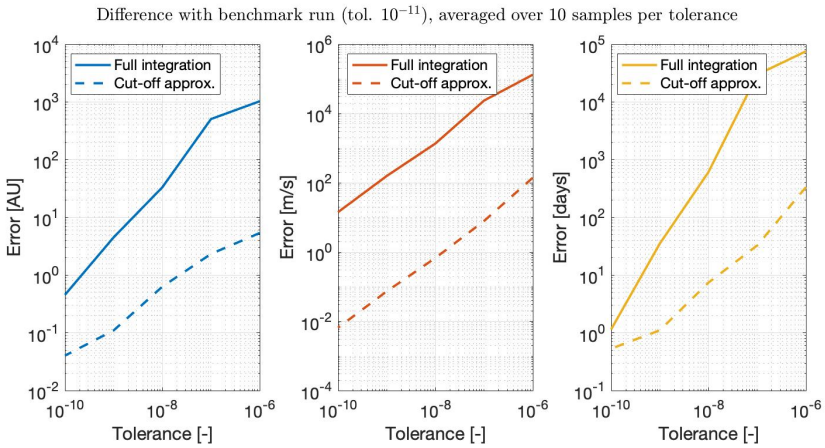

Figure 12. The error analysis for the extrapolation method (dotted lines) and for the lower accuracy propagation (straight lines). From left to right, the errors in distance, velocity and time are given.

a well-known phenomenon in numeric simulation, it is remarkable that the errors from the extrapolation method are much smaller. These results support the hypothesis of the extrapolation method, which states that the sail moves (almost) in a straight line through space with a constant velocity, until it comes within a certain range from the primary bodies. Therefore, the errors from the extrapolation method are smaller than the numerical errors from lower accuracy propagation, when compared to the high accuracy benchmark.

Furthermore, Fig. 13 displays the average run-time of all ten trajectories per tolerance, for both the extrapolation and the low-accuracy method. The same computer (2.2 GHz Quad-Core Intel Core i7) was used for all trajectory propagations. The extrapolated state reduces computation time by a factor of 15-40, depending on the tolerances. This reduction in runtime, combined with the much smaller errors resulting from the state estimation method, warrants the use of this method to find a transfer. In addition, when looking only at the cut-off errors (extrapolated state errors), a significant decrease in error is observed when lowering the tolerance. But, lowering the tolerances has far less impact on runtime, as can be seen from Fig. 13. Therefore, this work uses the state extrapolation method with a tolerance of 10^{-10} for the computations of the arrival phase.

C. Optimization problem

The objective of the optimization problem that is solved in this research is to minimize the errors at linkage. The first two errors are defined as the Euclidean norm difference between the states from both phases at surface Q (position and velocity). The third error is the difference in the exact time at which both phases pass surface Q. The following sections will further explain the objective functions, constraints, and decision variables.

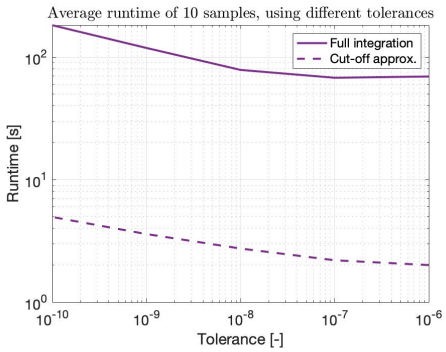

Figure 13. Average runtime from the error analysis for the extrapolation method (dotted lines) and the lower accuracy propagation (straight lines).

1. Objectives

To find a suitable transfer trajectory, three objectives are introduced that need to be minimized. The objectives are defined as the errors on the link surface Q: position error Δr, velocity error Δv, and time error Δt. The position and velocity errors are calculated using the Euclidean norm difference of the departure and arrival states at surface Q. The time error is calculated in days by subtracting the Julian Date at which the departure phase passes surface Q from the Julian Date at which the arrival phase passes surface Q. The three objectives are thus given as follows:

- $J_1 = \left\|\mathbf{r}_{\mathrm{f,d}} - \mathbf{r}_{\mathrm{f,a}}\right\|$ [AU]
- $J_2 = \left\|\mathbf{v}_{\mathrm{f,d}} - \mathbf{v}_{\mathrm{f,a}}\right\|$ [km/s]
- $J_3 = \left\|t_{\mathrm{f,d}} - t_{\mathrm{f,a}}\right\|$ [days]

It is important to note that the error in sail attitude at surface Q is not considered in the optimization. This means that at surface Q, a sudden, rapid change in sail attitude is allowed. For a real-life mission scenario, the attitude rate of change might be limited and a sudden change not possible. To solve this, a transition phase could be added in between the departure and arrival phase, in which the sail is allowed to slowly change its attitude. To limit the complexity of the computation in this research, such an approach is not used. The impact of this design choice on the final trajectory and results is not expected to be significant.

2. Constraints

A first set of constraints on the sail attitude was introduced in Section III.C (by Eqs. 13 and 16) and are restated here. These constraints are enforced to prevent the non-reflective side of the sail from facing one of the stars. For all sail configurations the constraints are given by:

$$\hat{\mathbf{r}}_C \cdot \hat{\mathbf{n}}_a \geq 0 \tag{21}$$

$$\hat{\mathbf{r}}_A \cdot \hat{\mathbf{n}}_d \geq 0 \quad \text{and} \quad \hat{\mathbf{r}}_B \cdot \hat{\mathbf{n}}_d \geq 0 \tag{22}$$

To simplify the problem, the constraints in Eqs. 21 and 22 are only enforced while the sail remains in the respective systems until surface Q is passed. This means, for example, that while the sail trajectory is propagated in the departure system, it is allowed to face AC-C with its backside. Similarly, during arrival phase the sail is allowed to face AC-A and AC-B with its backside.

Another set of constraints must be enforced to prevent the sail from passing one of the stars too closely. Although a significant sail acceleration can be obtained with close stellar flybys [42], the temperature of the sail can also increase to harmful levels. Therefore, a minimal distance is set to prevent the sail from heating up too much. Based on values obtained from literature [14, 16], a minimum safe distance of five stellar radii is used in this research:

$$\mathbf{r}_A > 5 * R_A$$

$$\mathbf{r}_B > 5 * R_B$$

$$\mathbf{r}_C > 5 * R_C$$

where R_d represents the radius of the respective star.

3. Decision variables

Six variables are used to tune the trajectories so that a smooth link at surface Q can be found. These six variables (DV) are the cone and clock angle during each phase (α_{A},δ_A,α_{C},δ_C) and arrival/departure time (t_d and t_a):

$$DV = \begin{bmatrix} \alpha_{\mathrm{A}} & \alpha_{\mathrm{C}} & \delta_A & \delta_C & t_d & t_a \end{bmatrix} \tag{23}$$

The bounds on the cone and clock angles during both phases are the following: $-90^\circ \leq \alpha_A, \alpha_C \leq 90^\circ$ and $0^\circ \leq \delta_A, \delta_C \leq 180^\circ$. As described in the introduction, this work is inspired by the Breakthrough Starshot project, which would, in a best-case scenario, launch its sails in 2036, resulting in an arrival at the Alpha Centauri system around 2056. However, it was already shown [4, 16] that to get captured in bound orbit about AC-A or AC-B, which is a necessity when starting from one of the Lagrange points, longer travel times should be expected (up to 80 years). Therefore, it is more reasonable to postpone the launch window of the mission investigated here to a window in a more distant future. So the bounds on the departure time from the

Lagrange points are set to $01/01/2095 \leq t_d \leq 01/01/2195$. The bounds on the arrival time depend on the sail configuration since a larger lightness number will result in shorter transfer times, and thus, a different arrival window is used for either lightness number in Table 6. For sail configurations 1 and 2, the arrival time is set to $01/01/3042 \leq t_a \leq 01/01/3122$. For sail configurations 3 and 4, the arrival window is bounded by: $01/01/2330 \leq t_a \leq 01/01/2420$. Note that the search space for the departure and arrival time is slightly larger than one period of the departure system. This is intentionally chosen to investigate the impact of the true anomaly θ_d on the transfer.

D. Optimization methods

The first step of the optimization process is a design space exploration. This is executed with a grid search to systematically explore the solution space by dividing all six decision variables into an equally-spaced grid of $k_1 \times k_2 \times k_3$ points. The cone and clock angles are divided into a grid of $k_1 = 35$ and $k_2 = 15$ points, respectively. The departure/arrival times are divided into $k_3 = 12$ points. Each combination of decision variables is then used to compute a transfer for which Δr, Δv, and Δt are assessed. Furthermore, taking the time error at Q into account in the design space exploration is computationally expensive, and, therefore, the results of the exploration focus mainly on the link error in position and velocity. After this exploration, a genetic algorithm is used to further optimize the link at surface Q and to also minimize the time error.

The software used to solve this numerical problem is Matlab's implementation of a multi-objective genetic algorithm *gamultiobj.m*. Three genetic algorithm parameters are tuned to fit best to this specific optimization problem. These parameters are the population size, the number of generations, and the crossover rate. The tuning of these parameters is done by investigating different values for each one, while keeping the default value for the other two parameters. The final settings are listed below.

- population size: 2000
- number of generations: 120
- crossover fraction: 0.8

To improve redundancy, the algorithm uses five different seeds[3] (with the Mersenne Twister random number generator in Matlab[4]) to initialize the population. For the sake of simplicity, the seeds in this paper are referred to as seed one to five, while their true values are given in brackets in the footnote.

[3]The seed numbers for sail configuration 1: seed 1 ["4"], seed 2 ["12"], seed 3 ["43"], seed 4 ["58"], and seed 5 ["12345"]. The seed numbers for sail configuration 3: seed 1 ["4"], seed 2 ["14"], seed 3 ["27"], seed 4 ["55"], and seed 5 ["67"]

[4]https://nl.mathworks.com/help/matlab/ref/rng.html

V. Design space exploration

The results of the design space exploration are presented in Tables 7-10. Each table represents a different sail configuration (defined in Table 6) and provides the best found links between all combinations of initial and target locations. In the tables, the absolute position and velocity errors (in AU and km/s) are given, as well as a normalized error percentage. The position error is normalized by comparing the absolute error to the distance between the barycenters of the two systems. The normalized velocity error is computed by comparing the absolute velocity error to the velocity magnitude of the sailcraft at surface Q. The best solution for each combination of initial/target location is defined by minimizing the sum of the normalized error percentages: $\min.(\Delta r[\%] + \Delta v[\%])$.

The first thing to notice is that there is no difference between the one-sided sail and the double-sided sail configurations, except that the L_1-point becomes a feasible departure location for the double-sided sail configuration. This can be explained by recalling that the double-sided nature of the sail will provide additional maneuverability in the double-star system. But, it is especially beneficial when the sail is close to, or, in between of the two stars. But by using large lightness numbers in combination with a constant sail attitude, most trajectories departing from L_2 and L_3 will quickly spiral outwards (as seen from a pulsating rotating frame), away from the two primary bodies. In this way there is not much time to exploit the benefits of having a double-sided sail. This is visually represented in Fig. 14, where trajectories leaving the departure L_2 are plotted in the O_d-frame. For a lightness number of $\beta = 0.05$, trajectories propagated for 80 years remain in proximity of the two stars, with the sail still moving in a bound trajectory. In comparison, the other two plots in Fig. 14 show that for substantially larger lightness numbers, considered for configurations 1-4, the sail travels almost in straight lines away from the stars. This behavior can be further explained by looking at Eqs. 7 and 8. With these large lightness numbers, the solar radiation pressure overcomes the gravitational attraction, and the sail can move 'freely'. So the grid search contains the exact same trajectories for both a one-sided and a double-sided sail, without using the benefits of the double-sided sail because of the constant sail attitude and the large lightness numbers. A sail with a smaller (currently more realistic) lightness number (as shown in the left plot of Fig. 14) in the departure system will stay close to the two stars for a longer time, because gravity has more effect on the spacecraft. In that case, the double-sided sail could provide additional benefits that are not exploited by a sail with the lightness numbers used in this research.

Furthermore, the results from Tables 7-10 show that the relative error is much larger for the velocity than for the position in most cases. It is difficult to find a matching velocity link at surface Q while also maintaining an appropriate position link. This is because, during the departure phase, the sail is accelerated to higher velocities than it can be decelerated during the arrival phase. The main reason for this is the dimness of

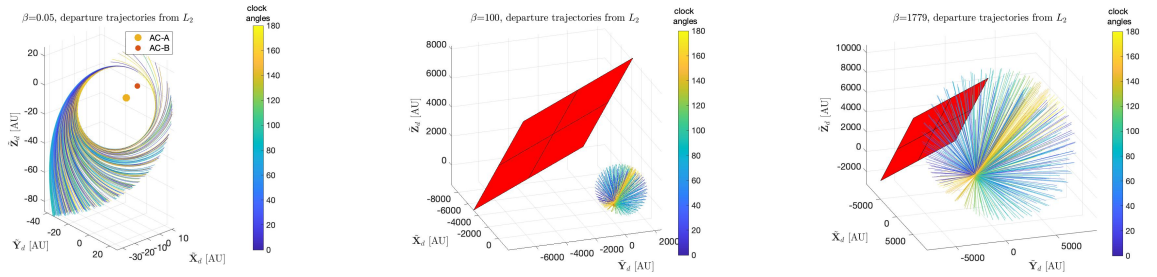

Figure 14. Example trajectories leaving L_2 in the O_d-frame with varying cone and clock angles. Initial conditions for all three figures are the same, except for the lightness number. The start of the propagation is at periastron in the year 2035. (a) $\beta = 0.05$, (b) $\beta = 100$, and (c) $\beta = 1779$. The color represents the clock angle variation. The trajectories are propagated over one departure system period (~80 years).

AC-C, while having a relatively large mass. Table 1 shows that its mass is approximately eight times smaller than the Sun's, but its luminosity is approximately 665 times smaller than the Sun's. This results in the very small relative lightness number shown in Table 6 and is the reason that the sail is less capable of decelerating during the arrival phase. The results presented in Fig. 20 support this conclusion. These boxplots contain the velocities at surface Q from all the trajectories in the grid search for each initial/target location (trajectories that do not pass surface Q are discarded). From these plots it is clear that the backward propagated (artificial) stable manifolds from the arrival system have smaller velocities at surface Q. Furthermore, little variation is observed between Lagrange points in the arrival system. But, the choice of departure location has a much larger impact on the velocity at surface Q. Care must be taken in drawing conclusions from the boxplot only for two reasons. First, the boxplots provide information on the probability that a good velocity link can be found between certain initial/target locations. However, a low probability does not necessarily mean that a link can not exist at all between these initial/target locations. Secondly, the boxplots do not consider the position errors. But, the boxplots do provide useful insight in this optimization problem and show the complexity of finding a proper velocity link.

Tables 7-10 and Fig. 20 show that, for both lightness numbers, departing from the L_1-point (while using a double-sided sail) does not provide any improvement over departing from the L_2 and L_3-points. In fact, because the sail is very close to both stars when departing from L_1, the velocity build-up is too large to find a proper connection with the arrival phase. Therefore, based on these preliminary results, it is concluded that the double-sided sail does not provide a benefit over a one-sided sail for the used set-up. So, only sail configurations 1 and 3 are chosen for further optimization. The boxplots in Fig. 13 show that the highest probability of finding a good velocity link is given by departure from the L_2-point (for both sail configurations 1 and 3). This is also observed in Tables 7-10, where for each sail configuration, the smallest velocity errors

are found for departures from the L_2-point. As was concluded previously, the boxplots show less obvious differences for the target points. But, when looking at the results in Tables 7 and 9, the most promising combinations are: L_2 to L_3 for sail configuration 1, and L_2 to L_1 for sail configuration 3. Therefore, those initial/target locations are chosen for further optimization. The genetic algorithm is used to investigate whether the gap in position/velocity error can be further closed, whilst also minimizing the time error at surface Q, which was not taken into account in this design space exploration.

Table 7. The results of the design space exploration for sail configuration 1 (one-sided, $\beta = 100$). The errors at linkage Δr and Δv are given in AU and km/s, as well as in their error percentages. The best result is marked in orange.

			Arrival									
	Location		L_1		L_2		L_3		L_4		L_5	
			AU - km/s	%	AU - km/s	%	AU - km/s	%	AU - km/s	%	AU - km/s	%
Departure	L_1	Δr	-	-	-	-	-	-	-	-	-	-
		Δv	-	-	-	-	-	-	-	-	-	5.83
	L_2	Δr	138.95	1.14	177.83	1.46	177.16	1.46	436.92	3.60	187.15	1.54
		Δv	2.81	5.40	2.72	5.28	1.85	3.55	3.21	5.99	5.32	5.83
	L_3	Δr	435.09	3.58	399.48	3.29	438.61	3.61	467.45	3.85	162.88	1.34
		Δv	12.52	7.97	4.46	4.96	4.55	8.50	9.93	6.46	4.04	4.51

Table 8. The results of the design space exploration for sail configuration 2 (double-sided, $\beta = 100$). The errors at linkage Δr and Δv are given in AU and km/s, as well as in their error percentages. The best result is marked in orange.

			Arrival									
	Location		L_1		L_2		L_3		L_4		L_5	
			AU - km/s	%	AU - km/s	%	AU - km/s	%	AU - km/s	%	AU - km/s	%
Departure	L_1	Δr	476.39	3.92	304.01	2.50	392.13	3.23	377.86	3.12	162.01	1.33
		Δv	14.45	8.82	13.43	8.04	14.89	7.22	11.32	5.99	15.93	9.49
	L_2	Δr	138.95	1.14	177.83	1.46	177.16	1.46	436.92	3.60	187.15	1.54
		Δv	2.81	5.40	2.72	5.28	1.85	3.55	3.21	5.99	5.32	5.83
	L_3	Δr	435.09	3.58	399.48	3.29	438.61	3.61	467.45	3.85	162.88	1.34
		Δv	12.52	7.97	4.46	4.96	4.55	8.50	9.93	6.46	4.04	4.51

Table 9. The results of the design space exploration for sail configuration 3 (one-sided, $\beta = 1779$). The errors at linkage Δr and Δv are given in AU and km/s, as well as in their error percentages. The best result is marked in orange.

			Arrival									
	Location		L_1		L_2		L_3		L_4		L_5	
			AU - km/s	%	AU - km/s	%	AU - km/s	%	AU - km/s	%	AU - km/s	%
Departure	L_1	Δr	-	-	-	-	-	-	-	-	-	-
		Δv	-	-	-	-	-	-	-	-	-	-
	L_2	Δr	293.29	2.41	456.24	3.76	469.16	3.86	438.55	3.60	325.79	2.68
		Δv	32.32	10.83	30.22	10.22	30.67	9.94	32.81	10.74	33.02	11.21
	L_3	Δr	143.70	1.18	480.75	3.96	468.66	3.85	495.05	4.08	433.27	3.57
		Δv	57.06	17.99	52.81	16.64	437.09	13.55	41.03	12.56	57.77	18.48

Table 10. The results of the design space exploration for sail configuration 4 (double-sided, β = 1779). The errors at linkage Δr and Δv are given in AU and km/s, as well as in their error percentages. The best result is marked in orange.

			Arrival									
	Location		L_1		L_2		L_3		L_4		L_5	
			AU - km/s	%	AU - km/s	%	AU - km/s	%	AU - km/s	%	AU - km/s	%
Departure	L_1	Δr	321.20	2.64	379.62	3.12	387.43	3.19	335.63	2.76	451.76	3.71
		Δv	71.29	24.87	42.02	14.65	48.78	16.53	52.06	17.54	36.87	12.93
	L_2	Δr	293.29	2.41	456.24	3.76	469.16	3.86	438.55	3.60	325.79	2.68
		Δv	32.32	10.83	30.22	10.22	30.67	9.94	32.81	10.74	33.02	11.21
	L_3	Δr	143.70	1.18	480.75	3.96	468.66	3.85	495.05	4.08	433.27	3.57
		Δv	57.06	17.99	52.81	16.64	437.09	13.55	41.03	12.56	57.77	18.48

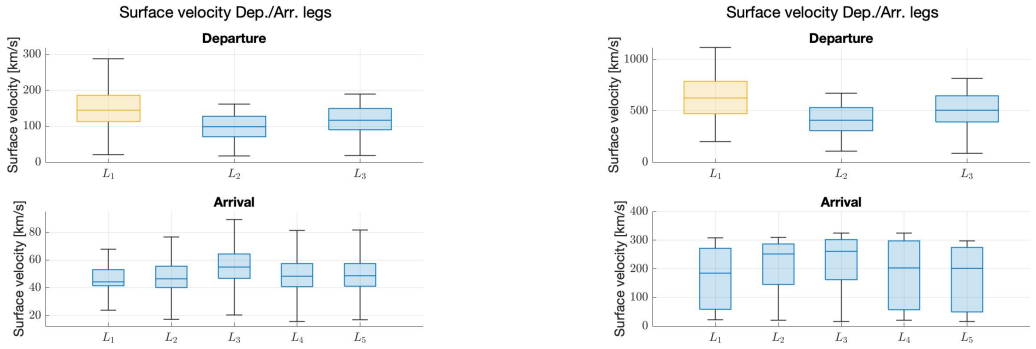

(a) **(b)**

Figure 15. Boxplots that give the average velocity at surface Q (of all trajectories that reach surface Q), for (a) sail configuration 1 (in blue) and 2 (in yellow), (b) sail configuration 3 (in blue) and 4 (in yellow).

VI. Results

The results of the optimization using the genetic algorithm are presented in this section. The Pareto fronts of the five different seeds and for both sail configurations (1 and 3) are given in Fig. 16. Both the absolute and relative errors on surface Q are given. The results show that the genetic algorithm is able to converge to solutions that minimize all three objectives effectively. Many solutions fall within a 1-5% error margin on all three objectives, and some solutions score even below 1% on all three objectives. This means that the genetic algorithm is able to find a link on surface Q between the departure and arrival phases within reasonable error margins. However, the quality of the results varies among different seeds for both sail configurations. This can be seen from the Pareto fronts, that exhibit significant differences between different seeds. For instance, in sail configuration 1, there is a substantial gap in the quality of results obtained with seed 2 and seed 4, with the genetic algorithm being unable to find the same quality of solutions using seed 4. This indicates the dependency of the genetic algorithm on the initial population, highlighting the importance of using multiple

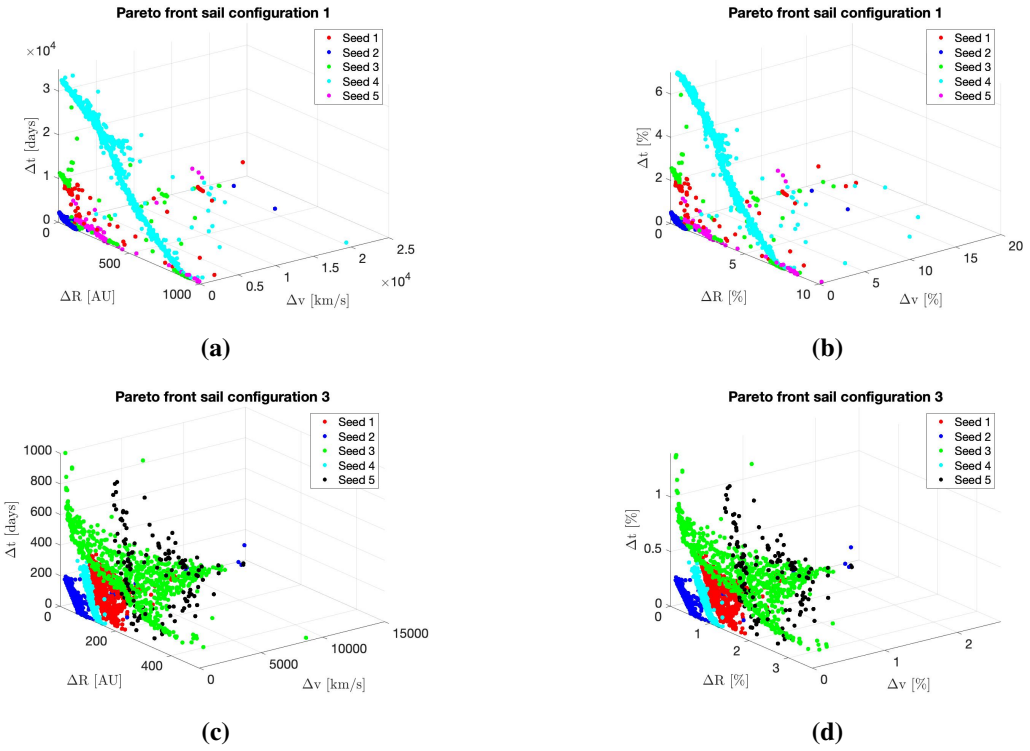

Figure 16. Results from the genetic algorithm, where the top figures represent: (a) the three objectives (link errors) for sail configuration 1, (b) the three objectives using relative errors. The bottom figures represent (c) the three objectives (link errors) for sail configuration 3, (d) the three objectives using relative errors.

seeds when applying the genetic algorithm to this optimization problem. The same trend is observed for sail configuration 3, although with smaller differences between the seeds.

Table 11. Best results from the genetic algorithm, for sail configuration 1 and 3. The results give the six decision variables for each phase, as well as the times at linkage $t_{Q,d}$ and $t_{Q,a}$, and link errors.

	$\alpha_d \mid \alpha_a$ [°]	$\delta_d \mid \delta_a$ [°]	$t_d \mid t_a$ [−]	$t_{Q,d} \mid t_{Q,a}$ [−]	Δr $[AU]$	Δv $[km/s]$	Δt $[days]$
Sail conf. 1	-56.40 | 5.11	98.65 | 106.35	2143-27-02 | 3168-02-09	2666-25-11 | 2667-03-09	70.32	0.236	281.52
Sail conf. 3	-53.66 | 30.07	99.53 | 92.93	2144-03-11 | 2379-18-03	2269-13-03 | 2268-02-10	9.13	0.761	161.08

In Fig. 17, the convergence of decision variables for the Pareto fronts presented in the previous section is shown. It is important to note that, although the phases are plotted separately, the departure and arrival phase plots are dependent on each other since a link between both phases is evaluated. For both sail configurations, the departure phase shows clear convergence to an optimal solution for each seed. It is also remarkable that the region of convergence seems to be independent of the sail configuration, although that should be further tested on more sail configurations. For both sail configurations (Fig. 17a and c), all five seeds show

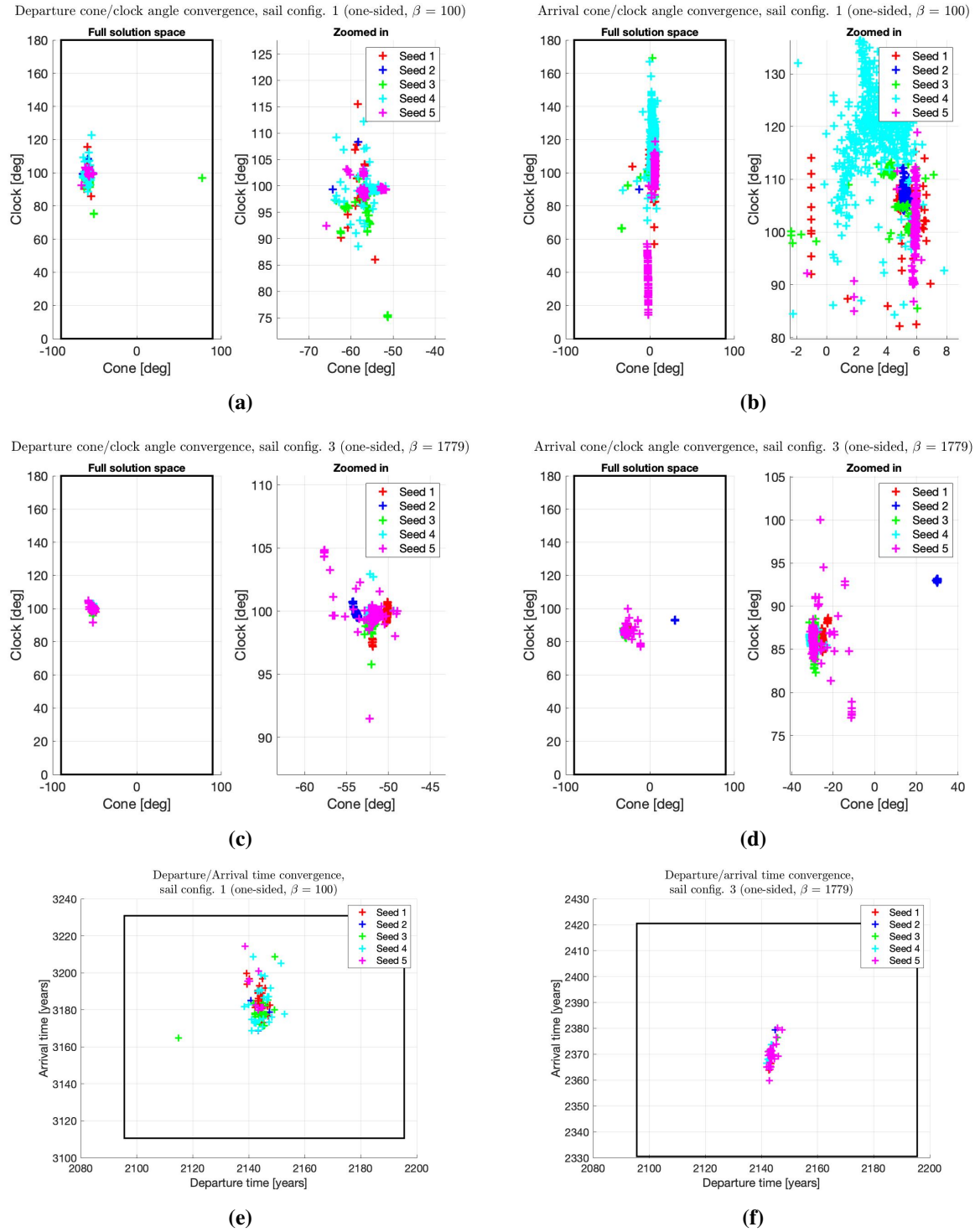

Figure 17. Decision variable values of the Pareto front solutions, for (a) sail configuration 1 departure phase, (b) sail configuration 1 arrival phase, (c) sail configuration 3 departure phase, (d) sail configuration 3 arrival phase. Plots (e and f) show the departure/arrival time convergence for sail configurations 1 and 3, respectively.

convergence to a specific area in the solution space: $-45° \leq \alpha_d \leq -65°$, and $90° \leq \delta_d \leq 110°$. Moreover, for both sail configurations, the arrival phase (Fig. 17b and d) shows a less clear area of convergence. This is especially true for sail configuration 1, where many solutions are found around a zero cone angle, meaning that the clock angle is not of much influence for those solutions. This is because a zero clock angle implies that the trajectory stays in the orbital plane of the primaries (see Eqs. 9 and 10). The fact that many solutions of the arrival phase are found around a zero-clock angle can be explained by the assumed inclination of the arrival system, which intersects with the orbital plane of the departure system close to the barycenter of the departure system. Therefore, in-plane arrival phases are more likely to allow for a transfer with the departure system. The result is that the genetic algorithm does not converge towards a narrow area in the solution space, because it finds solutions with similar quality despite the clock angle used. The results for the sail configuration 3 arrival phase show different convergence areas. There, the algorithm converges to solutions with cone angles slightly further off from zero, and therefore, the clock angle has more impact on the quality of the results and the algorithm converged again to a specific area in the solution space. From Fig. 17d, it can be observed that the algorithm converged to two different regions in the solution space. Only with seed 2 did the algorithm converge to the area with cone angles slightly larger than zero, whereas using the other seeds it converged to cone angles slightly smaller than zero. Figure 16 already showed that the Pareto front for seed 2 contains much better solutions than for the other seeds. Thus, four out of five seeds got trapped in a local minimum, and, even for seed 2, it is difficult to conclude whether it has converged to a globally optimal solution. Once again, the results indicate how sensitive the genetic algorithm is to the initial population and how susceptible the optimization problem in this work is to very small changes in the decision variables. Fig. 17e and Fig. 17f show the convergence for the departure and arrival time. For sail configuration 1, most solutions of different seeds are in good agreement, but there remains a relatively large spread in the convergence area: $2120 \leq t_d \leq 2140$, $3180 \leq t_a \leq 3210$. For sail configuration 3, the five seeds converged to the same, narrow area: $2140 \leq t_d \leq 2150$, $2360 \leq t_a \leq 2380$.

Since the multi-objective optimization results in a 3D Pareto front, no absolute best solution can be appointed. But, since the objective is to minimize all three of them, it makes sense to look for a solution in the Pareto front closest to the point (0,0,0). To achieve this, the relative error percentages are employed to calculate the absolute distance of each point in the Pareto front to the origin, thereby determining the optimal solution. Subsequently, the arrival phase is fully propagated to surface Q without a cut-off, using the initial conditions and attitude corresponding to the optimal solution. This yields the true arrival phase. The resulting trajectories are presented in the O_d-frame for both sail configurations and are given by Fig. 18 and Fig. 19. In these figures, the left plot contains the entire trajectory, and in the right plot, the states $\mathbf{x}_{d,f}$

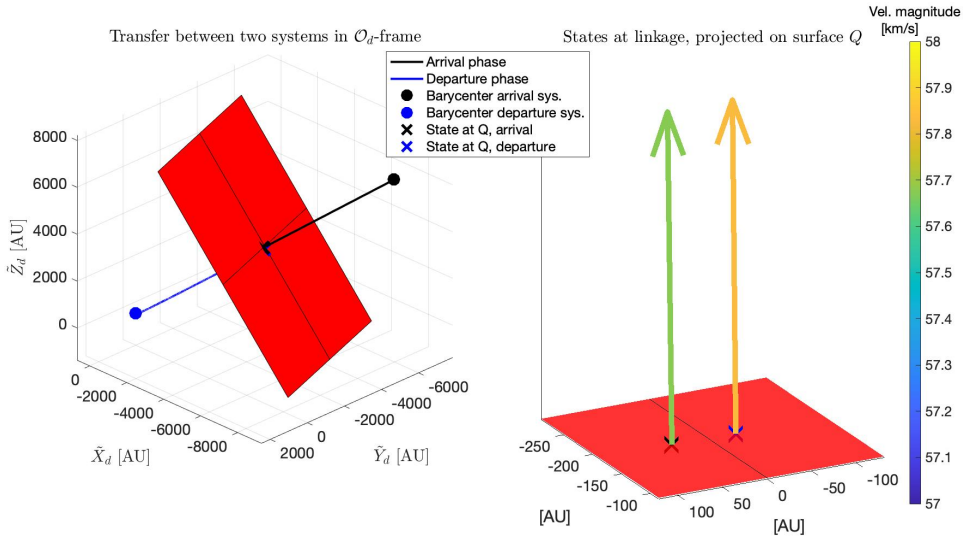

Figure 18. Best solution transfer trajectory in the $\mathcal{O}_d$-frame sail configuration 1 (left). Right plot shows states $\mathbf{x}_{Q,d}$ and $\mathbf{x}_{Q,a}$, normalized to the surface Q.

and $\mathbf{x}_{a,f}$ are projected on surface Q. The arrows represent the velocity vectors of both phases at Q, colored corresponding to their magnitude. The remaining linkage errors can therefore clearly be observed for both sail configurations. In Table 11, the decision variables, time at the linkage, and remaining state errors are all presented for the best solutions of both sail configurations.

To enhance the visual representation of the results, the departure and arrival of both phases in the $\mathcal{P}_d$ and $\mathcal{P}_a$-frames are illustrated in Fig. 20a and Fig. 20b for the propagation conducted over two periods of the corresponding system. Both sail configurations exhibit similar inwards/outwards spiraling trajectories. These similarities are expected, since the final solutions for both sail configurations are comparable in terms of the found constant sail attitude. The plots indicate that a larger lightness number results in a more significant distance traveled (in dimensionless units) during the same propagation time due to a larger sail acceleration; a straightforward and predictable result from this larger sail acceleration. Furthermore, the departure phase trajectories show a periodic decrease in x_d, y_d and z_d-directions. This can be explained by the pulsating nature of the $\mathcal{P}_d$-frame. As seen from the observer frame, the trajectory is merely a straight line. In the pulsating frame, this results in a trajectory that periodically shrinks/expands, which can clearly be seen in Fig. 20.

Compared to results in other literature [14], the transfer time of 235 years found in this research is much longer, using a similar sail configuration. In reference [14], a transfer time of 46 years from AC-A/AC-B to

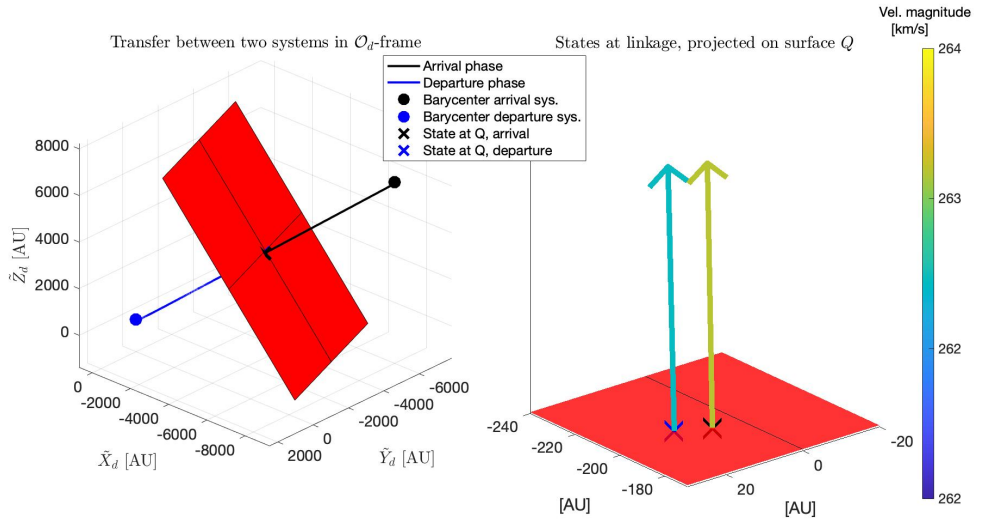

Figure 19. Best solution final trajectory in the O_d-frame sail configuration 3 (left). Right plot shows states $\mathbf{x}_{Q,d}$ and $\mathbf{x}_{Q,a}$, normalized to the surface Q.

AC-C was found. The reason for this is that, in their work, the departure towards AC-C is done with a much larger initial velocity. Their initial velocity results from an interstellar journey at percentages of the speed of light. However, for the work presented in this paper, the initial velocity depends on the rotational velocity of the Lagrange points, resulting in much longer transfer times. The found transfer time for sail configuration 3, when added to the 75-80 years travel time towards AC-A/AC-B, results in an approximate total mission time of 320 years, taking into account some time to reach the L_2-point after being captured in the departure system.

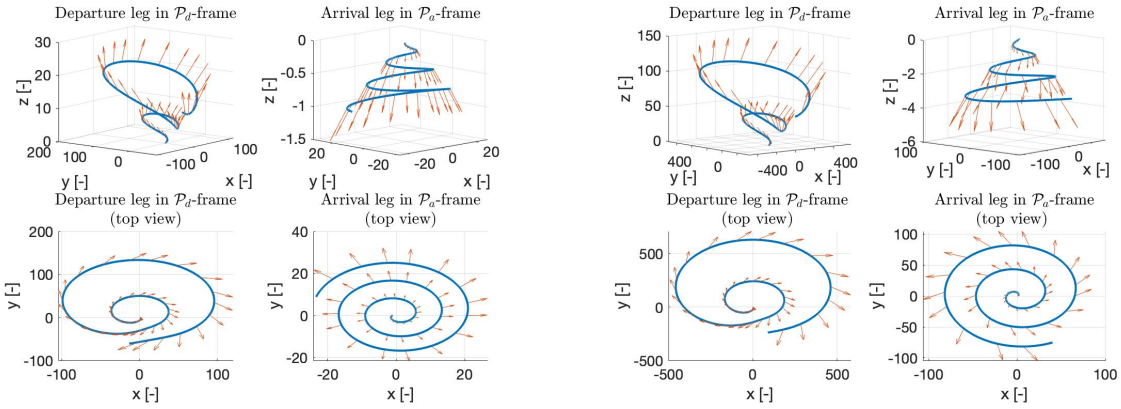

Figure 20. (a) Best solution departure/arrival phases in the $\mathcal{P}_d$-frame and $\mathcal{P}_a$-frame, for sail configuration 1. (b) Best solution departure/arrival phases in the $\mathcal{P}_d$-frame and $\mathcal{P}_a$-frame, for sail configuration 3. The bottom plots show the trajectories from a top-view. Trajectories are propagated over two periods of the respective system.

VII. Conclusion

In this paper, transfer trajectories from the L_1, L_2, and L_3-points in the Alpha Centauri A/B (AC-A/AC-B) system to all five Lagrange points Alpha Centauri C (AC-C)/Proxima b were investigated. This was done using four different futuristic sail configurations, using lightness numbers of $\beta = 100$ and $\beta = 1779$, in combination with a one-sided or a double-sided reflective sail. A transfer between the systems is sought for by exploiting photon-sail-induced invariant manifolds. The transfer is divided into two phases: departure from AC-A/AC-B and arrival at AC-C/Proxima b. The link between the phases is evaluated at a Poincaré section Q. A robust but computationally expansive grid search was applied in a design space exploration as a first analysis of the problem. The design space exploration revealed that the problem's most critical part is finding a good velocity link between the phases. Due to the greater luminosity of the stars in the AC-A/AC-B system compared to red-dwarf star AC-C, the velocity build-up during the departure phase is too great to be reduced in the arrival phase. Since the velocity build-up is smallest when starting from the L_2-point in the AC-A/AC-B system, this proved to be the best starting location. The choice of arrival location is of minor influence on the results and a double-sided sail opens up the possibility to start at the L_1-point in the departure system. However, due to the constant sail attitude and large lightness numbers, it does not improve the results for a departure from the L_2 and L_3-points. Based on these preliminary conclusions, for sail configuration 1 (one-sided reflective, $\beta = 100$), a transfer from the L_2-point in AC-A/AC-B to the L_3-point in AC-C/Proxima b was investigated using a genetic algorithm. For sail configuration 3 (one-sided reflective, $\beta = 1779$), a transfer from the L_2-point in AC-A/AC-B to the L_1-point in AC-C/Proxima b was explored. The best result

for sail configuration 1 shows remaining link errors of: Δr = 70.32 AU, Δv = 0.236 km/s, and Δt = 281.52 days, with a total transfer time of 1025 years, departing in the year 2143 and arriving in 3168. The best result for sail configuration 3 shows remaining link errors of: Δr = 9.13 AU, Δv = 0.761 km/s, and Δt = 161.08 days, with a total transfer time of 235 years, starting in the year 2144 and arriving in 2379. These errors are small considering the total distance, travel time, and velocity at surface Q. The found results could serve as an initial guess for optimal control algorithms suited for this problem. The genetic algorithm showed robust convergence with a large number of function evaluations and different seeds, although it can get trapped in local minima for the arrival phase and did not always exhibit full convergence, which may be improved with a larger population or more generations. The results from the genetic algorithm do demonstrate that it is possible to use heteroclinic connections in the Alpha Centauri system to find a transfer towards AC-C. Nevertheless, the time to reach AC-C/Proxima b for sail configuration 3, including travel time to AC-A/AC-B and time to reach L_2, is estimated to be approximately 320 years, much longer than values in previous literature [14] of 120 years, due to their much larger initial velocity resulting from an interstellar journey.

References

[1] Kameswara-Rao, N., et al., "Father J. Richaud and Early Telescope Observations in India," *Bulletin of the Astronomical Society of India*, Vol. 12, 1984, p. 81.

[2] Henderson, H., "On the Parallax of Alpha Centauri," *Memoirs of the Royal Astronomical Society*, Vol. 11, 1840, p. 61.

[3] Glass, I. S., "The Discovery of the Nearest Star," *African Sky*, Vol. 11, 2007, p. 39.

[4] Kervella, P., Thévenin, F., and Lovis, C., "Proxima's orbit around α Centauri," *Astronomy and Astrophysics*, Vol. 598, 2017. doi: 10.1051/0004-6361/201629930.

[5] Bixel, A., and Apai, D., "Probabilistic Constraints on the Mass and Composition of Proxima b," Vol. 836, No. 2, 2017, p. L31. URL https://doi.org/10.3847/2041-8213/aa5f51.

[6] Benedict, G. F., and McArthur, B. E., "A Moving Target—Revising the Mass of Proxima Centauri c," Vol. 4, No. 6, 2020, p. 86. URL https://doi.org/10.3847/2515-5172/ab9ca9.

[7] Genio, D., et al., "Habitable Climate Scenarios for Proxima Centauri b with a Dynamic Ocean," *Astrobiology*, Vol. 19, No. 1, 2019, pp. 99–125. URL https://doi.org/10.1089/ast.2017.1760.

[8] Meadows, V. S., et al., "The Habitability of Proxima Centauri b: Environmental States and Observational Discriminants," *Astrobiology*, Vol. 18, No. 2, 2018, pp. 133–189. URL https://doi.org/10.1089/ast.2016.1589.

[9] Barnes, R., et al., "The Habitability of Proxima Centauri b I: Evolutionary Scenarios," *Astronomy & Astrophysics*, Vol. 596, 2016. URL https://doi.org/10.1051/0004-6361/201629576.

[10] Mori, O., et al., "First Solar Power Sail Demonstration by IKAROS," *Transactions of the Japan Society for Aeronautical and Space Sciences, Aerospace Technology Japan*, Vol. 8, 2010. doi: 10.2322/tastj.8.to_4_25.

[11] Vulpetti, G., Johnson, L., and Matloff, G. L., *Solar sails: A novel approach to interplanetary travel*, 2015. doi: 10.1007/978-1-4939-0941-4.

[12] Wilkie, W., Fernandez, J., Stohlman, O., Schneider, N., Dean, G., Kang, J., Warren, J., Cook, S., Brown, P., Denkins, T., Horner, S., Tapio, E., Straubel, M., Richter, M., and Heiligers, J., "An Overview of the NASA Advanced Composite Solar Sail (ACS3) Technology Demonstration Project," 2021.

[13] Heller, R., and Hippke, M., "Deceleration of high-velocity interstellar photon sails into bound orbits at Alpha Centauri," *The American Astronomical Society*, Vol. 835, No. 2, 2017. URL http://dx.doi.org/10.3847/2041-8213/835/2/L32.

[14] Heller, R., Hippke, M., and Kervella, P., "Optimized Trajectories to the Nearest Stars Using Lightweight High-velocity Photon Sails," *The Astronomical Journal*, Vol. 154, No. 3, 2017, p. 115. URL http://dx.doi.org/10.3847/1538-3881/aa813f.

[15] Forgan, D. H., Heller, R., and Hippke, M., "Photogravimagnetic assists of light sails: A mixed blessing for Breakthrough Starshot?" *Monthly Notices of the Royal Astronomical Society*, Vol. 474, No. 3, 2018, pp. 3212–3220. doi: 10.1093/mnras/stx2834.

[16] Schoutetens, F., "Photon-Sail Trajectory Optimization in Alpha Centauri using Evolutionary Neurocontrol Thesis AEE888," Master's Thesis, 2019. URL http://repository.tudelft.nl/.

[17] Peng, H., et al., "Libration Transfer Design Using Patched Elliptic Three-Body Models and Graphics Processing Units," *Journal of Guidance, Control, and Dynamics*, Vol. 40, 2017, pp. 1–12. doi: 10.2514/1.G002692.

[18] Mingotti, G., Heiligers, J., and McInnes, C., "First-guess generation of solar sail interplanetary heteroclinic connections," *Advances in the Astronautical Sciences*, Vol. 153, 2015, pp. 1633–1651.

[19] Vergaaij, M., and Heiligers, J., "Time-optimal solar sail heteroclinic-like connections for an Earth-Mars cycler," *Acta Astronautica*, Vol. 152, 2018. doi: 10.1016/j.actaastro.2018.08.008.

[20] Heiligers, J., Mingotti, G., and McInnes, C. R., "Optimal solar sail transfers between Halo orbits of different Sun-planet systems," *Advances in Space Research*, Vol. 55, No. 5, 2015, pp. 1405–1421. doi: 10.1016/j.asr.2014.11.033.

[21] Kervella, P., et al., "A Family Portrait of the Alpha Centauri System," , 2003. URL https://www.eso.org/public/news/eso0307/#1.

[22] Kamper, K. W., and Wesselink, A., "Alpha and Proxima Centauri," *The Astronomical Journal*, Vol. 83, No. 12, 1978, pp. 1653–1659.

[23] Kervella, P., et al., "Close stellar conjunctions of tauri A and B until 2050 - An mK = 7.8 star may enter the Einstein ring of en A in 2028," *Astrodynamics & Astrophysics*, Vol. 594, 2016, p. A107. URL https://doi.org/10.1051/0004-6361/201629201.

[24] Akeson, R., et al., "Precision Millimeter Astrometry of the Centauri AB System," *The Astronomical Journal*, Vol. 162, 2021. URL https://doi.org/10.3847/1538-3881/abfaff.

[25] Thévenin, F., et al., "Asteroseismology and calibration of Alpha Cen binary system," *Astronomy and Astrophysics*, Vol. 392, 2002. doi: 10.1051/0004-6361:20021074.

[26] Sackmann, I. J., Boothroyd, A. I., and Kraemer, K. E., "Our Sun. III. Present and Future," *The Astrophysical Journal*, Vol. 418, 1993, pp. 457–468.

[27] Suarez Mascareno, A., et al., "Revisiting Proxima with ESPRESSO," *Astronomy Astrophysics*, Vol. 639, 2020. URL https://doi.org/10.1051/0004-6361/202037745.

[28] Benedict, G. F., and McArthur, B. E., "A Preliminary Mass for Proxima Centauri C," Vol. 4, No. 4, 2020, p. 46. URL https://doi.org/10.3847/2515-5172/ab84f3.

[29] Anglada-Escudé, G., et al., "A terrestrial planet candidate in a temperate orbit around Proxima Centauri," *Nature*, Vol. 536, No. 7617, 2016, p. 437–440. doi: 10.1038/nature19106.

[30] Kane, S. R., Gelino, D. M., and Turnbull, M. C., "On the orbital inclination of Proxima Centauri b," Vol. 153, No. 2, 2017, p. 52. URL https://doi.org/10.3847/1538-3881/153/2/52.

[31] Gilbert, E., et al., "No Transits of Proxima Centauri Planets in High-Cadence TESS Data," *Frontiers in Astronomy and Space Sciences*, Vol. 8, 2021. doi: 10.3389/fspas.2021.769371.

[32] Kervella, P., Arenou, F., and Schneider, J., "Orbital inclination and mass of the exoplanet candidate Proxima c," *Astronomy & Astrophysics*, Vol. 635, 2020. URL https://doi.org/10.1051/0004-6361/202037551.

[33] Szebehely, V., *Theory of orbits*, 1st ed., 1967.

[34] Heiligers, J., Schoutetens, F., and Dachwald, B., "Photon-Sail Equilibria in the Alpha Centauri System," *Journal of Guidance, Control, and Dynamics*, Vol. 44, No. 5, 2021, pp. 1053–1061. doi: 10.2514/1.g005446.

[35] Carroll, D. A., Bradley W. Ostlie, *An introduction to modern Astrophysics*, 2nd ed., 2017.

[36] Kaplan, G. H., "The IAU Resolutions on Astronomical Reference Systems, Time Scales, and Earth Rotation Models," 2006. URL https://arxiv.org/abs/astro-ph/0602086.

[37] Arias, E. F., Charlot, P., Feissel, M., and Lestrade, J. F., "The extragalactic reference system of the International Earth Rotation Service, ICRS." , Vol. 303, 1995, pp. 604–608.

[38] Baoyin, H., and McInnes, C. R., "Solar sail equilibria in the elliptical restricted three-body problem," *Journal of Guidance, Control, and Dynamics*, Vol. 29, No. 3, 2006, pp. 538–543. doi: 10.2514/1.15596.

[39] McInnes, C. R., *Solar Sailing: Technology, Dynamics, and Mission Applications*, 2nd ed., 1999. doi: 10.1007/978-1-4471-3992-8.

[40] McInnes, C. R., *Solar Sailing: Technology, Dynamics, and Mission Applications*, 2nd ed., Springer, 1999.

[41] Mingotti, G., Topputo, F., and Bernelli-Zazzera, F., "Earth-Mars transfers with ballistic escape and low-thrust capture," *Celestial Mechanics and Dynamical Astronomy*, Vol. 110, No. 2, 2011, pp. 169–188. doi: 10.1007/s10569-011-9343-5.

[42] Dachwald, B., "Optimal Solar-Sail Trajectories for Missions to the Outer Solar System," *Journal of Guidance, Control, and Dynamics*, Vol. 28, No. 6, 2005, pp. 1053–1061. doi: 10.2514/1.13301.

[43] "Gaia Data Processing and Analysis Consortium (DPAC), Gaia Data Release 2," https://gea.esac.esa.int/archive/documentation/GDR2/, 2019. [Online; accessed 5-Jan-2023].

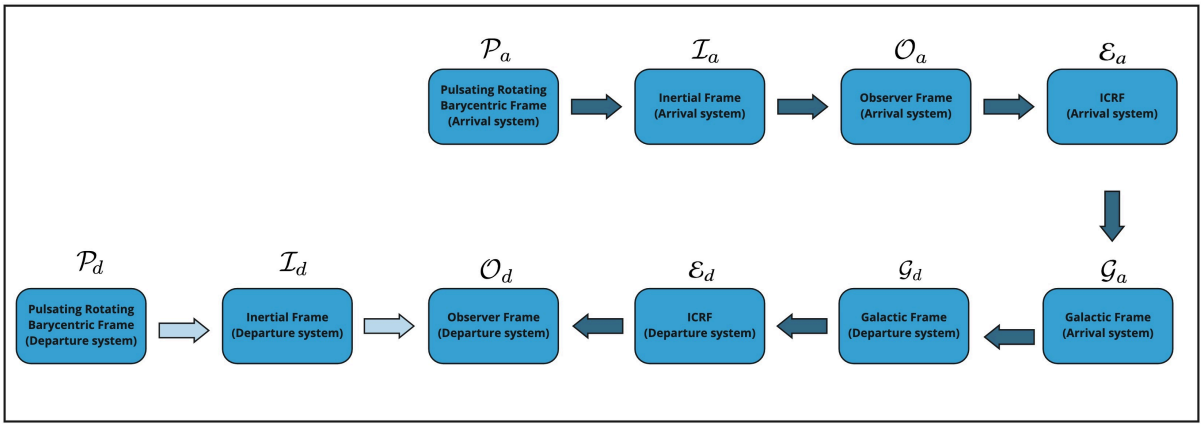

Figure 21. Sequence of frame transfromation to convert a state from $\mathcal{P}_a$ and $\mathcal{P}_d$-frames to $\mathcal{O}_d$.

Appendix

In the appendices, all frame transformations used for this research are given. The sequences to transform a state vector from the $\mathcal{P}_a$ or $\mathcal{P}_d$-frame to the $\mathcal{O}_d$-frame is given in Fig. 21. The corresponding frame transformations are provided in Appendices A-I. A general transformation, used to convert the sail normal vector $\mathbf{n}_i$ from its local sail-centered frame $\mathcal{S}_i$ to a $\mathcal{P}_i$-frame, is given in Appendix J. In addition, the general rotation matrices, denoted by $\boldsymbol{T}$, are given by Eqs. 24-26. These can be applied to rotate a frame around one of its axes, where a positive angle ϕ generates a counterclockwise rotation. The matrices will be used without further explanation in the rest of this section:

$$\boldsymbol{T}_x(\phi) = \begin{bmatrix} 1 & 0 & 0 \\ 0 & \cos\phi & \sin\phi \\ 0 & -\sin\phi & \cos\phi \end{bmatrix} \tag{24}$$

$$\boldsymbol{T}_y(\phi) = \begin{bmatrix} \cos\phi & 0 & -\sin\phi \\ 0 & 1 & 0 \\ \sin\phi & 0 & \cos\phi \end{bmatrix} \tag{25}$$

$$\boldsymbol{T}_z(\phi) = \begin{bmatrix} \cos\phi & \sin\phi & 0 \\ -\sin\phi & \cos\phi & 0 \\ 0 & 0 & 1 \end{bmatrix} \tag{26}$$

A. Arrival rotating pulsating barycentric frame $\mathcal{P}_a \longrightarrow$ Arrival inertial frame $\mathcal{I}_a$

To convert a state vector from the pulsating $\mathcal{P}_a$-frame to the inertial $\mathcal{I}_a$-frame, an approach is used described in [17]. As was stated in the main body of this paper, the subscripts d and a are used to denote the departure and arrival system. The mathematics describing this transformation are given as follows:

$$\mathbf{x}|_{\mathcal{I}_a} = \begin{bmatrix} \boldsymbol{T}_{z_a}^{-1}(\theta_a) \cdot \rho_a(\theta_a) & 0_3 \\ \frac{\mathrm{d}\left[\boldsymbol{T}_{z_a}^{-1}(\theta_a) \cdot \rho_a(\theta_a)\right]}{\mathrm{d}\theta_a} \cdot \frac{\mathrm{d}\theta_a}{\mathrm{d}t_a} & \boldsymbol{T}_{z_a}^{-1}(\theta_a) \cdot \rho_a(\theta_a) \cdot \frac{\mathrm{d}\theta_a}{\mathrm{d}t_a} \end{bmatrix} \cdot \mathbf{x}|_{\mathcal{P}_a} \tag{27}$$

The instantaneous distance between the two primaries ρ_a is a function of the true anomaly θ_a and is given as:

$$\rho_a(\theta_a) = \frac{s_a\left(1 - e_a^2\right)}{1 + e_a \cos\theta_a} \tag{28}$$

The angular velocity of the frame $\frac{d\theta_a}{dt_a}$ is given by:

$$\frac{d\theta_a}{dt_a} = \frac{G^{\frac{1}{2}}\left(m_{a,1} + m_{a,2}\right)^{1/2}}{s_a^{3/2}\left(1 - e_a^2\right)^{3/2}}(1 + e_a \cos\theta_a)^2 \tag{29}$$

B. Arrival inertial frame $\mathcal{I}_a \longrightarrow$ Arrival observer frame $\mathcal{O}_a$

This appendix describes how to transform the state from the $\mathcal{I}_a$-frame to the $\mathcal{O}_a$-frame. An approach given by [16] is used for this transformation. The full transformation consists of three rotations:

$$\mathbf{x}|_{\mathcal{O}_a} = \begin{bmatrix} \boldsymbol{T}_{Z_a}(\Omega_a)\boldsymbol{T}_{X_a}(-i_a)\boldsymbol{T}_{Z_a}(\Psi_a) & 0_3 \\ 0_3 & \boldsymbol{T}_{Z_a}(\Omega_a)\boldsymbol{T}_{X_a}(-i_a)\boldsymbol{T}_{Z_a}(\Psi_a) \end{bmatrix} \cdot \mathbf{x}|_{\mathcal{I}_a} \tag{30}$$

where the argument of periapsis Ψ_a, inclination i_a and right ascension of the ascending node Ω_a were provided in Section II.

C. Arrival observer frame $\mathcal{O}_a \longrightarrow$ Arrival ICRS frame $\mathcal{E}_a$

The steps provided in this appendix are used to transform the state from the $\mathcal{O}_a$-frame to the $\mathcal{E}_a$-frame. The transformation consists of two rotations and a translation. The translation shifts the center of the $\mathcal{O}_a$-frame to the center of AC-C. After this translation, two rotations are necessary to align the axes with the axes of the ICRS $\mathcal{E}$. The translation is given as follows:

$$\mathbf{x}|_{\mathcal{O}_{a_C}} = \mathbf{x}|_{\mathcal{O}_a} + [\rho_a\mu_a \;\; 0 \;\; 0 \;\; 0 \;\; 0 \;\; 0] \tag{31}$$

Note that the distance μ_a between the barycenter and AC-C is multiplied with the instantaneous separation between the two primaries ρ_a to dimensionalize the distance. The next step is to align the frame with the $\mathcal{E}$-frame. This is done by the following two rotations:

$$\mathbf{x}|_{\mathcal{E}_a} = \begin{bmatrix} \boldsymbol{T}_{\tilde{Z}_a}(-RA_C)\boldsymbol{T}_{\tilde{Y}_a}(DEC_C + 90°) & 0_3 \\ 0_3 & \boldsymbol{T}_{\tilde{Z}_a}(-RA_C)\boldsymbol{T}_{\tilde{Y}_a}(DEC_C + 90°) \end{bmatrix} \cdot \mathbf{x}|_{O_{a_C}} \tag{32}$$

where the right ascension and declination of AC-C, RA_C and DEC_C, were provide in Section II.

D. Arrival ICRS frame $\mathcal{E}_a \longrightarrow$ Arrival galactic $\mathcal{G}_a$

The conversion from a state vector in $\mathcal{E}_a$ to $\mathcal{G}_a$ is described in the Gaia data release [43]:

$$\mathbf{x}|_{\mathcal{G}_a} = \begin{bmatrix} \boldsymbol{D}_G^{-1} & 0_3 \\ 0_3 & \boldsymbol{D}_G^{-1} \end{bmatrix} \cdot \mathbf{x}|_{\mathcal{E}_a} \tag{33}$$

$$\begin{aligned} \boldsymbol{D}_G^{-1} &= \boldsymbol{R}_z\left(-l_\Omega\right)\boldsymbol{R}_x\left(90° - DEC_G\right)\boldsymbol{R}_z\left(_G + 90°\right) \\ &= \begin{bmatrix} -0.0548755604162154 & -0.8734370902348850 & -0.4838350155487132 \\ +0.4941094278755837 & -0.4448296299600112 & +0.7469822444972189 \\ -0.8676661490190047 & -0.1980763734312015 & +0.4559837761750669 \end{bmatrix} \end{aligned} \tag{34}$$

where the galactic longitude of the first intersection of the galactic plane with the equator is $l_\Omega = 32.93192°$, the right ascension of the north galactic pole $RA_G = 192.85948°$, and the declination of the north galactic pole $DEC_G = 27.12825°$.

E. Arrival galactic frame $\mathcal{G}_a \longrightarrow$ Departure galactic frame $\mathcal{G}_d$

The conversion of a state vector from the $\mathcal{G}_a$-frame to the $\mathcal{G}_d$-frame only consists of a translation; the translation from AC-C to the barycenter of the AC-A/AC-B system:

$$\mathbf{x}|_{\mathcal{G}_d} = \mathbf{x}|_{\mathcal{G}_a} + \mathbf{x}_C|_{\mathcal{G}_d} \tag{35}$$

Where $\mathbf{x}_C|_{\mathcal{G}_d}$ is the state vector of AC-C with respect to the barycenter of the system.

F. Departure galactic frame $\mathcal{G}_d \longrightarrow$ Departure ICRS frame $\mathcal{E}_d$

The conversion from a state vector in $\mathcal{G}_d$ to $\mathcal{E}_d$ is the reverse from the transformation described in Section Appendix D.

$$\mathbf{x}|_{\mathcal{E}_d} = \begin{bmatrix} \boldsymbol{D}_G & 0_3 \\ 0_3 & \boldsymbol{D}_G \end{bmatrix} \cdot \mathbf{x}|_{\mathcal{G}_d} \tag{36}$$

where $\boldsymbol{D}_G$, l_Ω, RA_G, and DEC_G are provided in Appendix D.

G. Departure ICRS frame $\mathcal{E}_d \longrightarrow$ Departure observer frame O_d

The transformation to transform the state from the $\mathcal{E}_d$-frame to the O_d-frame consists of two rotations. Since both frames have their origin in the barycenter, there is no need for an additional translation:

$$\mathbf{x}|_{O_d} = \begin{bmatrix} \boldsymbol{T}_{j_{2,d}}(-(DEC_{AB}+90)^\circ)\boldsymbol{T}_{j_{3,d}}(RA_{AB}) & 0_3 \\ 0_3 & \boldsymbol{T}_{j_{2,d}}(-(DEC_{AB}+90)^\circ)\boldsymbol{T}_{j_{3,d}}(RA_{AB}) \end{bmatrix} \cdot \mathbf{x}|_{\mathcal{E}_d} \tag{37}$$

where RA_{AB} and DEC_{AB} are the right ascension and declination of the barycenter of AC-A/AC-B.

H. Departure rotating pulsating barycentric frame $\mathcal{P}_d \longrightarrow$ Departure inertial frame $\mathcal{I}_d$

This appendix provides the transformation from the $\mathcal{P}_d$-frame to the O_d-frame. The first part of this process is to go from the $\mathcal{P}_d$-frame to the $\mathcal{I}_d$-frame.

$$\mathbf{x}|_{\mathcal{I}_d} = \begin{bmatrix} \boldsymbol{T}_{z_d}^{-1}(\theta_d) \cdot \rho_d(\theta_d) & 0_3 \\ \frac{\mathrm{d}\left[\boldsymbol{T}_{z_d}^{-1}(\theta_d)\cdot\rho_d(\theta_d)\right]}{\mathrm{d}\theta_d} \cdot \frac{\mathrm{d}\theta_d}{\mathrm{d}t_d} & \boldsymbol{T}_{z_d}^{-1}(\theta_d) \cdot \rho_d(\theta_d) \cdot \frac{\mathrm{d}\theta_d}{\mathrm{d}t_d} \end{bmatrix} \cdot \mathbf{x}|_{\mathcal{P}_d} \tag{38}$$

The instantaneous distance between the two primaries is a function of the true anomaly θ_d and is given as:

$$\rho_d(\theta_d) = \frac{s_d\left(1-e_d^2\right)}{1+e_d\cos\theta_d} \tag{39}$$

The angular velocity of the frame $\frac{d\theta_d}{dt_d}$ is given by:

$$\frac{d\theta_d}{dt_d} = \frac{G^{\frac{1}{2}}\left(m_{d,1}+m_{d,2}\right)^{1/2}}{a_d^{3/2}\left(1-e_d^2\right)^{3/2}}(1+e_d\cos\theta_d)^2 \tag{40}$$

I. Departure inertial frame $\mathcal{I}_d \longrightarrow$ Departure observer frame O_d

To transform a state vector from the $\mathcal{I}_d$-frame to the O_d-frame, the following three rotations are applied:

$$\mathbf{x}|_{O_d} = \begin{bmatrix} \boldsymbol{T}_{Z_d}(\Omega_d)\boldsymbol{T}_{X_d}(-i_d)\boldsymbol{T}_{Z_d}(\Psi_d) & 0 \\ 0 & \boldsymbol{T}_{Z_d}(\Omega_d)\boldsymbol{T}_{X_d}(-i_d)\boldsymbol{T}_{Z_d}(\Psi_d) \end{bmatrix} \cdot \mathbf{x}|_{\mathcal{I}_d} \tag{41}$$

where the argument of periapsis Ψ_d, inclination i_d and right ascension of the ascending node Ω_d of AC-A and AC-B are given in Section II.

J. General: $\mathcal{S}_i \rightarrow \mathcal{P}_i$

In this appendix, the general frame transformation from a sail-centered frame $\mathcal{S}_i$ to the rotating pulsating barycentric frame $\mathcal{P}_i$ is given. This transformation can be applied to either the departure or the arrival system by substituting the subscript i (where $i = a, d$). The conversion of a vector $\hat{\mathbf{n}}_i$ in the $\mathcal{S}_i$-frame to the $\mathcal{P}_i$-frame is done by multiplying the vector in the $\mathcal{S}_i$-frame by the unit vectors of this frame given in the $\mathcal{P}_i$-frame:

$$\hat{\mathbf{n}}|_{\mathcal{P}_i} = \hat{\mathbf{n}} = \begin{bmatrix} \hat{\mathbf{r}}_i & \hat{\boldsymbol{\theta}}_i & \hat{\boldsymbol{\eta}}_i \end{bmatrix} \hat{\mathbf{n}}\Big|_{\mathcal{S}_i} \tag{42}$$

This then becomes:

$$\hat{\mathbf{n}}|_{\mathcal{P}_i} = \begin{bmatrix} \frac{x_i-\mu_i}{r_i}\cos\alpha_i - \frac{(x_i-\mu_i)x_i}{r_i r_i^*}\sin\alpha_i\cos\delta_i - \frac{y_i}{r_i^*}\sin\alpha_i\sin\delta_i \\ \frac{y_i}{r_i}\cos\alpha_i - \frac{y_i x_i}{r_i r_i^*}\sin\alpha_i\cos\delta_i + \frac{x_i-\mu_i}{r_i^*}\sin\alpha_i\sin\delta_i \\ \frac{x_i}{r_i}\cos\alpha_i + \frac{r_i^*}{r_i}\sin\alpha_i\cos\delta_i \end{bmatrix} \tag{43}$$

Where $r_i^* = \sqrt{(x_i+\mu_i)^2 + y_i^2}$, and α_i/δ_i are the cone/clock angle.

3

Conclusions and Recommendations

In this thesis work, heteroclinic connections were employed to find photon-sail transfers between the Alpha Centauri A/Alpha Centauri B (AC-A/AC-B) and Alpha Centauri C (AC-C)/Proxima b systems. As an extension to previous studies, which focused on capturing orbits around AC-A or AC-B or transferring to AC-C after a flyby of AC-A/AC-B, this work aimed to find a trajectory towards AC-C for conducting in-situ measurements of Proxima b. This was achieved by patching together two elliptic restricted three-body problems, each augmented with a photon sail, and using two optimization methods, a grid search and a genetic algorithm, to establish a connection between the two patched models. The colinear Lagrange points in the AC-A/AC-B system were investigated as departure locations. In the AC-C/Proxima b system, all five Lagrange points were considered. This chapter presents the findings of the study, answering the research questions, and provides suggestions for future work in the second section.

3.1. Conclusions

The conclusions are divided into two parts, each containing one of the main research questions, where each research question has several sub-questions.

1. **Can a transfer be found between equilibrium points of the AC-A/AC-B and AC-C/Proxima b systems using photon-sail augmented heteroclinic connections?** The answer to this question depends on the answers to the sub-questions. Therefore, the sub-questions are answered first.

   (a) **What are the minimum errors at linkage in terms of position, velocity, and time between the trajectories from both systems**

   In this work, two optimization methods were applied to find an optimal link between the two patched elliptic restricted three-body problems. A grid search was used to limit the design space for the genetic algorithm, resulting in the elimination of two of the four sail configurations. The sail configurations employed by the genetic algorithm were one-sided ideal sails with lightness numbers $\beta = 100$ and $\beta = 1779$, referred to as sail configuration 1 and 3, respectively. The link is evaluated on the Poincaré surface Q, a surface in phase space perpendicular to the imaginary line connecting the barycenters of the two systems and located halfway between them. In the departure phase, starting from the AC-A/AC-B system, the state is propagated forward until section Q. In the arrival phase, ending in the AC-C/Proxima b system, the state is propagated backward in time. The optimization aimed to minimize the position, velocity, and time errors between the departure and arrival phases at surface Q. The final results were presented as three-dimensional Pareto fronts in absolute units (AU, km$/$s, and days) and relative error percentages. For the position error, the relative error is the absolute error divided by the distance between the barycenters of the two systems. For the velocity, the relative error is the absolute error divided by the velocity magnitude of the corresponding trajectory at surface Q. For the time, the relative error is the absolute error divided by the total travel time of the transfer. A solution from the Pareto front

closest to (0,0,0) was selected for each sail configuration and listed in Table 3.1. In addition, many solutions in the Pareto fronts of sail configuration 1 and 3 have relative errors smaller than 1% for all three objectives.

Table 3.1: Best results from the genetic algorithm, for sail configuration 1 and 3. The results give the six decision variables for each phase, as well as the times at linkage $t_{Q,d}$ and $t_{Q,a}$, and link errors.

	δ_d | δ_a [°]	α_d | α_a [°]	transfer time $[years]$	Δr $[AU - \%]$	Δv $[km/s - \%]$	Δt $[days - \%]$
Sail conf. 1	-56.40 | 5.11	98.65 | 106.35	1025	70.32 [0.58%]	0.236 [0.16%]	281.52 [0.064%]
Sail conf. 3	-53.66 | 30.07	99.53 | 92.93	235	9.13 [0.075%]	0.761 [0.13%]	161.08 [0.037%]

(b) **What is the minimum time for such a transfer?** The minimum time found by the genetic algorithm was 1025 years for sail configuration 1, and 235 years for sail configuration 3. A direct comparison can be made with the work of Heller & Hippke [20] who calculated a transfer time of 46 years to AC-C (starting from AC-A/AC-B) using a photon sail similar to sail configuration 3. However, the initial velocity used in their transfer was much higher due to a flyby of the AC-A/AC-B system at a high fraction of the speed of light. Given that the initial and final velocity in this work are mainly coming from the orbital rotation of the primary masses (about their barycenters), a transfer time five times greater than that of Heller & Hippke can still be considered a good outcome.

(c) **How do different combinations of departure and arrival locations perform in terms of transfer time and linkage errors?** The results of the design space exploration showed that the departure point has a substantial effect on the outcome. Furthermore, it was found that the velocity error at linkage is the most challenging factor to overcome. Due to the nature of the departure system, with two stars with comparable luminosity to the Sun, the relative lightness number is much higher than in the arrival system. In contrast, since AC-C is a red-dwarf star with a small luminosity, this considerably reduces the usability and flexibility of a photon sail in the arrival system compared to the departure system or the Solar system. As a result, the best departure point was determined to be the L_2-point, which minimizes the velocity build-up and results in better velocity links with the arrival phase at the Poincaré section. The specific arrival location (in the AC-C/Proxima b system) was found to have a limited impact on the results, due to the one-star nature of the system and the relatively small distances between its Lagrange points compared to the total travel distance. Although the arrival location may affect the trajectory in the arrival pulsating rotating barycentric frame $\mathcal{P}_a$,[1] it will have a minor impact on the overall transfer trajectory in the departure observer frame $\mathcal{O}_d$.[2]

(d) **How do different sail configurations impact the results in terms of transfer time and linkage errors?** The results in Table 3.1 indicate that sail configuration 3 exhibits a significant reduction in transfer time, while maintaining comparable absolute errors compared to configuration 1. But, it is noteworthy that the relative errors for sail configuration 3 are smaller, a result that can not easily be explained. Combining this with the fact that the different seeds of the genetic algorithm did not fully converge to a similar quality of results, there is a possibility that the algorithm did not converge to a global optimum for sail configuration 1. Another possibility is that the global optimal solution for sail configuration 1 consists of larger relative errors, or, that there is another underlying reason for these larger relative errors, but this can only be confirmed by further research on the problem. The design space exploration revealed that a double-sided sail does not significantly improve the results, due to the constant sail attitude during both phases, meaning that a one-sided or double-sided

[1] The origin of the $\mathcal{P}_a(\mathbf{x}_a,\mathbf{y}_a,\mathbf{z}_a)$-frame is located in the barycenter of AC-C and Proxima b. Its x_a-axis is aligned with the line connecting the two primaries, positive in the direction of Proxima b. The z_a-axis is aligned with the angular velocity vector $\boldsymbol{\omega}_a$, perpendicular to the $x_a y_a$-plane. The y_a-axis completes the right-handed reference frame.

[2] The $\mathcal{O}_d(\tilde{\mathbf{X}}_d, \tilde{\mathbf{Y}}_d, \tilde{\mathbf{Z}}_d)$-frame is located in the barycenter of AC-A and AC-B, the $\tilde{Z}_d$-axis points towards the observer and the $\tilde{X}_d$ and $\tilde{Y}_d$-axes are defined in the plane-of-the-sky (tangential plane), a plane perpendicular to $\tilde{Z}_d$. The $\tilde{X}_d$-axis points away from the intersection between the tangential plane and an imaginary line through the Celestial South Pole. The $\tilde{Y}_d$-axis completes the right-handed frame.

sail yields similar results in most cases. However, it provides the possibility of departing from the departure system's L_1-point. When considering the possibility of changing the sail attitude along the trajectory, the use of a double-sided sail could result in a more substantial impact on the outcomes.

Based on the answers to the sub-questions above, it can be concluded that good links between the departure and arrival system can be found by using photon-sail augmented heteroclinic connections. The results showed that the relative errors in position, velocity, and time were kept within their 1% error ranges, which is considered a reasonable error margin for a proper link.

2. **Can a grid search be used to reduce the design space for the genetic algorithm?** The grid search proved to be effective in reducing the design space of the genetic algorithm. Using the results from the grid search, it was possible to draw conclusions on the suitability of the different departure and arrival locations, as well as on the sail configuration. The grid search revealed that especially the departure location was important when constructing a transfer, and that the L_1-point is the best suited departure location. It also showed that the arrival location was of less influence, but the grid search still provided valuable information to choose a specific location. The grid search also gave insight into expected nominal transfer times, which helped in defining the bounds on the departure and arrival times for the genetic algorithm. Furthermore, results showed that double-sided reflective sails (configurations 2 and 4) offered no improvements compared to the one-sided configurations (1 and 3). The departure/arrival location and sail configuration choices reduced the design space significantly, but the grid search proved to be less useful in narrowing the bounds for cone and clock angles. This is mainly because the attitude needed to create a proper transfer is also dependent on the departure/arrival time. More specifically, whether the sail is headed in the correct direction to allow for a transfer, is not only dependent on the attitude, but also on the true anomaly of the respective system upon departure/arrival. A specific attitude can lead to a good transfer or not, depending on the true anomaly at departure/arrival. Since the true anomaly is *also* a decision variable, it is difficult to narrow down the bounds on the cone and clock angles, so the bounds on these variables were imposed by the constraints defined in the methodology.
3. **Is a genetic algorithm a suitable tool to solve the optimization problem in terms of global convergence?**

   This research showed that the genetic algorithm can be a valuable tool in solving the optimization problem, being able to compute transfers with reasonable link errors. However, the outcome of the genetic algorithm still leaves minor errors, which could be overcome when the results are used as input for an optimal control solver. The advantage of the genetic algorithm is clearly its simplicity of implementation, in combination with the fact that no apriori knowledge of the problem is necessary. A disadvantage is that the algorithm does not provide much insight in the problem. This disadvantage is what is often referred to as a "black box". Therefore, using only a genetic algorithm to solve similar problems remains tricky. A good, safe strategy is thus to combine it with another optimization technique, such as a grid search.

   From literature, it is known that a genetic algorithm *is* able to converge to global minima, under certain circumstances. The results from this research cannot definitively confirm if the genetic algorithm found the global optimal solution, as the global optimum is unknown. In theory, the global optimum of this optimization problem could be the point (0,0,0) in solution space. One of the goals of this research was to investigate the feasibility of a transfer, so whether such a perfectly smooth link (with zero position, velocity and time errors between the phases) truly exists is unknown. It is possible that the results presented in this work are already close to the global optimal solution, or even contain this solution. But, the genetic algorithm improved its solutions during the final iterations for all seeds and both sail configurations, implying that the global optimum may not have been found. Furthermore, during the arrival phase, for sail configuration 1, a wide spread of decision variable convergence is observed, although this does not necessarily mean the genetic algorithm has not properly converged. During the arrival phase, most solutions in the Pareto front have cone angles around zero degree. This is due to the inclined orbit of Proxima b, relative to the plane perpendicular to the line of sight (for an observer located in the Solar system). Due to this inclination, arrival trajectories that stay close to or in the orbital plane result in the best

link. Since the cone angle for the optimal solution is close to zero, the clock angle does not have much influence on the sail acceleration. Hence, the algorithm finds equally good solutions with a wide spread on the clock angle. Furthermore, four out of the five seeds show a similar quality of results in the Pareto front, suggesting that the global optimal solution could be present in the solution space to which these seeds have converged. For sail configuration 3 (during arrival phase), the results show that seed 2 gave much better solutions than the other seeds and converged to a different cone/clock angle range. This indicates that, the algorithm got trapped in a local optimum with the other four seeds. So, especially the results for the arrival phase suggest that the genetic algorithm is not always able to converge to a global minimum with the settings used in this work. However, during departure phase, for both sail configurations, the algorithm converged to narrow cone, clock, and departure time ranges, suggesting that the decision variable convergence in that phase is independent of the seed. To conclude, the results show how sensitive the optimization problem is to small changes in the decision variables. However, the results do suggest that the algorithm can converge to a global solution with a large enough population size and number of generations. Choosing a larger population size will produce a denser initial population, increasing the chance of finding the globally optimal solution, especially in combination with a larger number of generations, so that it can be ensured that the algorithm fully converges.

3.2. Recommendations

Now that the conclusions of this thesis work are given, the recommendations for future research are presented here. The recommendations are meant to either provide possible extensions of the work presented on heteroclinic connections in Alpha Centauri, or to improve this thesis research. Because of this thesis's futuristic nature, some remarks can be made on the applicability of this research, especially regarding the currently available data on the bodies in the Alpha Centauri system.

Optimal control solver

The first recommendation is to use the results from this research as an initial guess as input for an optimal control solver suited for this problem, such as the open-source PSOPT algorithm. This algorithm already proved to be suited for similar research on photon-sail heteroclinic connections [27, 28]. The optimization algorithm can then use the initial guess to close the gap between departure and arrival phases on the Poincaré section and ensure a smooth linkage. In addition, such an optimizer can improve the sudden attitude change at linkage, which was for simplicity accepted in this research, with a smoother change of attitude by, for example, introducing a transition phase between the departure and arrival phases. Furthermore, in this thesis, the three main objectives were the position, velocity, and time errors at link surface Q. An optimal control solver could also be used to minimize the transfer time while keeping the linkage errors minimal. Doing this with the genetic algorithm implementation in Matlab (*gamultiobj.m*), by adding a fourth objective that minimizes the time along with the linkage errors, could potentially lead to a large amount of function evaluations. An optimal control solver might be able to do this more efficiently, especially when using the results of this work as initial guess. An interesting feature to add when using an optimal control solving algorithm is allowing the sail to change attitude along the trajectory, which could lead to improvement of the results. Especially for the parts of the trajectories close to the stars, allowing the sail to change attitude could result in much different trajectories.

Dynamical model improvement

A second recommendation is to enhance the dynamical model by incorporating fourth-body perturbations in the ERTBP to maintain constant dynamics throughout the entire transfer. To simplify the problem, this was not done in this thesis, and a change in dynamical model is made at linkage Q. Incorporating fourth-body perturbations would account for gravitational and radiation pressure effects from the other system's bodies. Because the velocity increase/decrease mainly occurs during the start and end of the phases, where accelerations from the central bodies dominate over perturbing forces, making this simplification is considered reasonable. Nevertheless, it can be interesting to test whether the results change when adding fourth-body perturbations. Especially if the sail is far away from both systems and gravitational/radiation effects from both systems are almost equal (although both are very small).

Tuning of the departure/arrival locations
Another recommendation is to consider using artificial equilibrium points as departure/arrival points instead of the classic Lagrange points. Artificial equilibrium points are equilibrium solutions in the elliptic restricted three-body problem, enhanced with a satellite/body that is able to produce a continuous low thrust, such as a photon sail. An artificial equilibrium point is dependent on the sail attitude and lightness number, therefore, by controlling/adjusting the attitude, the equilibrium location can be shifted. In theory, there exist an infinite amount of AEPs, making the departure/arrival point a potential optimization variable. As the results of this work showed, especially the departure location was of great influence on the results, mainly because of its impact on the velocity build-up. By exploiting AEPs as departure locations, the velocity at a Poincaré surface can be controlled, which would make it much easier to find good connections with the arrival phase.

Sensitivity analysis
To advance this work, it is recommended to conduct a sensitivity analysis to evaluate the impact of small variations in the initial conditions and parameters used. Especially since there is much uncertainty in the astronomical data of the Alpha Centauri system. For example, the orbital parameters of AC-C about AC-A/AC-B are not yet confirmed by multiple sources; therefore, it can be expected that this data contains significant uncertainties. Furthermore, the angles used to transform a state from the AC-C -centered frame to the AC-A/AC-B -centered frame are all subject to high uncertainties since there is also little data on Proxima b's orbit yet, and some assumptions had to be made on its Kepler elements. For example, in this research an inclination of $i = 45$ degrees was assumed for Proxima b, while this parameter is of large influence on the results because it determines what sail attitude is needed during arrival phase to find a good transfer. Therefore a sensitivity analysis on the influence of the orbital parameters of AC-C and Proxima b would significantly increase the scientific impact of this research.

Other photon-sail missions in the AC-C/Proxima b system
Finally, it is suggested to further explore the potential of photon sails in the AC-C/Proxima b system. Now that a first estimation of the travel time to this system is known, mission applications *within* that system can be investigated. For example, finding periodic orbits, optimizing trajectories from the Lagrange points to an orbit about Proxima b, flyby missions on Proxima b, or trajectory optimization between the Lagrange points. There are still many opportunities to investigate, given Proxima b's proximity and its status as the closest known rocky exoplanet, making missions related to Proxima b scientifically valuable.

References

[1] Thompson, J. E. S. et al. (1974). Maya astronomy. *Philosophical Transactions of the Royal Society of London. Series A, Mathematical and Physical Sciences*, *276*(1257), 83–98. https://doi.org/10.1098/rsta.1974.0011

[2] Condos, T. (1997). *Star myths of the greeks and romans: A sourcebook containing "the constellations" of pseudo-eratosthenes and the "poetic astronomy" of hyginus*.

[3] Forward, R. L. (1986). Feasibility of interstellar travel: A review. *Acta Astronautica*, *14*, 243–252. https://doi.org/https://doi.org/10.1016/0094-5765(86)90126-8

[4] Long, K., Obousy, R., & Hein, A. (2011). Project icarus: Optimisation of nuclear fusion propulsion for interstellar missions. *Acta Astronautica*, *68*(11), 1820–1829. https://doi.org/https://doi.org/10.1016/j.actaastro.2011.01.010

[5] Lubin, P. (2016). *A Roadmap to Interstellar Flight* (tech. rep.).

[6] Perakis, N. et al. (2016). Project dragonfly: A feasibility study of interstellar travel using laser-powered light sail propulsion. *Acta Astronautica*, *129*, 316–324. https://doi.org/https://doi.org/10.1016/j.actaastro.2016.09.030

[7] Bae, Y. K. (2012). Prospective of photon propulsion for interstellar flight [Space, Propulsion Energy Sciences International Forum]. *Physics Procedia*, *38*, 253–279. https://doi.org/https://doi.org/10.1016/j.phpro.2012.08.026

[8] Thévenin, F. et al. (2002). Asteroseismology and calibration of alpha cen binary system. *Astronomy and Astrophysics*, *392*. https://doi.org/10.1051/0004-6361:20021074

[9] Kervella, P. et al. (2003). *A family portrait of the alpha centauri system*. Retrieved January 29, 2022, from https://www.eso.org/public/news/eso0307/#1

[10] Suarez Mascareno, A. et al. (2020). Revisiting proxima with espresso. *Astronomy Astrophysics*, *639*. https://doi.org/10.1051/0004-6361/202037745

[11] Bixel, A., & Apai, D. (2017). Probabilistic constraints on the mass and composition of proxima b. *836*(2), L31. https://doi.org/10.3847/2041-8213/aa5f51

[12] Benedict, G. F., & McArthur, B. E. (2020). A preliminary mass for proxima centauri c. *4*(4), 46. https://doi.org/10.3847/2515-5172/ab84f3

[13] Sackmann, I. J., Boothroyd, A. I., & Kraemer, K. E. (1993). Our sun. iii. present and future. *The Astrophysical Journal*, *418*, 457–468.

[14] Urbanczyk, M. (1965). Solar sails - a realistic propulsion for spacecraft. *Astronautyka*, *3*, 20–23.

[15] McInnes, C. R. (1999). *Solar sailing: Technology, dynamics, and mission applications* (2nd ed.). https://doi.org/10.1007/978-1-4471-3992-8

[16] Mori, O. et al. (2010). First solar power sail demonstration by ikaros. *Transactions of the Japan Society for Aeronautical and Space Sciences, Aerospace Technology Japan*, *8*. https://doi.org/10.2322/tastj.8.to_4_25

[17] Spencer, D. et al. (2020). The lightsail 2 solar sailing technology demonstration. *Advances in Space Research*, *67*. https://doi.org/10.1016/j.asr.2020.06.029

[18] Vulpetti, G., Johnson, L., & Matloff, G. L. (2015). The nanosail-d2 nasa mission. *Solar sails: A novel approach to interplanetary travel* (pp. 173–178). Springer New York. https://doi.org/10.1007/978-1-4939-0941-4_16

[19] Wilkie, W. et al. (2021). An overview of the nasa advanced composite solar sail (acs3) technology demonstration project.

[20] Heller, R., & Hippke, M. (2017). Deceleration of high-velocity interstellar photon sails into bound orbits at Alpha Centauri. *The American Astronomical Society*, *835*(2). https://doi.org/10.3847/2041-8213/835/2/L32

[21] Heller, R., Hippke, M., & Kervella, P. (2017). Optimized Trajectories to the Nearest Stars Using Lightweight High-velocity Photon Sails. *The Astronomical Journal*, *154*(3), 115. https://doi.org/10.3847/1538-3881/aa813f

[22] Forgan, D. H., Heller, R., & Hippke, M. (2018). Photogravimagnetic assists of light sails: A mixed blessing for Breakthrough Starshot? *Monthly Notices of the Royal Astronomical Society*, *474*(3), 3212–3220. https://doi.org/10.1093/mnras/stx2834

[23] Pino, T., & Circi, C. (2017). A star-photon sailcraft mission in the Alpha Centauri system. *Advances in Space Research*, *59*(9), 2389–2397. https://doi.org/10.1016/j.asr.2017.02.014

[24] Aliasi, G., Mengali, G., & Quarta, A. A. (2014). Artificial equilibrium points for a solar balloon in the α Centauri system. *Acta Astronautica*, *104*(2), 464–471. https://doi.org/10.1016/j.actaastro.2014.03.006

[25] Heiligers, J., Schoutetens, F., & Dachwald, B. (2021). Photon-sail equilibria in the alpha centauri system. *Journal of Guidance, Control, and Dynamics*, *44*(5), 1053–1061. https://doi.org/10.2514/1.g005446

[26] Farres, A., Heiligers, J., & Miguel Baños, N. (2018). Road map to l4/l5 with a solar sail. https://doi.org/10.2514/6.2018-0211

[27] Heiligers, J., Mingotti, G., & McInnes, C. R. (2015). Optimal solar sail transfers between halo orbits of different sun-planet systems. *Advances in Space Research*, *55*(5), 1405–1421. https://doi.org/10.1016/j.asr.2014.11.033

[28] Vergaaij, M., & Heiligers, J. (2018). Time-optimal solar sail heteroclinic-like connections for an earth-mars cycler. *Acta Astronautica*, *152*. https://doi.org/10.1016/j.actaastro.2018.08.008

[29] Peng, H. et al. (2017). Libration transfer design using patched elliptic three-body models and graphics processing units. *Journal of Guidance, Control, and Dynamics*, *40*, 1–12. https://doi.org/10.2514/1.G002692

[30] Wakker, K. F. (2015). *Fundamentals of astrodynamics*.

[31] Szebehely, V. (1967). Theory of orbits (1st ed.).

[32] Schoutetens, F. (2019). *Photon-sail trajectory optimization in alpha centauri using evolutionary neurocontrol thesis aee888* (Master's thesis). http://repository.tudelft.nl/.

[33] Gaia data processing and analysis consortium (dpac), gaia data release 2 [Online; accessed 5-Jan-2023]. (2019). https://gea.esac.esa.int/archive/documentation/GDR2/

[34] Akeson, R. et al. (2021). Precision millimeter astrometry of the α centauri ab system. *The Astronomical Journal*, *162*. https://doi.org/10.3847/1538-3881/abfaff

A

Verification & Validation

In this appendix, the verification and validation of the dynamical model and numerical methods is given. Verification and validation is a crucial part of this thesis, since it is meant to ensure the correctness and relevance of this research to science. The first section of Appendix A will describe the verification of the dynamical model, including the ERTBP, computation of manifolds, and the computation of the Monodromy matrix. The second section of Appendix A describes the verification of four frame transformations used: from the $\mathcal{P}_i$-frame to the $\mathcal{I}_i$-frame, from the $\mathcal{I}_i$-frame to the $\mathcal{O}_i$-frame, from the $\mathcal{E}_i$-frame to the $\mathcal{G}_i$-frame, and from the $\mathcal{G}_a$-frame to the $\mathcal{G}_d$-frame. Subscript i = d, a, so the frame transformations for frames with this subscript can be applied to both the departure or the arrival system.

A.1. Dynamical model

To verify that the equations of motion for a photon-sail augmented ERTBP are correctly implemented, the Artificial Equilibrium Points (AEPs) of the system are calculated. AEPs are mathematically similar to Lagrange points, but including the photon-sail acceleration. Secondly, the computation of manifolds is verified against literature, since these form the basis of the heteroclinic connections that are used in this research. Because no literature is available on manifolds in the ERTBP, this is done in the CRTBP. Therefore, one additional verification must be done: the computation of the Monodromy matrix. Computation of the Monodromy matrix is necessary to obtain a manifold in the ERTBP. Therefore, the verification of this matrix, together with the verification of the computation of manifolds, will ensure that the manifolds in the ERTBP are computed correctly.

A.1.1. SS-ERTBP

In reference [25], the contour plots, that connect artifial equilibrium points (AEPs) of similar sail performance in the Alpha Centauri A/B system, are given. These can be used to verify the implementation of the photon-sail augmented ERTBP. To do this, the same parameters (gravitational parameter μ_d, luminosity L_A and L_B, eccentricity e_d) as in the paper is used, and three different cases are presented. The first case considers the contour plots of the AC-A/AC-B system (A.1 for a one-sided ideal sail. The second case considers those for a double-sided ideal sail. In this way, also the implementation of the double-sided sail model is verified. Thirdly, the contour plots for the system with AC-B's luminosity set to zero are given to mimic the arrival system. The plots from the paper (left) exactly comply with the computed plots (right), therefore, it can be concluded that the equations of motion are correctly implemented. Note that the equations of motion for the arrival system are the same as for case 3: an ERTBP with only one radiation body, instead of two. So the implementation for the arrival equations do not have to be separately verified.

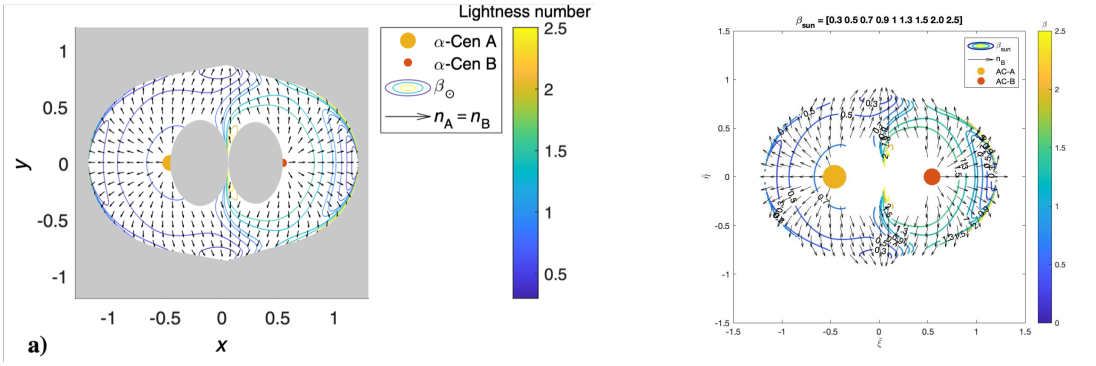

(a) (b)

Figure A.1: (a) Contour plot of the artificial equilibria in the photon-sail augmented ERTBP model applied to the AC-A/AC-B system, using a one-sided ideal sail [25]. (b) Computed contour plot, using the same parameters and contour lines. Each contour line represents one specific lightness number β.

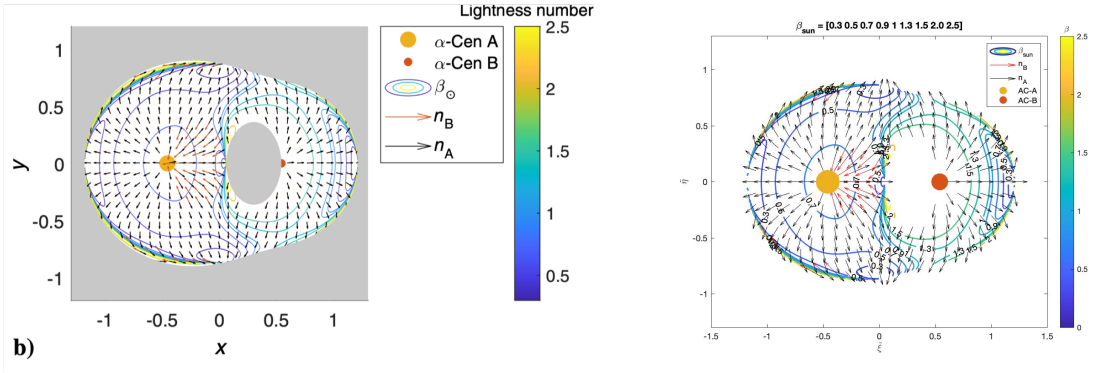

(a) (b)

Figure A.2: (a) Contour plot of the artificial equilibria in the photon-sail augmented ERTBP model applied to the AC-A/AC-B system, using a double-sided ideal sail [25]. (b) Computed contour plot, using the same parameters and contour lines. The dynamical model for a double-sided sail is applied. Each contour line represents one specific lightness number β.

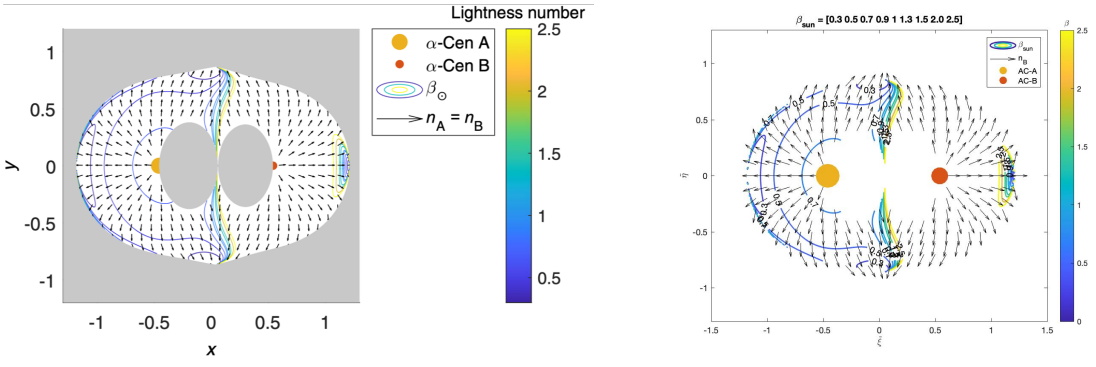

(a) (b)

Figure A.3: (a) Contour plot of the artificial equilibria in the photon-sail augmented ERTBP model applied to the AC-A/AC-B system, using a one-sided ideal sail and with the luminosity of AC-B set to zero [25]. (b) Computed contour plots, using the same parameters and contour lines. Luminosity of AC-B is set to zero. Each contour line represents one specific lightness number β.

A.1.2. Manifolds

The computation of the manifolds requires the perturbation of the state at an equilibrium point, in the direction of the eigenvectors of the Jacobian (CRTBP) or the Monodromy matrix (ERTBP). Motion

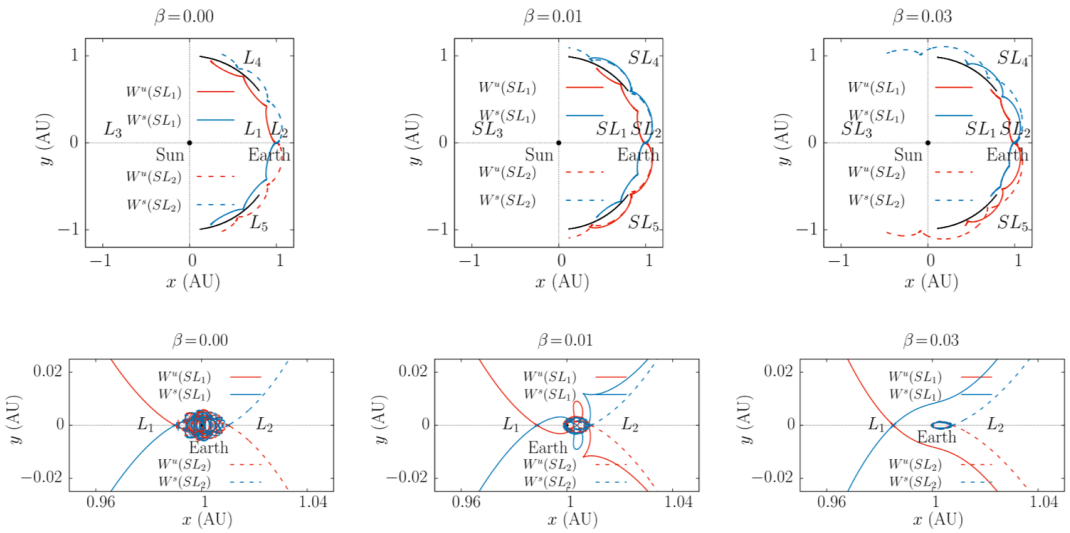

Figure A.4: Manifolds in the Sun-Earth system for three different values of β [26], where the bottom plots show zoomed in figures.

associated with the imaginary eigenvalues of the Jacobian/Monodromy matrix can be excited to obtain stable or periodic motion. Similarly, the motion associated with the real eigenvalues can be excited to create unstable behavior. By doing this, asymptotic motion towards or away from this equilibrium point is induced. These trajectories are called manifolds. The state is forward propagated to obtain the unstable manifold, and backwards propagated to obtain the stable manifold. In [26], three different examples of manifolds are given for the Sun-Earth system, each representing the manifold of a different lightness number. As can be seen from Figs. A.5, A.6, and A.7, the computed manifolds are in exact agreement with the manifolds presented in the paper (Fig. A.4). Minor differences occur because the exact propagation time was not correctly specified in the paper. But, it can be concluded from these plots that the computation of manifolds in the CRTBP is done correctly.

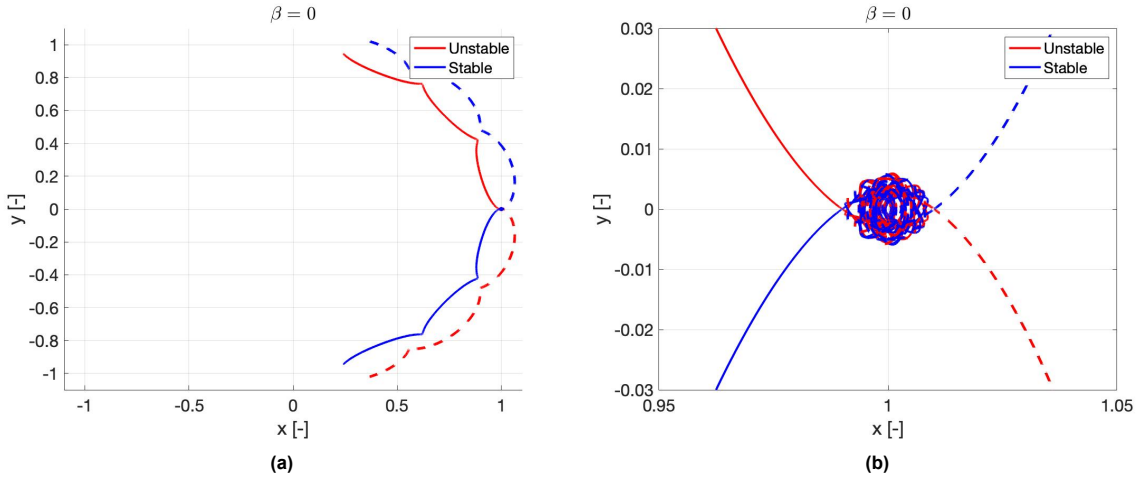

Figure A.5: Computed manifolds using the same initial conditions and lightness number (β=0) as in [26].

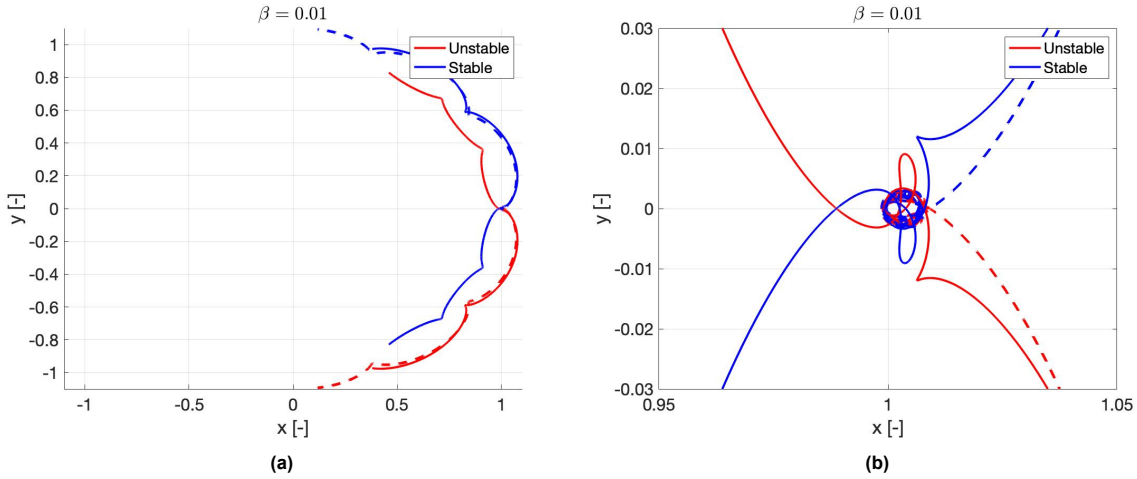

Figure A.6: Computed manifolds using the same initial conditions and lightness number (β=0.01) as in [26].

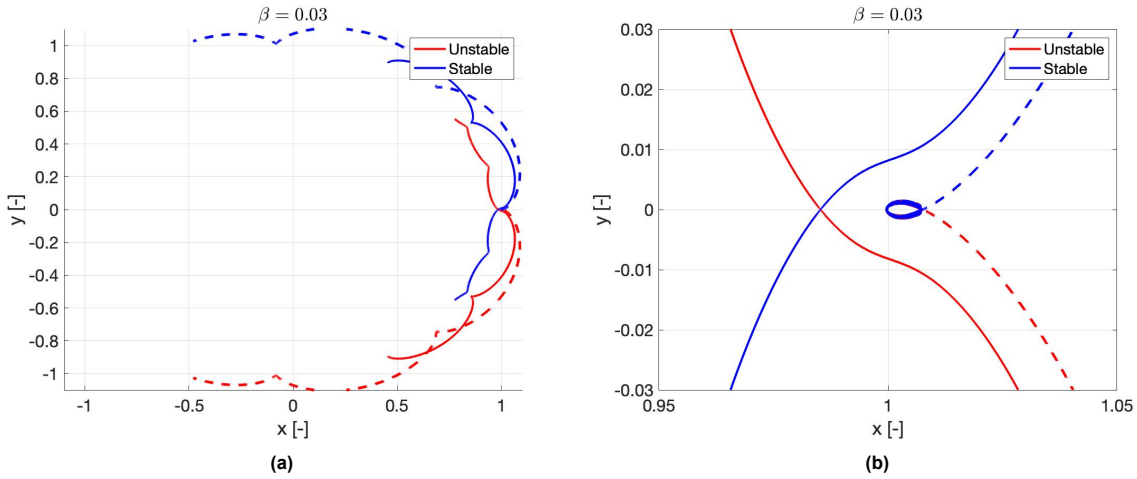

Figure A.7: Computed manifolds using the same initial conditions and lightness number (β=0.03) as in [26].

A.1.3. Monodromy matrix

The verification of the Monodromy matrix is done by comparing to stability plots found in [25]. There, the stability of equilibrium solutions in the AC-A/AC-B system is investigated by linearizing around the equilibrium point. Following the same approach as described there, the Monodromy matrix is computed and its eigenvalues λ_i are determined to analyse the stability. The linearized system is said to be stable if $|\lambda_i| \leq 1$. If $|\lambda_i| \leq 1 + \Delta$ holds, the system is almost stable, where Δ must be a small number. The plots from the paper are given in Fig. A.8; the top plots give the stability regions of the system for both a one-sided and double-sided sail, where black, dark-gray, white and light-gray indicate, respectively, unstable, almost-stable, stable, and infeasible motion. The bottom plots are zoomed in on a specific region in the double-sided plot, for different values of Δ. As can be seen, the computed stability regions (Figs. A.9 and A.10) are in agreement with the plots presented in Fig. A.8. Therefore, the computation of the Monodromy matrix is considered verified.

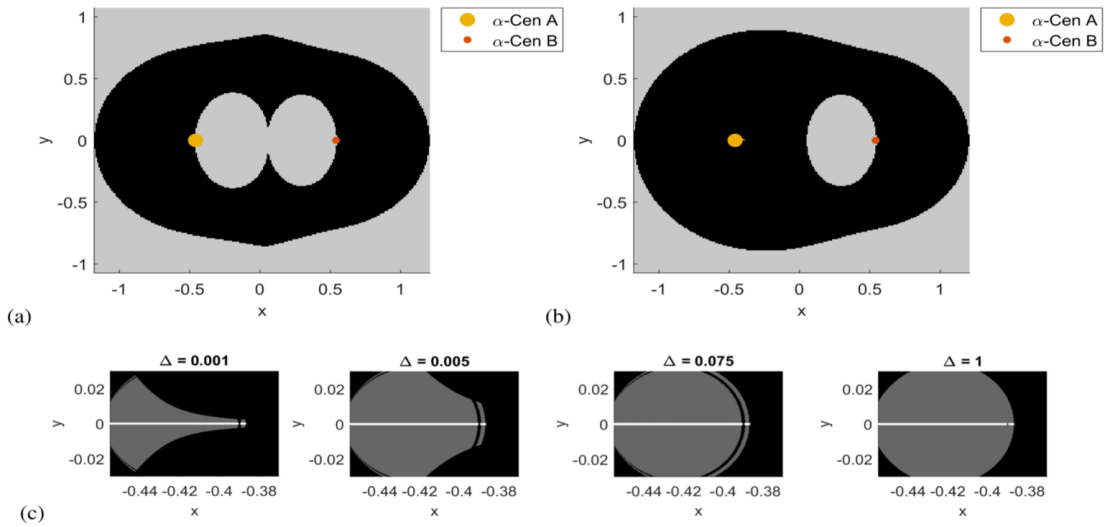

Figure A.8: Stability regions in the AC-A/AC-B system for a one-sided and double-sided sail [25]. In the plots, black, dark-gray, white and light-gray indicate, respectively, unstable, almost-stable, stable, and infeasible.

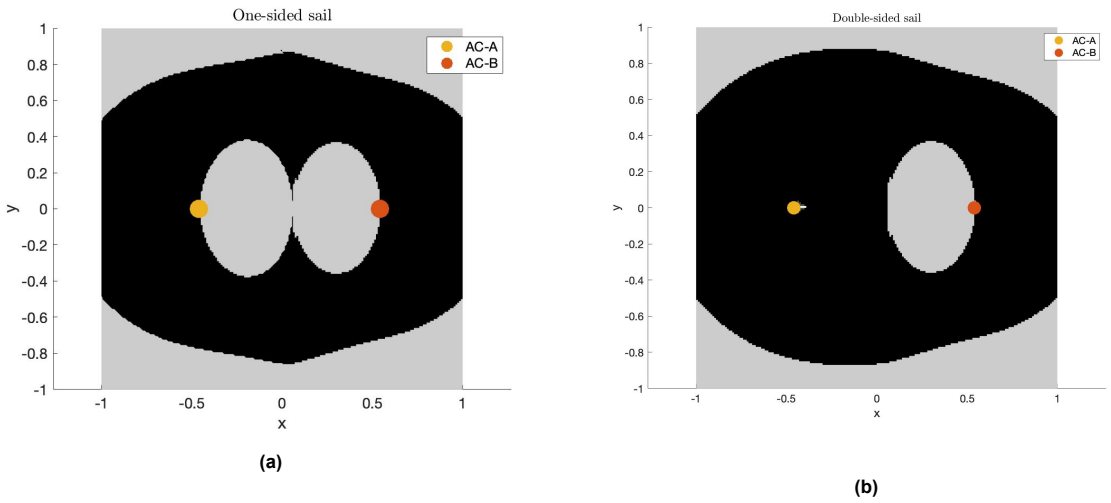

Figure A.9: Computed stability region plots for the AC-A/AC-B system, using both a one and double-sided sail configuration.

A.2. Frame Transformations

In this section, the verification of four frame transformations will be discussed. The first one is the transformation from the rotating pulsating barycentric frame $\mathcal{P}_i$ to the inertial frame $\mathcal{I}_i$. This transformation can be applied to both the departure and arrival system (so from $\mathcal{P}_d$ to $\mathcal{I}_d$, or from $\mathcal{P}_a$ to $\mathcal{I}_a$). The second one is the transformation from the inertial frame $\mathcal{I}_i$ to the observer frame $\mathcal{O}_i$. Again, this transformation can be applied to both systems. The third transformation converts a state from the observer frame $\mathcal{O}_i$ to the galactic frame $\mathcal{G}_i$, once more it can be applied to both systems. The last transformation is used to convert a state from the arrival galactic frame $\mathcal{G}_a$ to the departure galactic frame $\mathcal{G}_d$, which is merely a translation from AC-C to the barycenter of AC-A/AC-B.

A.2.1. Rotating pulsating barycentric frame $\mathcal{P}_i$ to inertial frame $\mathcal{I}_i$

The verification of the transformation from the rotating pulsating barycentric frame to the inertial frame is done in two steps. To do this, a trajectory in the rotating pulsating barycentric frame $\mathcal{P}_i$ is computed

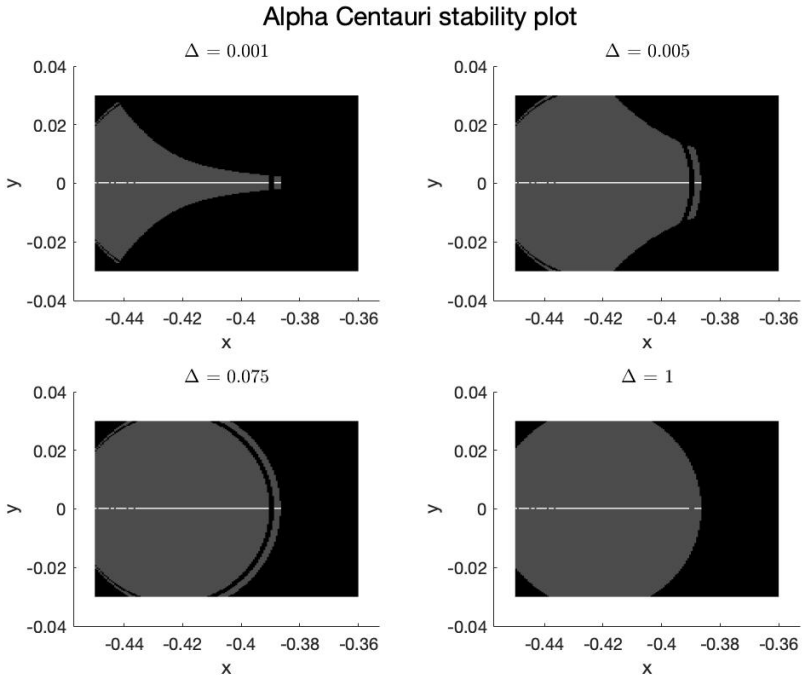

Figure A.10: Computed stability region plots for the AC-A/AC-B system, zoomed in on a specific area of the double-sided sail configuration plot, using different values of Δ.

and entirely (at each timestep) transformed to the inertial frame $\mathcal{I}_i$. The initial conditions in the $\mathcal{P}_i$-frame are given as: $\mathbf{x}_0|_{\mathcal{P}_i}$. The second step consists of propagating a trajectory in the $\mathcal{I}_i$-frame. To do this, initial conditions $\mathbf{x}_0|_{\mathcal{P}_i}$ are transformed to the $\mathcal{I}_i$-frame, with the new initial conditions given as: $\mathbf{x}_0|_{\mathcal{I}_i}$. Both trajectories are propagated over the same time interval. Note that the time is dimensionless in the $\mathcal{P}_i$-frame, so this dimensionless time θ_i must also be converted to dimensional time t_i, in order to let propagate both trajectories over the same interval. The transformed trajectory (propagated in $\mathcal{P}_i$ and converted to $\mathcal{I}_i$ for each timestep) and the trajectory propagated in the $\mathcal{I}_i$-frame can then be compared. Ideally, they should overlap and end in the same final state.

To execute the above explained verification, the equations of motion of a sail in the inertial frame must be written out. These differ from the equations of motion of the photon-sail augmented ERTBP, in which the rotation of the frame is taken into account. The equations of motion can easily be obtained. In fact, the starting point of the derivation of the equations for the ERTBP give the equations needed. From [30], it is known that the equations of motion of a massless particle in the inertial frame are given as:

$$\ddot{\mathbf{r}}|_I = -G\left(\frac{m_1}{r_1^3}\mathbf{r}_1 + \frac{m_2}{r_2^3}\mathbf{r}_2\right) \tag{A.1}$$

with the masses of the primary bodies m_1 and m_2 , gravitational constant G, and the position vectors relative to the primary bodies, $\mathbf{r}_1$ and $\mathbf{r}_2$. Equation A.1 holds under the assumptions that; the two bodies rotate in elliptic orbits about their common barycenter, the mass of the third body is negligible, and no additional perturbations are exerted on the third mass except the gravitational forces from the primary bodies. So, when adding the sail acceleration, this becomes:

$$\ddot{\mathbf{r}}|_I = -G\left(\frac{m_1}{r_1^3}\mathbf{r}_1 + \frac{m_2}{r_2^3}\mathbf{r}_2\right) + \mathbf{a}_s \tag{A.2}$$

The position vectors relative to the primary bodies, $\mathbf{r}_1$ and $\mathbf{r}_2$, are defined as:

$$\mathbf{r}_1 = \begin{bmatrix} X + \rho * \mu * cos(\theta) \\ Y + \rho * \mu * sin(\theta) \\ Z \end{bmatrix} \tag{A.3}$$

$$\mathbf{r}_2 = \begin{bmatrix} X - \rho * (1-\mu) * cos(\theta) \\ Y - \rho * (1-\mu) * sin(\theta) \\ Z \end{bmatrix} \tag{A.4}$$

where X, Y, Z are the position coordinates in the inertial frame, the true anomaly is denoted using θ, and the instantaneous distance between the primaries ρ is given as:

$$\rho = \frac{s(1-e^2)}{1 + e\cos\theta}, \tag{A.5}$$

with the semi-major axis s and eccentricity e. In this verification, a one-starred system is considered, and the sail acceleration is given as:

$$\mathbf{a}_s = \frac{\beta_\odot (1-\mu)}{\|\mathbf{r}_1\|^2} (\hat{\mathbf{r}}_1 \cdot \hat{\mathbf{n}})^2 \hat{\mathbf{n}} \tag{A.6}$$

where the sail normal vector $\mathbf{n}$ is defined using the cone/clock angle α and δ:

$$\hat{\mathbf{n}}|_{\mathcal{S}} = \begin{pmatrix} \cos\alpha & \sin\alpha\sin\delta & \sin\alpha\cos\delta \end{pmatrix}^\top \tag{A.7}$$

the cone and clock angle are defined relative to $\mathbf{r}_1$ and given in the local sail-centered frame $\mathcal{S}_i$. The frame definition is not relevant in this section, but the conversion from this frame to the $\mathcal{P}_i$-frame is given as:

$$\hat{\mathbf{n}}|_{\mathcal{P}_i} = \hat{\mathbf{n}} = \begin{bmatrix} \hat{\mathbf{r}}_i & \hat{\boldsymbol{\theta}}_i & \hat{\boldsymbol{\eta}}_i \end{bmatrix} \hat{\mathbf{n}}\Big|_{\mathcal{S}_i} \tag{A.8}$$

after which the transformation from $\mathcal{P}_i$ to $\mathcal{I}_i$ is done in a similar manner as for the state vector. The trajectories are propagated using tolerances of 10^{-10}, a lightness number $\beta = 0.5$, cone and clock angle $\alpha = 0$, $\delta = 0$. A fictional system is used with an eccentricity of $e = 0.0167$ and a mass parameter of $\mu = 0.4$. The trajectories are propagated over three periods of the fictional system. Two different initial states $\mathbf{x}_0|_{\mathcal{P}_i}$ were used to increase the robustness of this verification: $[0.7, 0.8, 0.0, 0.0000000006, 0.0031, -0.00000004]$ and $[0.95, 0.003, 0.015, 0.00000043, 0.00051, 0.00008]$

For both initial conditions, the verification trajectories are given in Figs. A.11 and A.12. So, the trajectory propagated in the $\mathcal{P}_i$-frame and transformed to $\mathcal{I}_i$, and the trajectory for which only the initial conditions are transformed to the $\mathcal{I}_i$-frame, and are propagated in the $\mathcal{I}_i$-frame. When looking at Figures A.11 and A.12, it can be concluded that there is a good overlap. The Euclidean norm differences between the final states are, for both cases, 2.3187 km/1.6301$*10^{-4}$ m/s, and 1.87 km/0.0026 m/s. The minor differences are likely to be caused by integration errors, since both trajectories use different equations of motion and different $\mathbf{r}_1$ and $\mathbf{r}_2$ vectors.

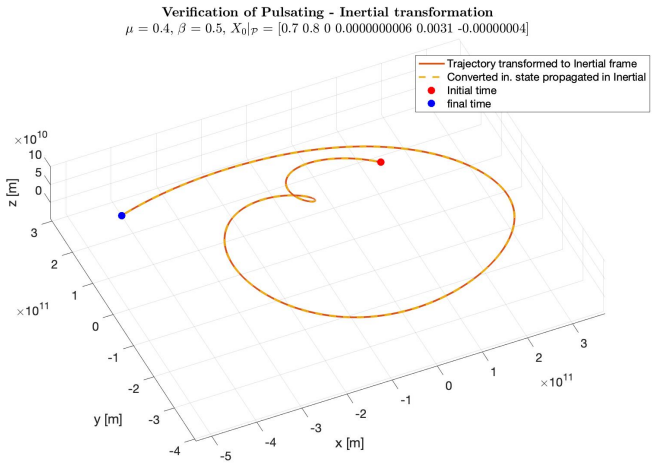

Figure A.11: Comparison between the transformed trajectory and the trajectory propagated in the inertial frame. The Euclidean norm position difference is 2.3187 km. The Euclidean norm velocity difference is 1.6301$*10^{-4}$ m/s.

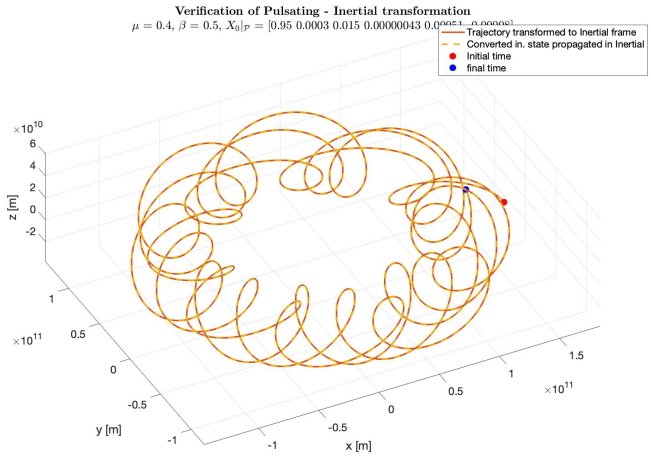

Figure A.12: Comparison between the transformed trajectory and the trajectory propagated in the inertial frame. The Euclidean norm position difference is 1.87 km. The Euclidean norm velocity difference is 0.0026 m/s.

Although the above presented results give base for the conclusion that the transformation is correct, there is the possibility of a systematic error in the transformation. A systematic error can result in a wrong transformed trajectory from $\mathcal{P}_i$ to $\mathcal{I}_i$-frame. This error will then also exist in the initial state $\mathbf{x}_0|_{\mathcal{I}_i}$ used for the propagation in the $\mathcal{I}_i$-frame, possibly resulting in an overlapping trajectory. This could lead to a wrong conclusion that the transformation is correct. To rule out the possibility of a systematic error in the transformation, an additional verification step is taken. For this, it is convenient to use an analytical solution that is known in both frames. In this way, the initial states for propagation in both the $\mathcal{P}_i$ and $\mathcal{I}_i$-frames can be calculated separately from each other. The same procedure is then applied, but now the initial state in the $\mathcal{I}_i$-frame propagation is not dependent on the transformation. An example of a known solution in both frames are the Lagrange points in the Sun-Earth system ($e = 0.0167$, $\beta = 0$). Note that the Lagrange points in the $\mathcal{P}_i$-frame are fixed in time, while in the $\mathcal{I}_i$-frame they will rotate along with the primary bodies. So the Lagrange points are calculated at $t = 0$.

Following the equations described in literature [31], the L_4 and L_5 points can be analytically calculated in both frames, see Table A.1. Table A.1 also give the transformed L_4 and L_5 points, which are (almost) exactly the same. This confirms the preliminary conclusions that the transformation is correct. In addition, the propagated trajectories are given in Figures A.13 and A.14. Note that these trajectories simply represent the motion of the L_4 and L_5 points in time. The L_4 and L_5 points are stable in the Sun-Earth system, so a massless particle placed there will stay there (although in reality, perturbing forces could make a spacecraft drift away over time). The small differences in final states after three Sun-Earth (Eucl. norm), given in Table A.2, are thus caused by numerical integration errors.

Table A.1: L_4 and L_5 analytically determined in the $\mathcal{P}_i$-frame and in the$\mathcal{I}_i$-frame (columns 1-4). Columns 5-6 give the L_4 and L_5 points transformed from the $\mathcal{P}_i$-frame to the $\mathcal{I}_i$-frame.

	L_4 analytic in $\mathcal{P}_i$-frame (dimensionless units)	L_5 analytic in $\mathcal{P}_i$-frame (dimensionless units)	L_4 analytic position in $\mathcal{I}_i$-frame at $t = 0$ [m - m/s]	L_5 analytic in $\mathcal{I}_i$-frame at $t = 0$ [m - m/s]	L_4 transformed from $\mathcal{P}_i$ to $\mathcal{I}_i$-frame at $t = 0$ $[m - m/s]$	L_5 transformed from $\mathcal{P}_i$ to $\mathcal{I}_i$-frame at $t = 0$ $[m - m/s]$
x	0.499996996639646	0.499996996639646	0.735504698561195*1$*10^{11}$	0.735504698561195*1$*10^{11}$	0.7355046985611955*1$*10^{11}$	0.7355046985611955*1$*10^{11}$
y	0.866025403784439	-0.866025403784439	1.273939159310350*1$*10^{11}$	-1.273939159310350*1$*10^{11}$	1.273939159310351*1$*10^{11}$	-1.273939159310351*1$*10^{11}$
z	0	0	0	0	0	0
$\dot{x}$	0	0	-2.622915961910904$*10^4$	2.622915961910904$*10^4$	-2.622915961910904$*10^4$	2.622915961910904$*10^4$
$\dot{y}$	0	0	1.514332140446162$*10^4$	1.514332140446162$*10^4$	1.514332140446162$*10^4$	1.514332140446162$*10^4$
$\dot{z}$	0	0	0	0	0	0

Table A.2: Euclidean norm errors after propagation over three periods of the Sun-Earth system.

Euclidean norm difference after 3 periods	Position $[km]$	Velocity $[m/s]$
L_4	0.357	7.2e-05
L_5	0.374	7.6e-05

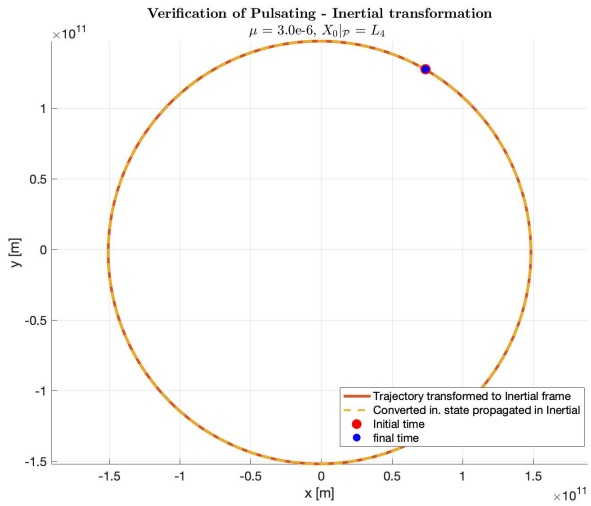

Figure A.13: Comparison between the transformed trajectory and the trajectory propagated in the inertial frame. The trajectory represent the motion of the L_4 point over three periods of the Sun-Earth system.

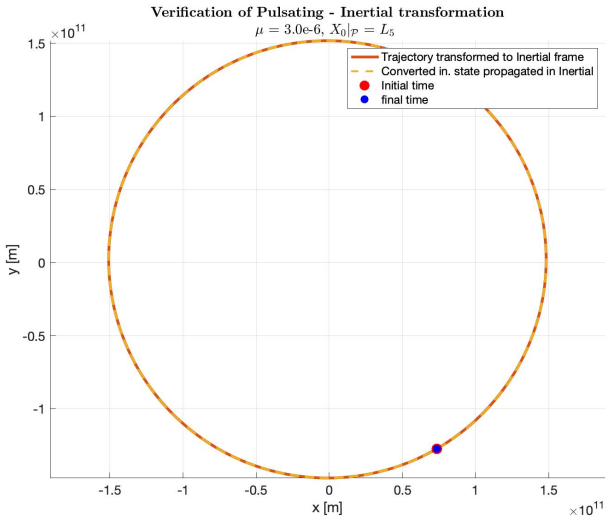

Figure A.14: Comparison between the transformed trajectory and the trajectory propagated in the inertial frame. The trajectory represent the motion of the L_5 point over three periods of the Sun-Earth system.

From the above presented work it can be concluded that the frame transformation from the rotating pulsating barycentric frame $\mathcal{P}_i$ to the inertial frame $\mathcal{I}_i$ is verified.

A.2.2. Inertial frame $\mathcal{I}_i$ to observer frame $\mathcal{O}_i$

The transformation used to convert a state vector from the inertial frame $\mathcal{I}_i$ to the observer frame $\mathcal{O}_i$ consists of three rotations. In essence, it is therefore only necessary to verify that the rotation matrices are correctly implemented. To do this, Figures A.15 and A.16 (obtained from [32]) are used. Figure A.15 describes the motion of AC-A and AC-B about their barycenter, in the inertial frame. Figure A.16 describes the motion of AC-A and AC-B about their barycenter in the observer frame.

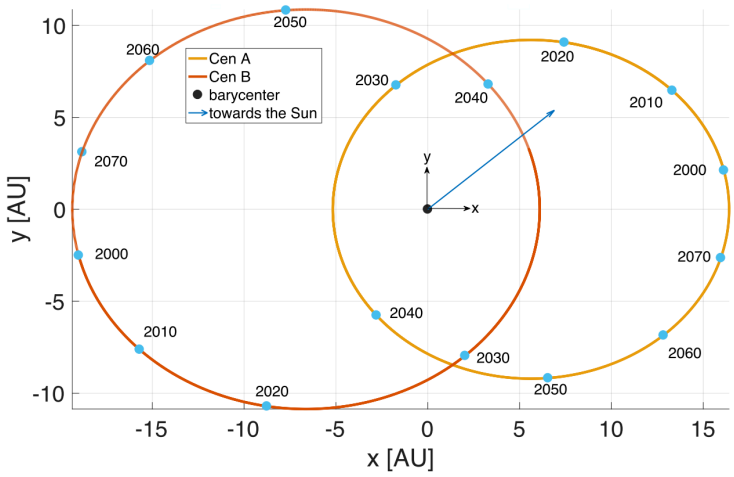

Figure A.15: Orbital trajectories of AC-A and AC-B about the barycenter in the orbital plane, with the blue arrow indicating the Sun's direction (inclined with 10.68° with respect to the orbital plane). Obtained from [32].

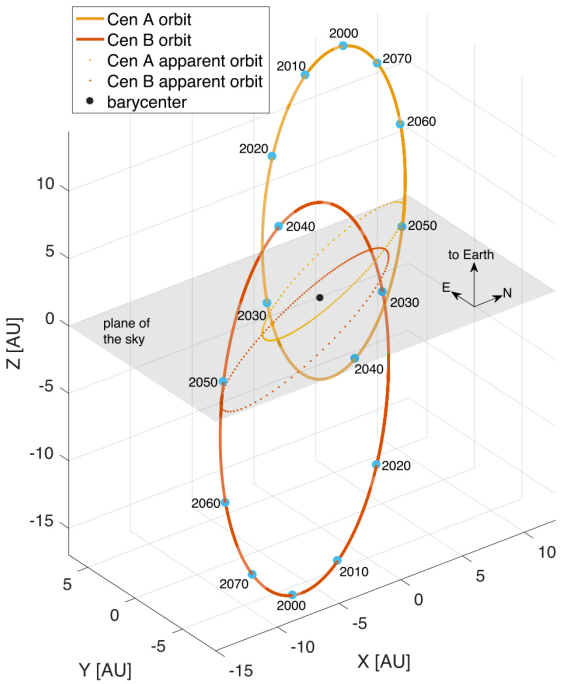

Figure A.16: Orbital trajectories of AC-A and AC-B about the barycenter, 3D-view with the projection of the orbits on the plane of the sky representing the apparent orbits as dots. Obtained from [32].

Following a procedure described in [30], the Kepler elements of the orbits provided in [32] can be converted to Cartesian elements. In this way, Figures A.15 and A.16 are reproduced, see Figures A.17

and A.18. Note that the implementation of the conversion of Kepler elements into Cartesian elements is directly verified in this step by reproducing Figures A.15 and A.16.

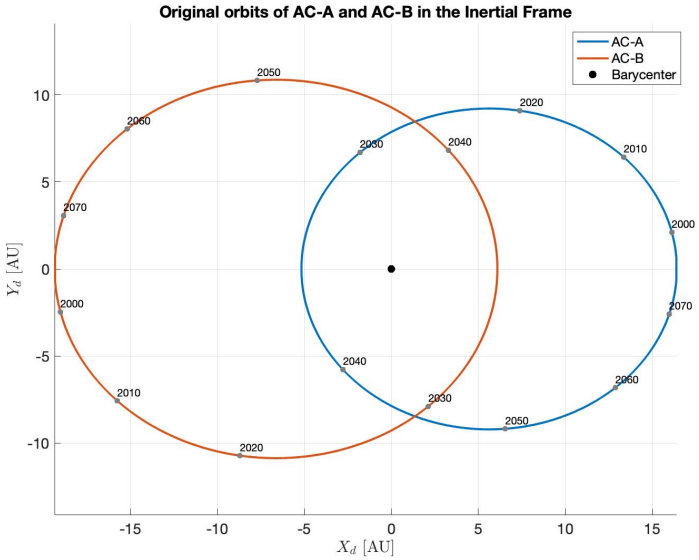

Figure A.17: Orbital trajectories of AC-A and AC-B about the barycenter in the inertial frame.

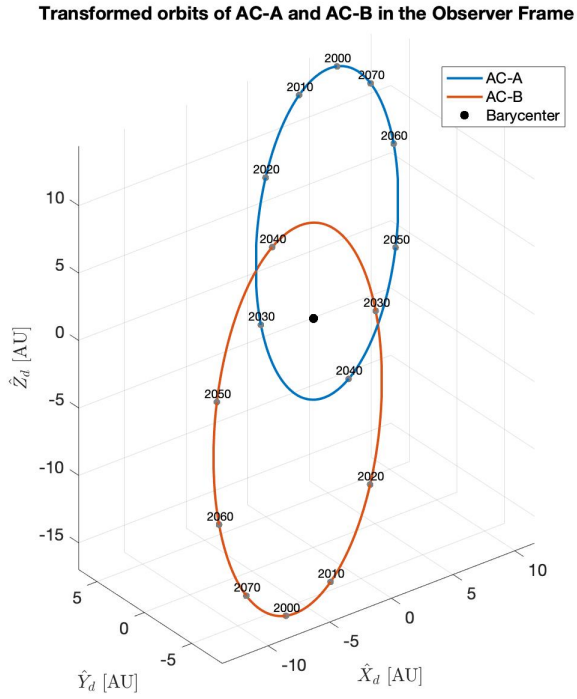

Figure A.18: Orbital trajectories of AC-A and AC-B about the barycenter in the observer frame.

Finally, the verification of the implementation of the frame transformation is done by taking the orbits displayed in Figs. A.15 and A.17, so the orbits in the inertial frame, and transforming the entire orbit into the observer frame. The result should be two orbits that are exactly similar to the orbits displayed

in Figs. A.16 and A.18. Figure A.19 shows that this is indeed accomplished. There, the orbits in inertial frame are given by red and blue lines, and the transformed orbits in purple. The inverse transformation is also verified. This is done following the same procedure, so taking the orbit from Figure A.16/A.18 and transform them to the inertial frame. Figure A.20 shows the result. To conclude, since the three angles (the right ascension of the ascending node, inclination, and argument of periapsis) with which the rotations are done are constant over time, the transformation is the same for both the position and velocity components of the state vector. It can be concluded that the transformation that converts a state vector from the inertial frame to the observer frame is verified.

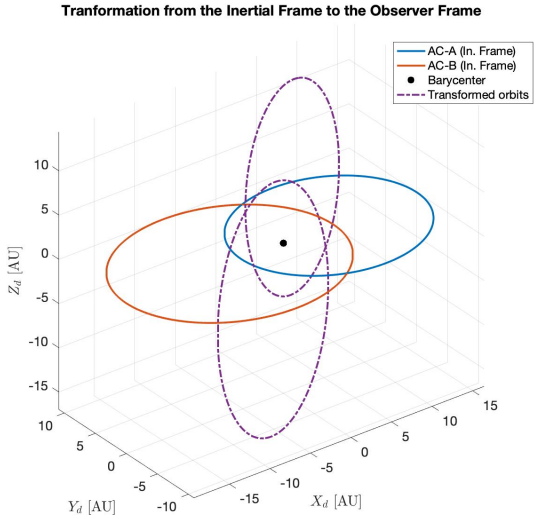

Figure A.19: Representation of the transformation from Inertial to observer frame.

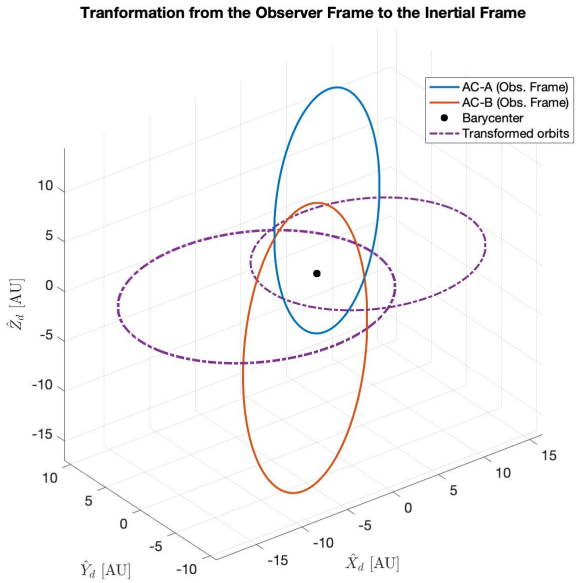

Figure A.20: Representation of the transformation from observer to inertial frame.

A.2.3. ICRS frame $\mathcal{E}_i$ to galactic frame $\mathcal{G}_i$

The transformation from the ICRS frame $\mathcal{E}_i$ to galactic frame $\mathcal{G}_i$ (and its reverse) is verified by using the coordinates of a celestial object in both galactic and ICRS coordinates, obtained from the Simbad database[1]. The Simbad database contains astronomical data on celestial objects. The celestial object can be any, but appropriately the coordinates of AC-C are used. The verification process is based on equations from the Gaia data release [33]. The first step is to calculate the position unit vector of AC-C in the ICRS frame $\mathcal{E}$ with its origin in the barycenter of the Solar system. The position vector of AC-C describes where it is located as seen from the Solar system. The position unit vector can be calculated using the right ascension RA_C and declination DEC_C of AC-C, both obtained from the Simbad database. Then, the transformation from the $\mathcal{E}_i$-frame to the galactic frame $\mathcal{G}_i$ is executed by using matrix $\boldsymbol{D}_{\mathsf{G}}$, provided in the Gaia data release [33]. This transformation thus gives the position unit vector in the $\mathcal{G}_i$-frame. From this position vector, the galactic longitude and latitude l and b can be calculated. These two values will then be compared to the values in Simbad, concluding the verification of this transformation.

So, the position unit vector of AC-C, in the ICRS frame E is calculated using the right ascension RA_C and declination DEC_C of AC-C:

$$\hat{\boldsymbol{r}}_{\mathsf{ICRS}} = \begin{bmatrix} \cos RA_C \cos DEC_C \\ \sin RA_C \cos DEC_C \\ \sin DEC_C \end{bmatrix} \tag{A.9}$$

Then, the transformation is applied using matrix $\boldsymbol{D}_{\mathsf{G}}$:

$$\hat{\boldsymbol{r}}_{\mathsf{Gal}} = \boldsymbol{A}_{\mathsf{G}}^{-1} \hat{\boldsymbol{r}}_{\mathsf{ICRS}} \tag{A.10}$$

The final step is to calculate the galactic longitude and latitude:

$$l_C = \mathsf{atan}\,2\,(\tilde{y}_{\mathsf{Gal}}\,, \tilde{x}_{\mathsf{Gal}}\,) \tag{A.11}$$

$$b_C = \mathsf{atan}\,2\left(\tilde{z}_{\mathsf{Gal}}, \sqrt{\tilde{x}_{\mathsf{Gal}}^2 + \tilde{y}_{\mathsf{Gal}}^2}\right) \tag{A.12}$$

The right ascension, declination, galactic longitude and latitude, obtained from the Simbad database, are:

- RA_C = 217.4289422216058°
- DEC_C = -62.6794901890756°
- l_C = 313.9398620493784°
- b_C = -01.9271491330428°

The calculated values, using steps A.9-A.12, of the galactic longitude and latitude are:

- l_C = 313.9398558803908°
- b_C = -1.927146404534169°

The calculated values are in good agreement with the values obtained from Simbad, although small differences are observed. The difference might occur because the values of the galactic north pole (RA_G, DEC_G) and the galactic longitude of the first intersection of the galactic plane with the equator l_Ω, used in matrix $\boldsymbol{D}_{\mathsf{G}}$ and obtained from the Gaia data release [33], are slightly different then the values used by Simbad. But, since the differences are very small, the transformation is considered verified. The reverse of this transformation can be achieved by taking the inverse of $\boldsymbol{D}_{\mathsf{G}}$ and is not separately verified here.

[1] http://simbad.cds.unistra.fr/simbad/

A.2.4. Arrival galactic frame $\mathcal{G}_a$ - Departure galactic frame $\mathcal{G}_d$

This frame transformation shifts the origin of the $\mathcal{G}_a$-frame to the barycenter of the AC-A/AC-B system to obtain the state in the $\mathcal{G}_d$-frame. The translation is done by addition of the state vector of AC-C, which is calculated from its Kepler elements [34]. To verify that the correct AC-C state vector is added in the translation, the plot in Fig. A.21(a) is used [21]. There, a trajectory is given from the Solar system towards Alpha Centauri. The current positions of the barycenter of AC-A/AC-B and of AC-C are given in the galactic frame originated in the Solar system. The plot in Fig. B21(b) shows that the computed current position of AC-C in the galactic frame is correct. Therefore, it is concluded that the translation from $\mathcal{G}_a$-frame to $\mathcal{G}_d$-frame is verified.

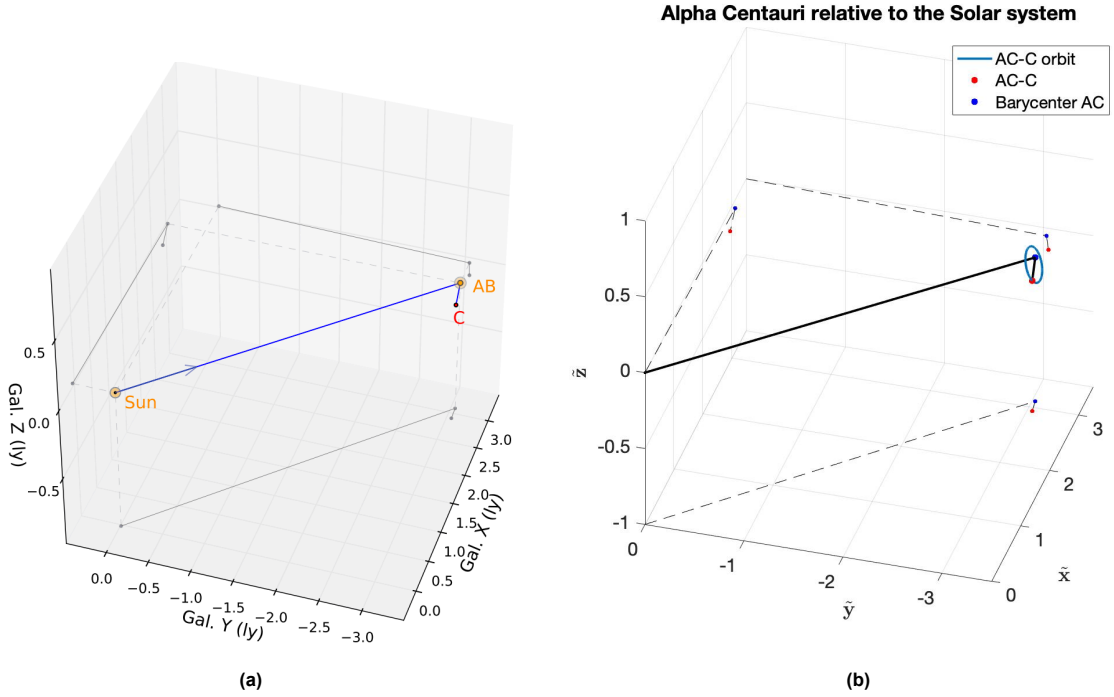

Figure A.21: (a) A photon-sail trajectory from the Solar system toward Alpha Centauri, showing the location of the Sun relative to AC-A/AC-B and AC-C [21]. (b) Plot made to verify the correctness of the shift from AC-C to the barycenter of AC-A/AC-B.

B

Genetic algorithm settings

This Appendix presents the argumentation for the choices in genetic algorithm settings. Properly tuning the settings of the genetic algorithm can help it converge faster, prevent to get trapped in local optima, and, in general, find better solutions.

Three genetic algorithm parameters were chosen to be tuned: the crossover fraction, the population size and the number of generations. The default settings for these parameters are 0.8, 1000 and 40, respectively. To properly tune the settings of the algorithm, different values for each parameter are investigated, while keeping the other two at their default value. The tuning of the parameters was done using the optimization problem described in this research, using the one-sided sail configuration with lightness number $\beta = 1779$. The departure location is the L_2 point (in the AC-A/AC-B system), and the target location is the L_3 point (in the AC-C/Proxima b system). The genetic algorithm is then used to create Pareto fronts that contain the error at linkage between the systems in position, velocity and time, see Figures B.1(a), B.1(b), and B.1(c). The crossover parameter was tested on its default value 0.8, and on one additional value of 0.7. The impact of this variable on the results is the most difficult to predict beforehand. Therefore, tuning of the crossover is done carefully; only one value close to the default (0.7) is tested to see how it impacts the results. It can be seen that a crossover fraction of 0.7 does not necessarily change the resulting Pareto solutions, therefore the crossover setting is kept to its default of 0.8. For the population size, three different values were tested: 500, 1000, and 4000. Figure B.1(b) clearly shows a better convergence towards an optimal solution for the largest population size, and also 1000 performs better than 500. For the number of generations, five different values were tested: 20, 40, 60, 80, and 100. When analysing the plot for the number of generations (Fig. B.1(c)), it is again clear that more generations leads to better results. There can even be seen a difference between generation 80 and 100, where 100 converged slightly more towards the minimal error values. Figure B.1(d) show the convergence of each objective separately over the generations. The blue dots indicate the average score of the entire generation and the red dots mark the best scores for each generation. Especially for the velocity and time errors, it can be seen that the average score is still changing over time, which might indicate that the genetic algorithm has not yet converged towards the optimal solution. To ensure that the genetic algorithm fully converges, the population size is therefore set to 120, so higher than the maximum tested number. Taking into account the number of function evaluations needed, the population size is not set to 4000, although this performed by far the best. Out of computational load considerations, a trade-off was made and the population size was set to 2000. This leads to the final genetic algorithm settings of:

- Crossover: 0.8
- Population size: 2000
- Number of generations: 120

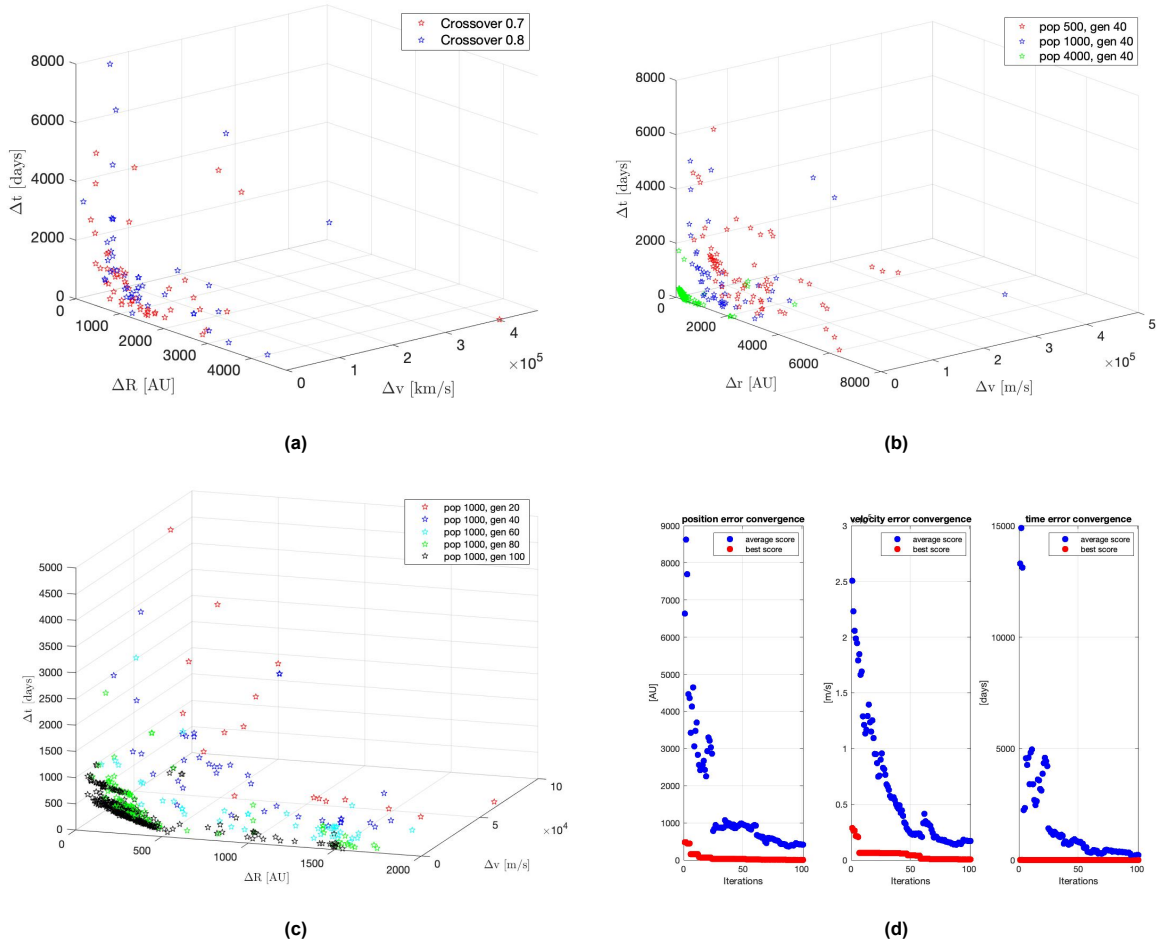

Figure B.1: Pareto front plots made to tune the settings of the genetic algorithm. (a) crossover settings, (b) population size settings, (c) number of generations settings, (d) convergence of each objective over 100 generations (pop 1000, cross 0.8).